National Library of Canada
Bibliothèque nationale du Canada

Canadian Theses Service
Services des thèses canadiennes

Ottawa, Canada
K1A 0N4

CANADIAN THESES
THÈSES CANADIENNES

NOTICE

The quality of this microfiche is heavily dependent upon the quality of the original thesis submitted for microfilming. Every effort has been made to ensure the highest quality of reproduction possible.

If pages are missing, contact the university which granted the degree.

Some pages may have indistinct print especially if the original pages were typed with a poor typewriter ribbon or if the university sent us an inferior photocopy.

Previously copyrighted materials (journal articles, published tests, etc.) are not filmed.

Reproduction in full or in part of this film is governed by the Canadian Copyright Act, R.S.C. 1970, c. C-30.

AVIS

La qualité de cette microfiche dépend grandement de la qualité de la thèse soumise au microfilmage. Nous avons tout fait pour assurer une qualité supérieure de reproduction.

S'il manque des pages, veuillez communiquer avec l'université qui a conféré le grade.

La qualité d'impression de certaines pages peut laisser à désirer, surtout si les pages originales ont été dactylographiées à l'aide d'un ruban usé ou si l'université nous a fait parvenir une photocopie de qualité inférieure.

Les documents qui font déjà l'objet d'un droit d'auteur (articles de revue, examens publiés, etc.) ne sont pas microfilmés.

La reproduction, même partielle, de ce microfilm est soumise à la Loi canadienne sur le droit d'auteur, SRC 1970, c. C-30.

THIS DISSERTATION
HAS BEEN MICROFILMED
EXACTLY AS RECEIVED

LA THÈSE A ÉTÉ
MICROFILMÉE TELLE QUE
NOUS L'AVONS REÇUE

NL-339 (r.86/06)

Canada

THE UNIVERSITY OF ALBERTA

SPIN EXCITATIONS IN s-d SHELL NUCLEI WITH INTERMEDIATE ENERGY PROTONS

by

REYAD ILAYAN TAWFIQ SAWAFTA

A THESIS

SUBMITTED TO THE FACULTY OF GRADUATE STUDIES AND RESEARCH
IN PARTIAL FULFILMENT OF THE REQUIREMENTS FOR THE DEGREE

OF DOCTOR OF PHILOSOPHY

IN

NUCLEAR PHYSICS

DEPARTMENT OF PHYSICS

EDMONTON, ALBERTA

SPRING 1987

Permission has been granted to the National Library of Canada to microfilm this thesis and to lend or sell copies of the film.

The author (copyright owner) has reserved other publication rights, and neither the thesis nor extensive extracts from it may be printed or otherwise reproduced without his/her written permission.

L'autorisation a été accordée à la Bibliothèque nationale du Canada de microfilmer cette thèse et de prêter ou de vendre des exemplaires du film.

L'auteur (titulaire du droit d'auteur) se réserve les autres droits de publication; ni la thèse ni de longs extraits de celle-ci ne doivent être imprimés ou autrement reproduits sans son autorisation écrite.

ISBN 0-315-37668-6

THE UNIVERSITY OF ALBERTA

RELEASE FORM

NAME OF AUTHOR: REYAD ILAYAN TAWFIQ SAWAFTA

TITLE OF THESIS: SPIN EXCITATIONS IN s-d SHELL NUCLEI WITH INTERMEDIATE ENERGY PROTONS

DEGREE: DOCTOR OF PHILOSOPHY

YEAR THIS DEGREE GRANTED: 1987

Permission is hereby granted to THE UNIVERSITY OF ALBERTA LIBRARY to reproduce single copies of this thesis and to lend or sell such copies for private, scholarly or scientific research purposes only.

The author reserves other publication rights, and neither the thesis nor extensive extracts from it may be printed or otherwise reproduced without the author's written permission.

R. Sawafta

Signature

Permenant Adress:
Zahret Nablus Sweets
Al-Hashimi Street
Irbid - Jordan.

Date: March, 10th, 1987.

THE UNIVERSITY OF ALBERTA

FACULTY OF GRADUATE STUDIES AND RESEARCH

The undersigned certify that they have read and recommend to the faculty of Graduate Studies and Research for acceptance a thesis entitled SPIN EXCITATIONS IN s-d SHELL NUCLEI WITH INTERMEDIATE ENERGY PROTONS submitted by REYAD ILAYAN TAWFIQ SAWAFTA in partial fulfilment of the requirements for the degree of DOCTOR OF PHILOSOPHY in NUCLEAR PHYSICS.

.....
Supervisor

.....

.....

.....

.....

Date: 10 March 1987

This work is dedicated to
my
Parents, Brother and Sisters.

ABSTRACT

During the past two years significant improvements have occured at the Medium Resolution Spectrometer (MRS) at TRIUMF, which have made possible many nuclear physics experiments over the full range of TRIUMF energies. With the help of the dispersion matching technique and a front-end wire chamber, nearly background-free (p,p′) spectra with a typical resolution of 150 keV FWHM are observed at forward angles. Spin transfer experiments in (p,p′) have been carried out with the newly installed focal-plane polarimeter which covers a large region of excitation energies (about 45 MeV).

Cross-sections, analyzing powers, and spin-flip probabilities have been measured in the low momentum transfer region in the ^{24}Mg(p,p′)^{24}Mg* reaction at 250 MeV. The spin-flip measurements reveal a large spin-flip probability value (about 0.6) for the M1 region. However, a large spin-flip cross-section distributed uniformally over the energy from 16 to 40 MeV is also observed. The quenching factors for the combined isovector and isoscalar 1^+ states QF(σS_{NN} , 1^+) in the 9-16 MeV region are in good agreement with those for the 10.71 MeV (1^+,T=1) state, (QF=0.7).

Finally, cross-section and analyzing power data have also been obtained for the 11.45 MeV (ΔT=1) and the 9.5 MeV (ΔT=0) M1 transitions in the ^{28}Si(p,p′)^{28}Si* reaction at 200, 250, 290, 360 and 400 MeV. The quenching of the isovector and isoscaler M1 strength is found to be roughly constant as a function of energy relative to theoretical calculations using the density dependent interaction. An average quenching factor of about 0.7 and 0.58 for the strongest 1^+ isovector and isoscalar transitions in the ^{28}Si(p,p′)^{28}Si* reaction, respectively, has been obtained. This work suggests a universal quenching factor for the (p,n), (n,p) and (p,p′) reactions.

ACKNOWLEDGMENTS

I would like to express my gratitude to my supervisor, Dr. Peter Kitching, for his guidance, and support during the course of this work.

I am also deeply indebted to Dr. O. Hausser for suggesting this project and sharing with me his time. I would particularly like to thank Otto for his guidance, understanding, assistance, for being so patient with me during the course of this work and for his financial support for one summer.

Thanks to Dr. R. Abegg, Dr. D. Freckeres, Dr. K. Hicks, Dr. R. Henderson, Dr. D. Hutcheon, Dr. K.P. Jackson, Dr. R. Jeppesen, Dr. C.A. Miller, Dr. M. Vetterli, Dr. S. Yen and all my collaborators at TRIUMF for sharing with me their time and knowledge in Physics and for being always there when I needed them. Special thanks to Dr. R. Abegg for his financial support for the last few months of this work.

I am grateful to Dr. E.D. Cooper and Dr. H. Sherif for their time explaining some of the theoretical aspects of my thesis. Special thanks to Dr. R. Dymarz for providing and helping in some of the theoretical calculations.

To my fellow graduate students, J. Johansson, G. lotz, K. Michaelian and K. Negm, for sharing your knowledege and time with me, I thank you all and wish you luck.

To all the new friends I have made in Canada during the last few years, thank you all for your encouragement, help and the good times we spent together. Special thanks to very special friends O. Othman, M. Othman, H. El-Sharkawi and their families for their continuous encouragement, love and support.

I would like to thank the University of Alberta and the Department of Physics for their continued support in the forms of RA's and TA's during my years as a graduate student.

Last, but by no means least, I would like to thank my family for their love, patience, support, understanding and encouragement.

Table of Contents

Chapter	page
1. Introduction	1
1.1Magnetic Dipole Transitions	1
1.2 Selection Rules	6
1.3 M1 Operator	7
1.4 Why s-d Shell Nuclei	9
1.5 Comparison of Different Probes	10
2. Theory	12
2.1 Scattering Theory	13
2.2 The Density Dependent Hamburg Interaction	20
2.3 Observables	24
3. Experimental Details	26
3.1 The Cycoltron	26
3.2 The Medium Resolution Spectrometer (MRS)	26
3.3 Dispersion Matching	35
3.4 Data Acquisition	38
3.5 Event Trigger and Data Stream	38
3.6 Particle Identification	41
3.7 The Focal Plane Polarimeter (FPP)	41
3.8 Beam Monitors	46
3.9 Experiments 272 and 335	50
4. Data Analysis	53
4.1 The Lisa Data Analysis Program	53
4.2 Coordinate Corrections	53

4.3 Angle Calibration 54
4.4 Normalization 56
4.5 Determination of Overall MRS Efficiency 56
4.6 Calculations of Measured Observables and Uncertainities 59
4.6a Differential Cross Section and Analysing Power 59
4.6b Spin-Flip Probability 61

5. Results and Comparison withTheory 68
5.1 ^{24}Mg(p,p$'$)^{24}Mg* Results 68
5.2 ^{28}Si(p,p$'$)^{28}Si* Results 76
5.3 Spin-Flip Properties 77
5.4 Comparison with Theory 78

6. Conclusion 95

References 97

Appendix 1. Optical Model Potential 102

Appendix 2. Experimental Data for Experiment 272 106

Appendix 3. Experimental data for Experiment 335 114

Appendix 4. Brown and Chung and Wildenthal one body transition densities for 1^+ states in ^{24}Mg and ^{28}Si. 119

List of Tables

Table		Page
3.1	Beam normalization values for TRIUMF beam line 4b in-beam polarimeter	49
5.1	Three-Parameter Fermi density for ^{24}Mg and ^{28}Si.	79
5.2	B(M1) and B(GT) values for the first five (1+,T=1) states in ^{28}Si according to Brown transition densities.	82
5.3	B(M1) and B(GT) values for the (1+,T=1) states in ^{24}Mg according to Brown transition densities.	82
5.4	Quenching of Gamow-Teller and M1 strength in ^{24}Mg.	84
5.5	Quenching factors for the strongest isovecor (1^+,T=1) and isoscalar (1^+,T=0) states in 28Si according to two different calculations, the first is based on Franey and Love interaction and Chung and Wildenthal Transition densities (FL,WC), while the second is based on the Density Dependent Hamburg interaction and Brown and Wildenthal transition densities (DD,BW).	84

List of Figures

Figure	Page
1..1 Levels excited in spin-flip transitions with various probes.	2
1.2a. M1 Strength according to the Independent Particle Model.	5
1.2b. Fragmentation of M1 strength due to configuration mixing.	5
1.2c. M1 strength according to the Independent Particle Model including the Δ state of the nucleon.	5
3.1. General Layout of the TRIUMF facility.	27
3.2. A layout of the Proton Hall showing Beam Line 4B.	28
3.3. A layout of the Medium Resolution Spectrometer (MRS).	29
3.4. Schematic diagram showing the 'X' and 'U' wires in a VDC.	31
3.5. Vector diagram showing the calculation of 'Y' from 'X' and 'U' of the VDCs.	31
3.6. Geometry of the Medium Resolution Spectrometer Focal Plane.	33
3.7. Operation of The Medium Resolution Spectrometer with dispersion Matching.	36
3.8. A layout of the Medium Resolution Spectrometer electronics.	39
3.9. A particle Identification scatter plot (SPID).	42
3.10. A layout of the Focal Plane Polarimeter (FPP).	43
3.11. The Focal Plane Polarimeter Cage assembly.	45
3.12. Arrangement of the In-Beam-Polarimeter scintillator-photomultiplier detector assemly.	48
4.1. Spectrum showing independence of focal plane position on Y_0.	55
4.2. Spectrum showing independence of focal plane position on θ_{pc}.	55
4.3. Energy of outgoing proton after scattering from a polyethelene target (CH_2) at 250 MeV.	57
4.4. Schematic representation of scattering process coordinates.	62
4.5. Schematic representation of cone test.	65
5.1. Momentum spectrum of 250 MeV protons scattered from ^{24}Mg at $\theta_{lab}=2.9°$.	69
5.2. Momentum spectrum of 250 MeV protons inelastically scattered from ^{28}Si at $\theta_{lab}=4°$.	69

5.3. Differential Cross section of 250 MeV protons inelastically scattered from ^{24}Mg at θ_{lab}=2.9° . 71
5.4. Spin-flip cross section $\sigma S_{NN'}$ of 250 MeV protons inelastically scattered from ^{24}Mg at θ_{lab}=2.9° . 71
5.5.Differential Cross section of 250 MeV protons inelastically scattered from ^{24}Mg at θ_{lab}=6.55° . 72
5.6. Spin-flip cross section $\sigma S_{NN'}$ of 250 MeV protons inelastically scattered from ^{24}Mg at θ_{lab}= 6.55°. 72
5.7. Polarization and Analysing Power of 250 MeV protons inelastically scattered from ^{24}Mg at θ_{lab} =2.9°. 73
5.8. Spin-flip probability $S_{NN'}$ of 250 MeV protons inelastically scattered from ^{24}Mg at θ_{lab}=2.9° . 73
5.9. Polarization and Analysing Power of 250 MeV protons inelastically scattered from ^{28}Si at θ_{lab}=6.55°. 74
5.10. Spin-flip probability $S_{NN'}$ of 250 MeV protons inelastically scattered from ^{24}Mg at θ_{lab}=6.55° . 74
5.11. Differential Cross-Section difference between 2.9°and 6.55° for the $^{24}Mg(p,p')^{24}Mg$ reaction. 75
5.12. Spin Flip Cross-Section difference between 2.9° and 6.55° for the $^{24}Mg(p,p')^{24}Mg$ reaction. 75
5.13. Angular distributions for (T=1, 1^+) state at Ex=10.71 MeV in the $^{24}Mg(p,p')^{24}Mg$ reaction at 200 MeV (up) and at 250 MeV (down). The solid curves are the results of the DWBA calculations discussed in the text. 81
5.14. Angular distributions for (T=0, 1^+) state at Ex=9.50 MeV in the $^{28}Si(p,p')^{28}Si$ reaction at 200 MeV (up) and at 250 MeV (down). 86
5.15. Angular distributions for (T=1, 1^+) state at Ex=9.50 MeV in the $^{28}Si(p,p')^{28}Si$ reaction at 200 MeV (up) and at 250 MeV (down). 87
5.16. Angular distributions for (T=0, 1^+) state at Ex=9.50 MeV in the $^{28}Si(p,p')^{28}Si$ reaction at 360 MeV (up) and at 400 MeV (down). 88
5.17. Angular distributions for (T=1, 1^+) state at Ex=11.45 MeV in the $^{28}Si(p,p')^{28}Si$ reaction at 360 MeV (up) and at 400 MeV (down). 89
5.18. Angular distributions for (T=1, 1^+) state at Ex=11.45 MeV in the $^{28}Si(p,p')^{28}Si$ reaction at 290 MeV (up) and for (T=0, 1^+) state at Ex=9.50 MeV at 290 MeV (down). 90

5.19. Quenching factors for the strongest isovector (up) and isoscalar (down) states in ^{28}Si between 200 MeV and 400 MeV using the density dependent interaction and Brown and Wildenthal transition densities. 92

5.20. Quenching factors for the strongest isovector (up) and isoscalar (down) states in ^{28}Si between 200 MeV and 400 MeV using the Franey and Love interaction and Wildenthal and Chung transition densities. 93

5.21. Summary of GT quenching in s-d shell nuclei. 94

1. Introduction

1.1) Magnetic Dipole Transitions (M1)

To each nuclear state corresponds a particular distribution of charges and currents. One can introduce the static multipole moments to describe the interaction of these charges and currents with an external electric or magnetic field. The electric multipole moments are sensitive only to the effective charge distribution in a nucleus, while their magnetic counterparts are sensitive to the effective magnetization within the nucleus. The magnetization density of a nucleus derives from three sources. First, the magnetic moments associated with the spin of the individual nucleons. Second, the orbital motion of the charged particles which includes convection currents in the nucleus. The third source is exchange currents due to the different mesonic degrees of freedom in the nucleus (Yo72). Studies of the magnetic multipole transitions might give the relative importance of these sources.

Consider a target nucleus with neutron and proton numbers denoted by N and Z, respectively. The ground state isospin is given by

$$T_0 = 1/2(N-Z). \qquad 1.1$$

Isospin excitations of this nucleus will have analogues in the adjacent (N+1,Z-1); $T_0=T_0+1$ and (N-1,Z+1); $T_0=T_0-1$ isobars. Schematically represented in figure 1.1 are the possible states that can be excited by a spin-flip isospin-flip transition from the ground state in the target nucleus. The dashed lines in the figure connect the isobaric analogue states and the solid lines denote transitions that can be induced by various hadronic and electromagnetic transitions as indicated by arrows. In the target nucleus (N,Z), spin-flip isospin-flip M1 transitions can be excited by the (p,p´), (e,e´), and (γ,γ´) reactions. The isobaric analogues of the T_0 and T_0+1 states can be excited in the isobar (N-1,Z+1) by (p,n), (^{3}He,t), and (π^+,γ) charge exchange reactions whereas the

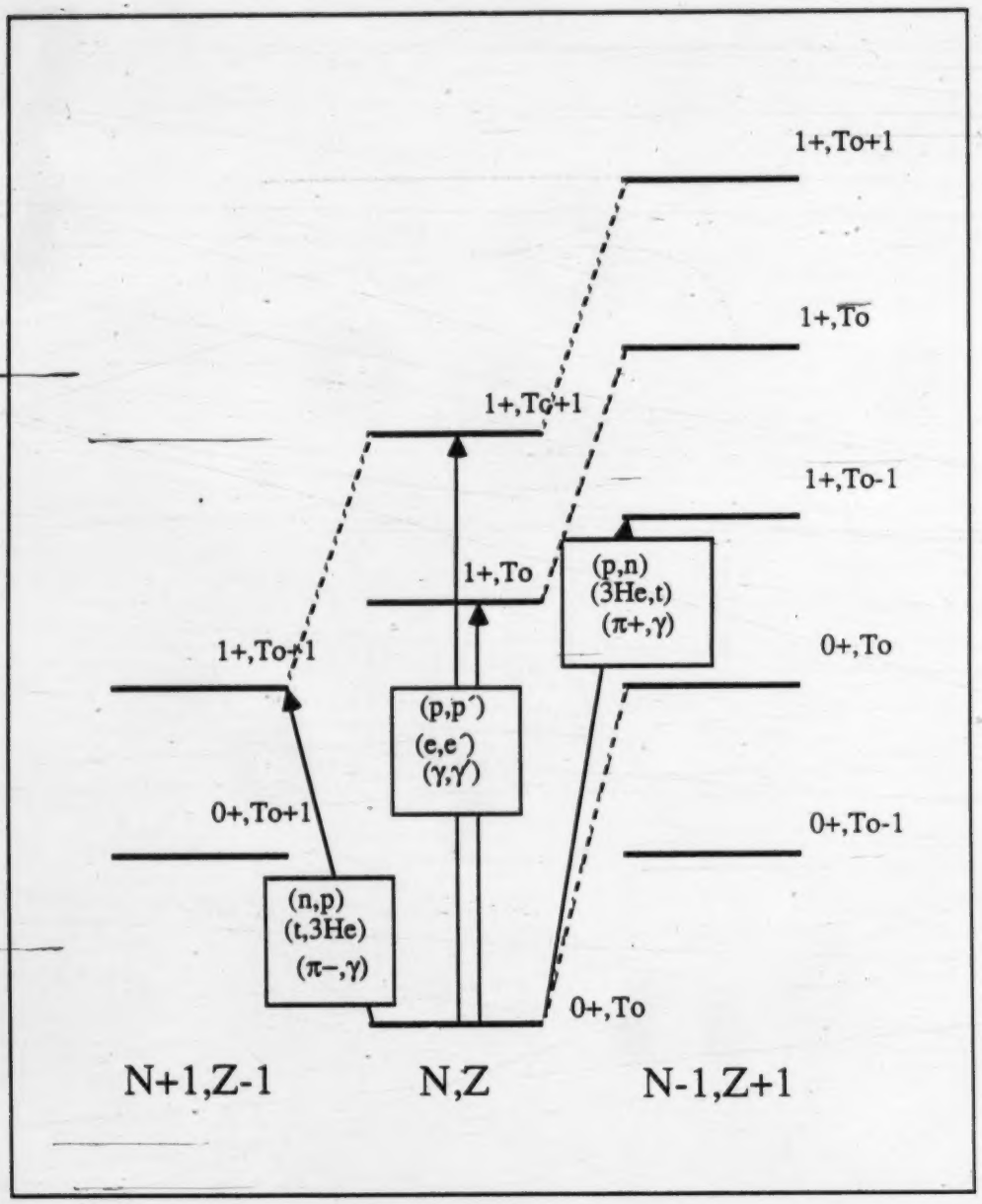

Figure 1.1 Levels excited in spin-flip transitions with various probes.

T_0+1 analogue states may be excited in the (N+1,Z-1) isobar through the (n,p), (t,^{3}He), and (π^-,γ) reactions. In addition, the T_0-1 and T_0+1 analogue states may decay to the ground state of the target nucleus via β^+ and β^- decay, respectively.

The M1 resonance is the isobaric analogue of one of the isospin components of the Gamow-Teller (GT) resonance, and should therefore be seen in the (p,p´) and (e,e´) reactions with a strength comparable to that of the corresponding component of the GT resonance seen in the (p,n) reaction on medium and heavy nuclei. The expected lower limit on the strength of the M1 giant resonance is model-dependent, and the observed strength is an important test of these models. For the GT strength in (p,n) reactions, the operator responsible for the transition is the same as that in the case of β-decay. Hence the β-decay matrix elements can be used in a model independent sum rule for the GT and Fermi strength observed in the (p,n) reaction. The total GT strength for β^- transitions minus that for the β^+ transition is given by the following relation (Ik64)

$$\Sigma B(GT, \beta^-) - \Sigma B(GT, \beta^+) = 3(N-Z),$$

or equivalently

$$\Sigma B(GT,pn) - \Sigma B(GT,np) = 3(N-Z). \qquad 1.2$$

Heavy nuclei have a neutron excess, therefore (n,p) transitions will be Pauli blocked and their total expected B(GT) should be small, so one can write

$$\Sigma B(GT,pn) \approx 3(N-Z). \qquad 1.3$$

Experimentally 60 to 70% of this minimum strength is found in discrete states and the giant Gammow-Teller resonance. No closed form sum rule for the total M1 transition strength in (p,p´) and (e,e´) reactions could be established, but a prediction for the strength dependent only on the nuclear structure form factors for (e,e´) can be made. Sum rules or not, a substantial percentage of the spin transfer strength to 1^+ states in (p,n), (n,p), (p,p´) and (e,e´) reactions has not been identified in the region where the best nuclear structure calculations predict it.

A number of explanations for this "quenching" of the M1 strength has been proposed. The first model suggests that the quenching could be partially explained in terms of mesonic effects (Er73 and Os79). The nuclear configuration space should be

extended to include the excited states of the nucleon, such as the Δ(J=3/2, T=3/2). A spin-flip isospin-flip can couple a nucleon to the Δ, as illustrated schematically by figure (1.2c). The Δ peak is larger because all of the nucleons can participate in the Δ excitation, while the Pauli principle blocks most of them from the particle hole excitation. It might seem that the states are too far away to be significant, but the $V_{\sigma\tau}$ part of the interaction, which is responsible for the Δ-N excitation, is dominated by the one pion exchange term, and the pion couples more strongly to the Δ than to the nucleon. The second model presents a more conventional explanation, which suggest that ordinary nuclear structure effects such as configuration mixing between one-particle-one-hole (1p-1h) and two-particle-two-hole (2p-2h) states (Sh74, Ar79, To79 and Be82), might spread out the M1 strength over a 30-40 MeV wide region of excitation, (fig. 1.2b). The fragmented strength might be too small to be distinguishable from the background at the low energy side, and also too small relative to the strongly excited nuclear continuum in the high energy region; thus implying that it will be very difficult to observe experimentally. This is one of the issues we will attempt to investigate in the spin flip measurement. Typical calculations indicate that 20% of the M1 strength expected from the Independent Particle Model (IPM) disappears, primarily due to the influence of ground state correlations; this still leaves a large gap between theory and experiment.

The Δ has an isospin of 3/2 and that of the nucleon is 1/2, so the sum of the two can never be zero and hence the Δ-N coupling is isovector. This implies that the first model of quenching is blocked from playing a significant role in isoscalar processes. Then, one might conclude that any quenching of isoscalar strength must be taken as a strong indication of the importance of high order configuration mixing, not only in the isoscalar channel, but in the isovector as well. In principle, the dilemma can be solved, if a pure isoscalar transition can be found to test the argument mentioned above, and according to the IPM both ^{12}C and ^{28}Si nuclei have such transitions. This will be discussed in more details later.

Microscopic Random-Phase-Approximation (RPA) calculations (Kl85 and Os85) of the spectrum of ^{90}Zr(p,n) up to 70 MeV of excitation have been performed at 200 MeV. These calculations suggest that the background under the peaks is actually part of the GT strength, and by including it, there is little or no missing strength since they reproduce the measured spectra quite well. This model does not include the (n,p) strength in the sum rule, therefore unless there is a substantial β^+ strength, the Δ-hole admixture is not needed to describe the integrated measured cross section in the (p,n)

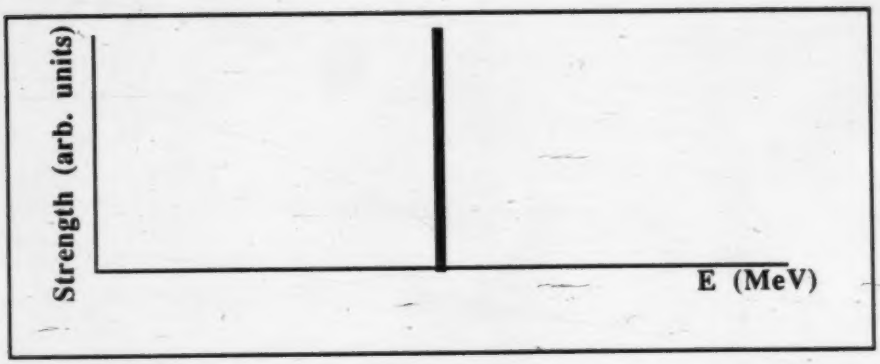

Figure 1.2a M1 strength according to the Independent Particle Model.

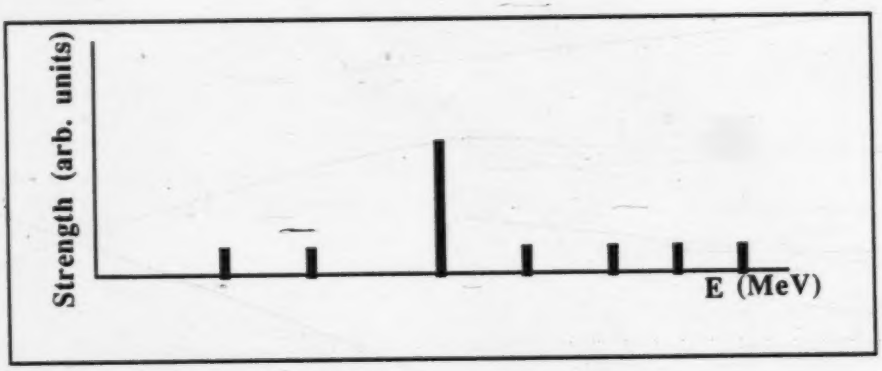

Figure 1.2b Fragmentation of M1 strength due to configuration mixing.

Figure 1.2c M1 strength sccording to the Independent Particle Model including the Δ state of the nucleon.

reactions. Similar calculations (Ya86) have been performed for the forward angle $^{90}Zr(p,p')$ spin-flip spectrum at 319 MeV. It was shown that the whole spectrum up to an excitation energy of Ex=25 MeV can be understood as a superposition of correlated 1p-1h spin-flip ($\Delta S=1$) transitions. The dominant part to the $\Delta S=1$ cross section is contributed by the 2^- states. The conclusion of these calculations is that the Δ isobar quenching mechanism is likely to be small, since the measured cross section is compatible with the transition strength predictions as obtained from the RPA calculations.

The primary focus of this thesis are the properties of spin excitation strength in ^{24}Mg and ^{28}Si as revealed by the inelastic scattering of intermediate energy protons. Interpretation of the data obtained in the present work as well as comparison with available data from various other probes will also be discussed later in chapter 5. In this introduction some of the fundamental aspects of spin excitations and their relevance to nuclear reactions and nuclear structure studies will be discussed.

1.2) Selection Rules

According to the IPM, the M1 strength should be concentrated in a single particle-hole state for a closed shell nucleus. This is represented schematically in figure (1.2a). The M1 transitions are expected to occur between spin-orbit partners in a j-unsaturated shell

$$j = l+1/2 \text{ to } j = l-1/2, \qquad 1.4$$

with $\Delta J = \pm 1$ without any change in parity. This means that one has a spin momentum transfer $\Delta S = 1$, and an orbital angular momentum transfer $\Delta L = 0$ or 2, but $\Delta L = 0$ dominates in the (p,p') reaction at low momentum transfer because of its low multipolarity.

In general, the selection rules for the allowed quantum numbers for M1 transitions are

$$\Delta J = \pm 1,0 \qquad 0 \rightarrow 0 \text{ forbidden}$$

no change in parity , and

$$\Delta T = \pm 1,0 \qquad 1.5$$

1.3) M1 Operator

The magnetic moments of a free proton and a free neutron in nuclear magnetons are

$$\mu_p = 2.79277,$$

and $$\mu_n = -1.91315. \qquad 1.6$$

The magnetic moment operator for a nucleon is

$$\vec{\mu} = g_l \boldsymbol{l} + g_s \mathbf{s} \ , \qquad 1.7$$

where $\boldsymbol{l}$ and s are the orbital angular momentum and the spin, repectively. The values for the spin and orbital g-factors in nuclear magnetons are

$$g_s(p) = +5.59; \qquad g_l(p) = 1;$$

$$g_s(n) = -3.83 ; \qquad g_l(n) = 0. \qquad 1.8$$

It is a good approximation to take for the magnetic moment of a many-nucleonic system the sum of the moments of the individual nucleons

$$\vec{\mu} = \Sigma_i \vec{\mu}_i . \qquad 1.9$$

In spin-isospin notation one can write the M1 operator (Mo58) as follows

$$\vec{\mu} = \mu_0 \Sigma_i^A [\{(g_s^0 - 0.5) \mathbf{s}(i)\} - \{(g_s^1 \mathbf{s}(i) + 0.5 \boldsymbol{l}(i)) \tau_z(i)\}] + \{0.5 \mathbf{J}\}, \qquad 1.10$$

where τ_z and J represent the Pauli matrix for isospin projection and the total angular momentum, respectively. The first and third terms of equation (1.10) consitute the isoscalar ($\Delta T = 0$) part of the transition, while the second term is the isovector ($\Delta T = 1$) part. Both the initial and final states are eigenstates of J, and so the operator J cannot cause transitions between states of different J, so only the first term gives the strength of the isoscalar transition. The values of the scalar and vector g-factors with their values in nuclear magnetons are

$$g_s^0 = 0.5\,[\,g_s(p) + g_s(n)\,] = 0.88$$

$$g_s^1 = 0.5\,[\,g_s(p) - g_s(n)\,] = 4.71. \qquad 1.11$$

Because g_s^1 is much larger than the other g-factors, the magnetic moment operator is mostly isovector and is mostly a spin operator. The relative strength of the isoscalar and isovector parts of the M1 operator is determined by the ratio

$$|\,(g_s^0 - 0.5) / g_s^1\,|^2 \sim 10^{-2}, \qquad 1.12$$

and this implies that $\Delta T = 0$, M1 transtions in self conjugate (N=Z) nuclei are strongly inhibited compared to their isovector counterparts. This dominance of the isovector character of the M1 operator is known as Morpurgo's selection rule (Mo58).

The reduced transition probability B(M1↑) for an M1 transition from J_i to J_f is proportional to the square of the reduced matrix element of the operator μ between the two states. It is given by

$$B(M1\uparrow) = (2J_i+1)^{-1}\,|\,<J_f T_f \|\,\vec{\mu}\,\| J_i T_i>\,|^2 . \qquad 1.13$$

This quantity is proportional to the reaction strength for electromagnetic interactions such as (e,e') and (γ,γ').

So M1 transitions enjoy a relatively unique position in the study of nuclear structure properties. Since the M1 operator is mostly an isovector and mostly a spin operator, M1 transitions are especially suited for probing the spin and isospin characteristics of the nucleus. This ability is very clear in the many especially strong spin-flip transitions throughout the nuclides and in the spin- and isospin-flip transitions in the self conjugate nuclei. Thus M1 transitions can test basic selection

rules, help determine the role of the spin-flip mechanism in transitions, and can give information on the spin-dependence of the nuclear force (Be81).

1.4) Why s-d Shell Nuclei ?

In this section we will discuss some of the reasons which led us to suggest ^{24}Mg and ^{28}Si as the desired targets to be used in this work. Our reasoning is based partially on a paper by Brown and Wildenthal (Br83). They suggested the use of s-d shell nuclei for the study of spin excitations and especially M1 transitions, because such processes are dominated in this region by spin-isospin-flip only. Some of the reasons are listed below

1) Shell model wave functions for these nuclei have been checked to confirm that they reproduce the complete range of spectroscopic features with good accuracy.

2) The selection rules for M1 excitation confine the transition amplitudes to lie within the s-d shell space. The full $0d_{5/2}$- $1s_{1/2}$- $0d_{3/2}$ configuration space wave functions can encompass the complete giant resonance strength.

3) The density of the states is low enough that most of the strength is concentrated in the lowest few M1 levels.

4) From an experimental point of view, there are measurements of gamma and beta decay strengths involving these states and their excitation probabilities via the (e,e´) and (p,n) reactions. Correlation between these data make possible a detailed analysis of the structure of the transitions and of the validity of shell-model wave functions.

5) The s-d shell system might serve as a paradigm for heavier systems like the f-p shell as an example; so the conclusions may have some implications for the general case of M1 excitations.

The ^{28}Si target was chosen because according to the IPM, it is the heaviest T=0 nucleus that can provide a single T=0, 1^+ state, which is strongly excited in the (p,p´) reaction and appears to be as free from mixing with T=1 state as any likely to be found. It is predicted to be at an excitation energy of 9.5 MeV and hence separated by more than one MeV from the lowest predicted T=1 state at 10.59 MeV. Then, a pure isoscalar transition (ΔT=0) can be measured, and one might be able to distinguish between the suggested sources of quenching. As was mentioned before in this chapter the Δ-isobar admixture is isovector by nature and cannot contribute to isoscalar

processes, any source of quenching for such processes as well as for the isovector ones could be related to higher order configuration mixing (An84). The ^{24}Mg target is also special, because of the different charecteristics of its 1^+ states. The 1^+ state at 9.97 MeV is dominated by orbital contributions, while that at 10.71 MeV is dominated by spin contributions. Also the known B(M1) values are well explained by the shell model calculations. In general one hopes to study the reaction mechanism if the nuclear structure uncertainities are minimized, which is the case for the s-d shell nuclei.

1.5) Comparison of Different Probes

Because of the spin and isospin structure of the nucleon, it is a rich probe for nuclear structure. The reaction mechanism for nucleon-nucleus reactions such as (p,p'), (p,n) and (n,p) scattering is not, however, as well understood as that for electron scattering and this clearly limits the quantative reliability of nucleon-nucleus scattering for extracting dynamical structure information. One of the most significant uncertainities in the reaction mechanism for nucleon scattering is an incomplete knowledge of the underlying nucleon-nucleon coupling itself. Studying the nucleus with different probes gives usually different and complementary information about nuclear structure and reaction mechanisms. Electrons interact with the nucleus via the electromagnetic interaction, which is very well known. Because the electromagnetic interaction is relatively weak, the distortions of the incoming and outgoing electron waves are small and can be computed if necessary. In back angle electron scattering one excites primarily spin excitations of the target nucleus with a great enhancement of $\Delta T=1$ transitions over $\Delta T=0$ transitions.

Nucleon scattering is a more complex and yet a richer process than electron scattering. The nucleon-nucleon interaction is usually parameterized to fit free N-N scattering data, which is usually extended to describe nucleon-nucleus scattering. In the (p,p') reaction both $\Delta T=0$ and $\Delta T=1$ spin excitations can occur, which makes it more complex than electron scattering. Distortion effects are large because the interaction is strong. These effects are usually calculated from an optical potential fitted to elastic proton scattering, with associated uncertainties.

Proton and electron scattering generally agree on the identification of the M1

states, but there are disagreements, particularly when the strength is broadly distributed. The most notorious example is ^{51}V where a peak near 10 MeV has been identified as the M1 giant resonance using (p,p') (Na85), while no peak at all is observed in this region in low energy electron scattering. There are possible explanations for discrepancies between (p,p') and (e,e') in terms of orbital contributions. Orbital currents contribute to electron scattering, while nucleon scattering sees essentially only the spin term in the magnetic operator. Another possible explanation for discrepancies between the two probes could be the fact that (e,e') experiments must be done near 180° where the momentum transfer is large and because any (e,e') excitations are observed on a large background from the radiative tail of the elastic scattering. This would result in some difficulties distinguishing the actual M1 strength from the background.

As discussed before in this chapter, the M1 operator is an isovector operator for the (p,n) reaction and the (e,e') reaction at backward angles. Also, it was mentioned that the isoscalar interaction in the (p,p') reaction is very small compared to its isovector counterpart at intermediate energies. This implies that (e,e'), (p,p') and (p,n) reactions should yield directly comparable strengths.

2. Theory

The nucleon is the most easily accessible and at the same time one of the most powerful probes for the study of nuclear structure; especially at intermediate energies. In the energy range of 100-400 MeV, the NN reaction cross section has a wide minimum and therefore nuclear transparency is at a maximum. Approaches based on multiple scattering theory use the free NN scattering amplitude as a driving operator on the elementary NN level. For the nucleon-nucleus interaction, the scattering mechanism is based on the elementary NN interaction in which the rest of the target nucleons play the role of spectators preserving the centre of mass motion. The validity of this idea has been verified for energies above 500 MeV. Below this energy the scattering process between the incoming projectile and the medium is influenced more and more by the phase space limitations imposed by the surrounding fermion medium leading to Pauli blocking, off-shell effects in the NN scattering and higher-order effects including excitation of intermediate states in the target system. Most of these effects become increasingly important with decreasing energy (Ri84).

The perturbing interaction which gives rise to inelastic scattering is the effective interaction between the incoming projectile (p) and each nucleon (i) of the target nucleus. Regardless of origin or method of derivation, the effective interaction is usually constructed to be of the following (or an equivalent) form

$$\begin{aligned} V(r_i,r_p) = {} & V_0(r)+V_\sigma(r)\ (\sigma_i\cdot\sigma_p) + V_\tau(r)\ (\tau_i\cdot\tau_p) \\ & + V_{\sigma\tau}(r)\ (\sigma_i\cdot\sigma_p)\ (\tau_i\cdot\tau_p) \\ & +[V_{LS}(r)+V_{LS\tau}(r)\ (\tau_i\cdot\tau_p)\ ]\ L\cdot S \\ & +[V_T(r)+V_{T\tau}(r)\ (\tau_i\cdot\tau_p)\ ]S_{12} \quad , \end{aligned} \qquad 2.1$$

where σ and τ denote the spin and isospin respectively, $L\cdot S$ and S_{12} are the usual spin-orbit and tensor operators, with

$$S = (1/2)\,(\sigma_i + \sigma_p),$$

and $$S_{12} = 3\,(\sigma_1 \cdot r)(\sigma_2 \cdot r) - \sigma_1 \cdot \sigma_2 \qquad 2.2$$

The central spin-dependent (V_σ,$V_{\sigma\tau}$) and tensor forces (V_T,$V_{T\tau}$) which are able to induce spin transfer are of primary interest here.

Inelastic scattering studies may be considered as a test of the effective interaction putting different weights on the individual components as compared to the elastic channel. The M1 transitions are of special interest, because they can provide such tests. They could be classified in two different classes, the first class is the isoscalar transition $\Delta T=0$ which is primarily sensitive to the V_σ component. The second class is the isovector transition $\Delta T=1$ which requires in addition to a spin-flip an isospin-flip and therefore selects out $V_{\sigma\tau}$. In the following section, a brief introduction to scattering theory will be given then a short description of the Hamburg density dependent interaction will follow.

2.1) Scattering Theory

Consider the total Hamiltonian for a nucleon interacting with a target

$$H = H_0 + V(r,\xi) \ , \qquad 2.3$$

where H_0 is the kinetic energy of relative motion, $\xi = r_1, \ldots r_A$ denotes all nuclear coordinates, and $V(r,\xi)$ is the interaction potential of the incident projectile (p) with the target which can be written in the following fashion

$$V = V(r,\xi) = \Sigma_i v_{ip} \ , \qquad 2.4$$

where v_{ip} is the interaction of the projectile and the i^{th} nucleon in the target nucleus. Denote Ψ as the total wavefunction of the target-projectile system such that

$$(E-H)\,|\Psi> = 0. \qquad 2.5$$

In the absence of a potential, we replace the total wave function Ψ by a plane wave ϕ and the problem becomes

$$(E-H_0)\,|\,\phi\,\rangle = 0. \qquad 2.6$$

The Green's functions related to equations (2.5) and (2.6) are

$$G_0^{\pm} = [\,E- H_0 \pm i\varepsilon\,]^{-1}$$

and

$$G^{\pm} = [\,E- H \pm i\varepsilon\,]^{-1} \quad , \qquad 2.7$$

where (+) and (-) refer to outgoing and incoming boundary conditions, respectively. Using the following identity

$$(1/A) - (1/B) = (1/B)\,(B-A)\,(1/A) \quad , \qquad 2.8$$

one can find integral equations relating G_0 and G. Assuming

$$A = E- H_0$$

and

$$B = E-H = E- H_0-V \quad , \qquad 2.9$$

gives

$$G^{(\pm)} = G_0^{(\pm)} + G_0^{(\pm)}\, V\, G^{(\pm)}. \qquad 2.10$$

The Lipmann-Schwinger equation for the total wave function is

$$|\,\Psi^{(\pm)}\rangle = |\,\phi\,\rangle + G_0^{(\pm)}\ V\,|\Psi^{(\pm)}\rangle, \qquad 2.11$$

or equivalently

$$|\,\Psi^{(\pm)}\rangle = |\,\phi\,\rangle + G^{(\pm)}\ V\ |\,\phi\,\rangle. \qquad 2.12$$

One can define a transition operator T

$$T^{(\pm)} = V + G^{(\pm)} V \ , \qquad 2.13$$

which may be rewritten alternately as

$$T^{(\pm)} = V + V G_0^{(\pm)} T^{(\pm)} . \qquad 2.14$$

The transition matrix for a scattering process from an initial state |i> to a final state |f> is given by

$$T_{fi} = < \phi_f \mid T^{(+)} \mid \phi_i^{(+)} >$$

or $$T_{fi} = < \phi_f \mid V \mid \Psi_i^{(+)} > . \qquad 2.15$$

Let us now consider a special case, namely the scattering from two potentials

$$V = U + W \ , \qquad 2.16$$

and the T-matrix is given by

$$T_{fi} = < \phi_f \mid U+W \mid \Psi_i^{(+)} > . \qquad 2.17$$

Suppose that we can find a solution for the Hamiltonian involving U only

$$H_1 = H_0 + U \ , \qquad 2.18$$

so $$H_1 \mid \chi^{(+)} > = E \mid \chi^{(+)} > . \qquad 2.19$$

The Green's functions for this problem are

$$G_0^{(\pm)} = [\, E - H_0 \pm i\varepsilon \,]^{-1}$$

$$G_1^{(\pm)} = [\, E - H_0 - U \pm i\varepsilon \,]^{-1}$$

$$G^{(\pm)} = [\, E - H_0 - U - W \pm i\varepsilon \,]^{-1} . \qquad 2.20$$

Using the identity (2.8), one can find integral equations relating $G_0^{(\pm)}$ and $G^{(\pm)}$, assuming

$$A = E - H_0 - U$$

and $$B = E - H_0 - U - W, \qquad 2.21$$

then leads to

$$G^{(\pm)} = G_1^{(\pm)} + G_1^{(\pm)} W G^{(\pm)}. \qquad 2.22$$

The Lippmann-Schwinger equations for the wave functions are

$$\chi^{(\pm)} = \phi + G_1^{(\pm)} U \phi$$

$$= \phi + G_0^{(\pm)} U \chi^{(\pm)}$$

and $$\Psi^{(\pm)} = \phi + G^{(\pm)} (U+W) \phi. \qquad 2.23$$

and substitution of $G^{(+)}$ in the last equation gives

$$\Psi^{(+)} = \phi + (G_1^{(+)} + G_1^{(+)} W G^{(+)}) (U+W) \phi \ , \qquad 2.24$$

which could be rewritten as

$$\Psi^{(+)} = \chi^{(+)} + G_1^{(+)} W \Psi^{(+)}. \qquad 2.25$$

Now consider the scattering amplitude

$$T_{fi} = \langle \phi_f \mid U+W \mid \Psi_i^{(+)} \rangle \ , \qquad 2.26$$

using equation (2.25) the matrix element can be written as

$$T_{fi} = \langle \phi_f \mid U \mid \chi_i^{(+)} \rangle + \langle \phi_f \mid W+UG_1^{(+)} W + G_1^{(+)} W G^{(+)} \mid \phi \rangle. \qquad 2.27$$

After some iteration, and by using equation (2.24), one can write

$$T_{fi} = \langle \phi_f \mid U \mid \chi_i^{(+)} \rangle + \langle \chi_f^{(-)} \mid W \mid \Psi_i^{(+)} \rangle . \qquad 2.28$$

The presence of the total wavefunction $\Psi_i^{(+)}$ in the second term generally precludes solving the problem exactly but there are various ways to approximate the solution. Let us recall the matrix element

$$T_{fi} = \langle \phi_f \mid V \mid \Psi_i^{(+)} \rangle , \qquad 2.29$$

and introduce a spherical optical potential in an artificial way

$$T_{fi} = \langle \phi_f \mid (V-U)+U \mid \Psi_i^{(+)} \rangle$$

$$= \langle \phi_f \mid \omega + U \mid \Psi_i^{(+)} \rangle . \qquad 2.30$$

If we take the potential U to be the optical potential for the problem, then the distorted waves are solution of

$$(E-H_0-U) \mid \chi \rangle = 0. \qquad 2.31$$

Using the same procedures discussed above for the two potential case, then one can write the T-matrix as follows

$$T_{fi} = \langle \phi_f \mid U \mid \chi_i^{(+)} \rangle + \langle \chi_f^{(-)} \mid \omega \mid \Psi_i^{(+)} \rangle . \qquad 2.32$$

Because U is spherical the first term in the previous equation does not contribute for an inelastic transition where $i \neq f$, while the second term does. Then the matrix element can be written as

$$T_{fi} = \langle \chi_f^{(-)} \mid \omega \mid \Psi_i^{(+)} \rangle . \qquad 2.33$$

The simplest possible approximation is to replace $\chi_f^{(-)}$ and $\Psi_i^{(+)}$ by plane waves, then the T-matrix can be written as

$$T_{fi} = \langle \phi_f \mid \omega \mid \phi_i \rangle . \qquad 2.34$$

This is the T-matrix in the Plane Wave Born Approximation (PWBA). A much better approximation is achieved if we expand the total wave function $\Psi_i^{(+)}$ using equation (2.25) and keep only the first term in the expansion to obtain

$$T_{fi} = \langle \chi_f^{(-)} \mid \omega \mid \chi_i^{(+)} \rangle + \langle \chi_f^{(-)} \mid \omega\, G_1^{(+)}\, \omega \mid \chi_i^{(+)} \rangle + \ldots$$

$$\approx \langle \chi_f^{(-)} \mid T \mid \omega \mid \chi_i^{(+)} \rangle . \qquad 2.35$$

This is the T-matrix for inelastic scattering in the Distorted Wave Born Approximation (DWBA).

Another commonly used distorted wave approximation is the Distorted Wave Impulse Approximation (DWIA). To derive the DWIA matrix element we start with the inelastic part of equation

$$T_{fi} = \langle \chi_f^{(-)} \mid \omega \mid \Psi_i^{(+)} \rangle . \qquad 2.36$$

In the Impulse approximation, one assumes that the total residual interaction is the sum of the two body residual interactions

$$\omega = \Sigma_i \omega_i = \Sigma_i (v_{ip} - U/A) , \qquad 2.37$$

where U is the average potential. Expanding the total wave function as in (2.25) we can write the T-matrix element as

$$T_{fi} = \langle \chi_f^{(-)} \mid \omega \mid \chi_i^{(+)} + G_1^{(+)}\, \omega\, \Psi_i^{(+)} \rangle$$

$$= \langle \chi_f^{(-)} \mid \omega + \omega\, G_1^{(+)}\, \omega + \ldots \mid \chi_i^{(+)} \rangle$$

$$= \langle \chi_f^{(-)} \mid t \mid \chi_i^{(+)} \rangle , \qquad 2.38$$

where we have defined the t-matrix by

$$t = \omega + \omega G_1^{(+)} t \ ,$$

or

$$t = \Sigma_i \omega_i + \Sigma_i \omega_i G_1^{(+)} t_i \ . \qquad 2.39$$

By introducing an effective two body t-matrix as

$$t_i = \omega_i + \omega_i G_1^{(+)} t_i \qquad 2.40$$

and with some algebric manipulation, one obtains

$$t = \Sigma_i t_i + \Sigma_i t_i G_1^{(+)} \Sigma_{k \neq i} t_k + \ldots \ . \qquad 2.41$$

The free two body t-matrix obeys the relation

$$t_i^{(0)} = v_{ip} + v_{ip} G_0 t_i^{(0)} \ . \qquad 2.42$$

The final form of the t-matrix in DWIA is given by

$$T_{fi} = < \chi_f^{(-)} | \Sigma_i t_i^{(0)} | \chi_i^{(+)} > , \qquad 2.43$$

and if we set U=0, the distorted waves will be replaced by plane waves and thus yielding the Plane Wave Impulse Approximation (PWIA), and the T-matrix is given by

$$T_{fi} = < \phi_f | \Sigma_i t_i^{(0)} | \phi_i > . \qquad 2.44$$

Most of the microscopic approaches to the nucleon-nucleus interaction are based on the impulse approximation formalism where the NN interaction is used as an input. Because the interaction between an incident nucleon and that of the nucleus is not exactly the same as the free NN interaction, certain modifications have to be applied to the T-matrix to take this into account. The most direct alternative is to use the effective NN interaction, where the T-matrix is modified to include Pauli blocking, exchange and medium effects . This will be discussed in more details in the next section, where we take the Density Dependent Hamburg Interaction as an example.

2.2) The Density Dependent Hamburg Interaction (DD)

The introduction of complex energy-dependent and density-dependent interactions with all the complications of spin-isospin dependence is essential to describe the experimental data. The Hamburg density dependent interaction (DD) describes nuclear matter in terms of a Fermi gas in its ground state, thus any given point in the nucleus is characterized by a local Fermi momentum. The semi-phenomenological momentum-dependent Paris potential is used as input for the reaction matrix. This potential describes the long and medium range of the NN interaction in terms the exchange of one pion, two pions, and the ω-meson between the interacting nucleons. The short range part of the interaction; where the internucleon distance is less than 0.8 fermis, is represented by a phenomenological soft core repulsive interaction. A full description of the DD interaction is given in detail in reference (Ri84) but for the sake of completeness a brief description will be given.

The microscopic optical potential follows the infinite nuclear matter approach (Hu72 and Je76), which identifies the single particle mass operator with the optical model in infinite nuclear matter in the lowest order of the hole-line expansion

$$U_{opt}(a) = \sum_{|m|< K_f} < \phi_{am} \mid t(w) \mid \phi_{am} >_A \quad , \qquad 2.45$$

where t(w) is the antisymmetrized plane wave matrix element satisfying the Bethe-Goldstone (BG) equation

$$t(w) = V + V\, G_Q^{(+)}(w)\, t(w), \qquad 2.46$$

and V is the free NN Paris potential (La80). The Green's function $G_Q^{(+)}(w)$ which is given by

$$G_Q^{(+)}(w) = Q(K,q,K_f)\, [\omega - e(b) - e(c) + i\,\omega]^{-1}, \qquad 2.47$$

contains outgoing wave boundary conditions, and medium effects which is ensured by the Pauli projection operator

$$Q(K,q,K_f) = \sum_{|b|,|c|>K_f} | \phi_{bc} > < \phi_{bc} | , \qquad 2.48$$

where $|b|,|c| > K_f$ ensures that the two particles in the intermediate states propagate only in unoccupied momentum states above the Fermi momentum K_f, and e(k) represent the single particle energies. The starting energy is identified as the sum of the projectile energy e(a) and the energy of the struck single particle in the medium

$$\omega = e(a) + e(m). \qquad 2.49$$

Using equation (2.15), one can introduce the following identity

$$< \phi_{am}| \, t(w) \, | \phi_{am} > = \, < \phi_{am}| \, V \, | \psi_{am} >. \qquad 2.50$$

The correlated wave function ψ_{am} satisfies a related Bethe-Goldstone equation

$$\psi_{am} = \phi_{am} + G_Q^{(+)}(w) \, V \, \psi_{am}. \qquad 2.51$$

The single particle energies e(k) in equations (2.47) and (2.49), contain the kinetic energy and a self-consistent energy-dependent potential energy

$$e(k) = (\hbar^2 k^2/2m) + u(k) \quad . \qquad 2.52$$

The choice for u(k) was taken to be the real part of the lowest order nuclear mass operator defined by equation (2.46). For $K_f = 0$, u(k) = 0, the Pauli projection operator goes over to one and the resulting matrix elements are those of the free t-matrix which can be directly compared to NN data. By replacing the integral by a trapezoidel rule integration, equation (2.47) is transformed into a system of linear equations. The correlated wave functions which are the solutions of equation (2.51) then enable us to generate a complex energy and density dependent effective interaction in the form of a two nucleon potential

$$t(r) = \Sigma_{ST} \, t_0^{ST}(r) \, P^S P^T + \Sigma_T \, t_1^T(r) \, (\mathbf{L}.\mathbf{S}) \, .P^T + \Sigma_T \, t_2^T(r) \, S_{12} \, P^T$$

$$= \Sigma_K \, (\, \mathbf{R}_K \, . \mathbf{S}_K \,). \qquad 2.53$$

With the scalar product, one distinguishes tensor operators $\mathbf{R}_K$ of rank K, acting on coordinate space elements, and $\mathbf{S}_K$ acting in spin / isospin space, respectively. The r-space representation of the effective interaction is given in terms of Yukawa form factors, and they are of the following forms

Central:

$$t_0^{ST}(r) = \Sigma_i t_i^{ST}(r)\,(r)^{-1} \exp(-\mu_i r)$$

Spin-Orbit:

$$t_1^{ST}(r) = \Sigma_i t_i^{T}(r)\,(r)^{-1} \exp(-\mu_i r) + \Sigma_T\, t_1^{T}(r)\,[\mathbf{L}.(\sigma_1+\sigma_2)/2)]$$

Tensor:

$$t_2^{T}(r)\, S_{12} = \Sigma_i t_i^{T}(r)\,(r^2)\,(r)^{-1} \exp(-\mu_i r)\,[(3/r^2)\,(\sigma_1.\hat{r})\,(\sigma_2.\hat{r}) - (\sigma_1.\sigma_2). \quad 2.54$$

The local non-relativistic form of the optical potential is obtained by folding the single particle density of a target ground state with the complex effective interaction including both the direct and exchange terms

$$U(r,E) = \int d^3s\, \rho(|r+s|)\,\{ Z\, t_p^{D}(s,\hat{k},E) + N\, t_n^{D}(s,\hat{k},E)\}$$

$$+ \int d^3s\, \rho(|r+(1/2)s|)\, 3\, \{j_1(\hat{k}s)/\hat{k}s\}\, j_0(k_f(r)s)$$

$$\cdot\{ Z\, t_p^{Ex}(s,\hat{k},E) + N\, t_n^{Ex}(s,\hat{k},E)\}, \quad 2.55$$

wherein

$$\hat{k} = k_f(|r+(1/2)s|)$$

$$k_f = \{(3/2)\,\pi^2 \rho(r)\}^{1/3} \quad , \quad 2.56$$

and the complex local momentum is given self-consistently by

$$\hbar k(r) = [2m\{e-u(r)-V_{coul}(r)\}]^{1/2}. \quad 2.57$$

At intermediate energies, the real part of the central potential resembles a bottle-bottom shape; which is a result of direct and exchange interference effects together with density dependence in the interaction. The inelastic transitions are analysed using the fully antisymmetrized DWTA where the exchange amplitudes are treated exactly with the t-matrix as driving transition operator. The DWTA and the DWIA are distinguished by the use of the density-dependent t-matrix in the former whilst the latter is based on the free t-matrix. The density-dependent distorted wave T-matrix

$$T_{DWTA} = \Sigma_{j1,j2} S_{j1j2}^{LT} \langle \chi_f^-(r_0)\, \phi_{j2}(r_1) \mid t(|r_0 - r_1|; LDA) \mid \{ \chi_i^+(r_0)\, \phi_{j1}(r_1) - \chi_i^+(r_1)\, \phi_{j1}(r_0) \} \rangle , \qquad 2.58$$

wherein S_{j1j2}^{LT} is the spectroscopic factor, and the distorted waves $\chi^{\pm}$ could be computed either with phenomenological or microscopic optical potentials. The notation for the transition operator emphasizes the density dependence and the use of the local density approximation (LDA). The term $t(|\mathbf{r}_0 - \mathbf{r}_1|; LDA)$ in equation (2.58), requires a recipe for handling the dependence of the two coordinates $\mathbf{r}_0$ and $\mathbf{r}_1$ which point into different density regions. This recipe could be achieved by using either the geometric mean

$$t(|\mathbf{r}_0 - \mathbf{r}_1|; LDA) = [\{t(|\mathbf{r}_0 - \mathbf{r}_1|; k_f(r_0)\} \cdot \{t(|\mathbf{r}_0 - \mathbf{r}_1|; k_f(r_1)\}]^{1/2} , \qquad 2.59$$

or alternatively the arithmetic mean

$$t(|\mathbf{r}_0 - \mathbf{r}_1|; LDA) = (1/2)[\{t(|\mathbf{r}_0 - \mathbf{r}_1|; k_f(r_0)\} + \{t(|\mathbf{r}_0 - \mathbf{r}_1|; k_f(r_1)\}]. \qquad 2.60$$

In practice these two prescriptions are not distinguishable.

An alternative approach used to obtain an effective interaction has been pursued by Love and Franey (Lo81, Lo83 and Fr85). They start from the general invariant structure of the free NN scattering amplitude

$$M(E_{c.m.}, \theta) = A + B\,(\sigma_1.\hat{n})\,(\sigma_2.\hat{n}) + C\,(\sigma_1 + \sigma_2).\hat{n} + D\,(\sigma_1.\hat{q})\,(\sigma_2.\hat{q}) + E\,(\sigma_1.p)\,(\sigma_2.p) . \qquad 2.61$$

where

$$\mathbf{n} = (\mathbf{k}\times\mathbf{k}') / |\mathbf{k}\times\mathbf{k}'|$$

$$\mathbf{q} = (\mathbf{k}'-\mathbf{k}) / |\mathbf{k}'-\mathbf{k}|$$

$$\mathbf{p} = (\mathbf{k}'+\mathbf{k}) / |\mathbf{k}'+\mathbf{k}|, \qquad 2.62$$

k (k´) is the projectile (ejectile) momentum, and the (A, B, C, D and E) amplitudes are constructed from phase shift analysis, (Ar84), extracted from experimental NN data. An equivalent ansatz to equation (2.58) is then used together with a criterion to reproduce these amplitudes. This approach is very appealing as it makes direct use of NN informations, but medium corrections of any sort are not included, a feature which is important especially at low and intermediate energies.

2.3) Observables

The measured observables for nucleon-nucleus inelastic scattering are related to the T-matrix as follows

$$d\sigma/d\Omega = 1/2\ (k_f/k_i)\ (m/2\pi)^2\ \mathrm{Tr}\ (TT^\dagger)$$

$$A = \mathrm{Tr}\ (T\sigma T^\dagger) / \mathrm{Tr}\ (TT^\dagger)$$

$$P = \mathrm{Tr}\ (TT^\dagger\sigma) / \mathrm{Tr}\ (TT^\dagger)$$

$$D_{ij'} = \mathrm{Tr}\ (T\sigma_i T^\dagger \sigma_{j'}) / \mathrm{Tr}\ (TT^\dagger) \qquad 2.63$$

where $d\sigma/d\Omega$, A, P, and $D_{ij'}$ refer to the differential cross section, analyzing power, polarization, and polarization transfer coeffecients, respectively, while i refers to the incident projectile frame and j´ refers to the ejectile frame. The polarization transfer coeffecients are identical to the "Wolfenstein" parameters (Wo54)

$$D_{SS'} = R$$

$$D_{LS'} = A$$

$$D_{SL'} = R'$$

$$D_{LL'} = A'$$

$$D_{NN'} = D. \qquad 2.64$$

The spin flip probability $S_{NN'}$ is related to the $D_{NN'}$ as follows

$$S_{NN'} = (1/2)\,(1 - D_{NN'}). \qquad 2.65$$

For nucleon-nucleus elastic scattering from a spin zero target, there are only three independent observables that can be measured, namely the cross section, analyzing power and the spin rotation parameter Q which is defined as (Sh85)

$$Q = Tr\,(T\sigma_z T^{\dagger}\sigma_x) / Tr(TT^{\dagger}). \qquad 2.66$$

Q is related to the polarization transfer coeffecients as follows

$$Q = D_{LS'}\cos\theta_{Lab} + D_{LL'}\sin\theta_{Lab}$$

$$= -D_{SL'}\cos\theta_{Lab} + D_{SS'}\sin\theta_{Lab}, \qquad 2.67$$

and as a consequence of time reversal invariance for the reaction matrix, we have

$$D_{LS'} = -D_{SL'}$$

$$D_{LL'} = D_{SS'}$$

$$P = A \qquad 2.68$$

3. Experimental Details

3.1) The Cyclotron

The TRIUMF cyclotron is a six-sector, isochronous cyclotron which accelerates H^- ions injected from the ion source. Beam extraction is achieved by passing part or all of the H^- circulating beam through a carbon stripping foil, creating H^+ ions which bend out of the cyclotron into the beam lines. The radial position of the stripper (R) can be adjusted to provide continuously variable energies from 180 up to 510 MeV. The stripper height (Z) can be varied to change the beam intensity up to 1 μA and 100 μA for polarized or unpolarized beam respectively. The unpolarized ion source is of the Ehlers type, giving 1-2 mA at 12 keV. The Lamb Shift polarized ion source (Do71) is capable of giving 1 μA of 75-80% polarized beam at injection. The beam is bunched in packets 1 to 4 ns wide separated by 43 ns.

The general layout of the TRIUMF facility is presented in figure (3.1). The experiments described in this work were performed on beam line 4B (BL4B), which is shown schematically in figure (3.2).

3.2) The Medium Resolution Spectrometer (MRS)

A general layout of the MRS is presented in figure (3.3). The MRS is a 1.4 GeV/c quadrupole dipole (QD) spectrometer with a vertical bend angle of 60° and a solid angle of 1-2.5 msr. The quadrupole is mounted on a track and can be positioned between 1 and 2 m from the target. It is typically set for point-to-point focusing in the non-bend (Y) plane. The dipole is strongly focusing in the bend (X) plane. The combination of these two elements produces an image of the target on an imaginary surface called the focal plane. The standard focal plane detection system consists of

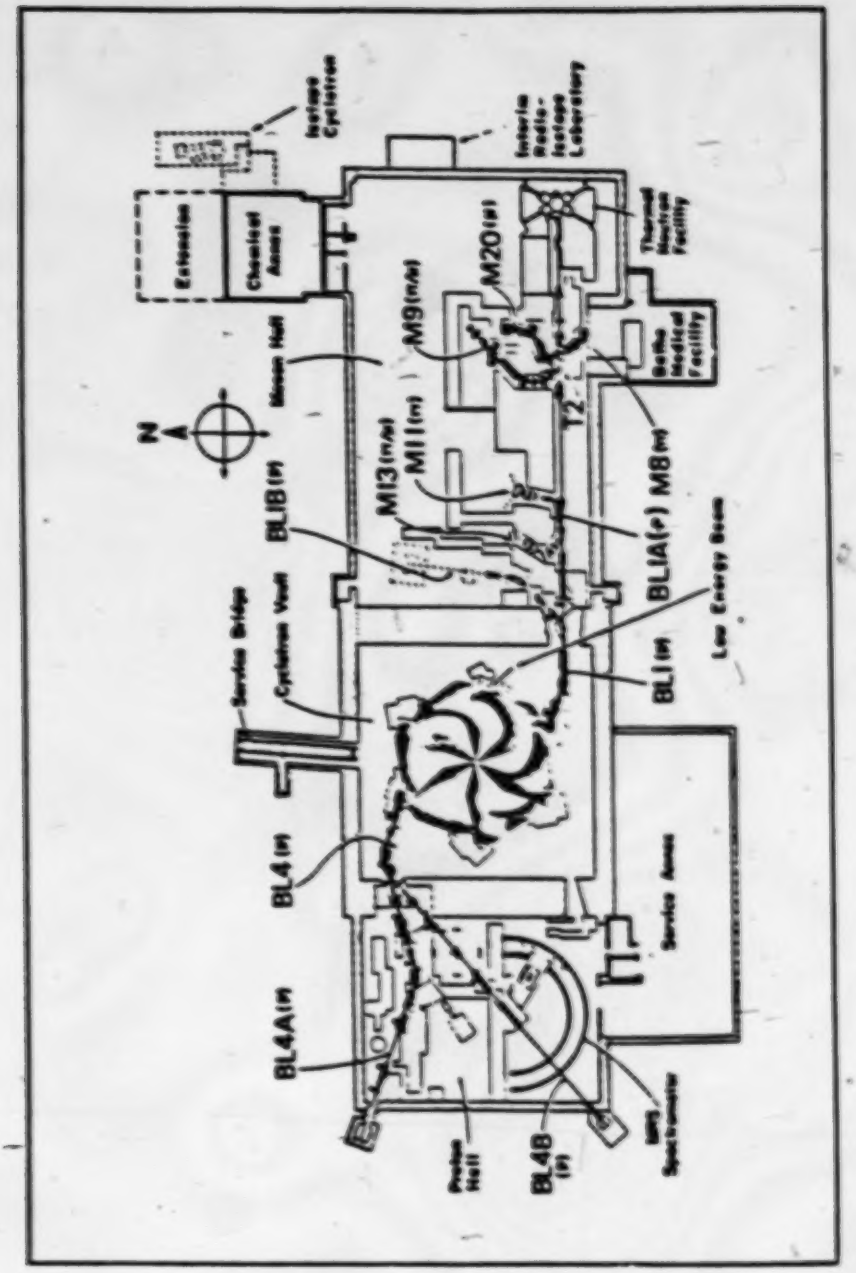

Figure 3.1 General layout of the TRIUMF facility.

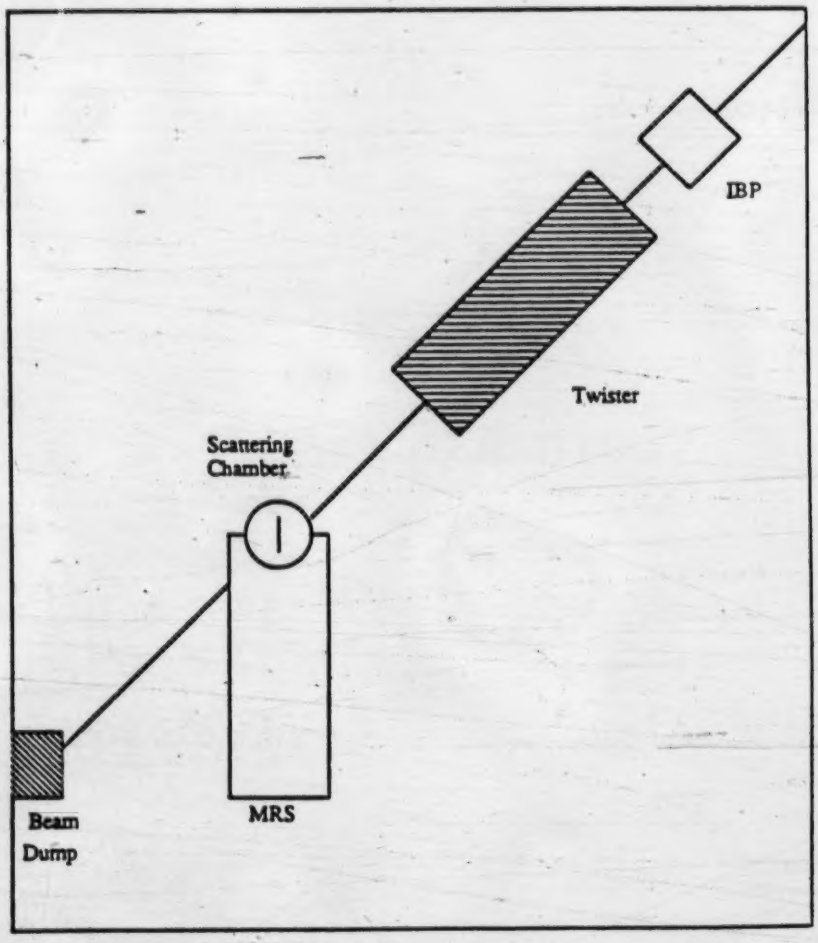

Figure 3.2 A layout of the Proton Hall showing Beam Line 4B.

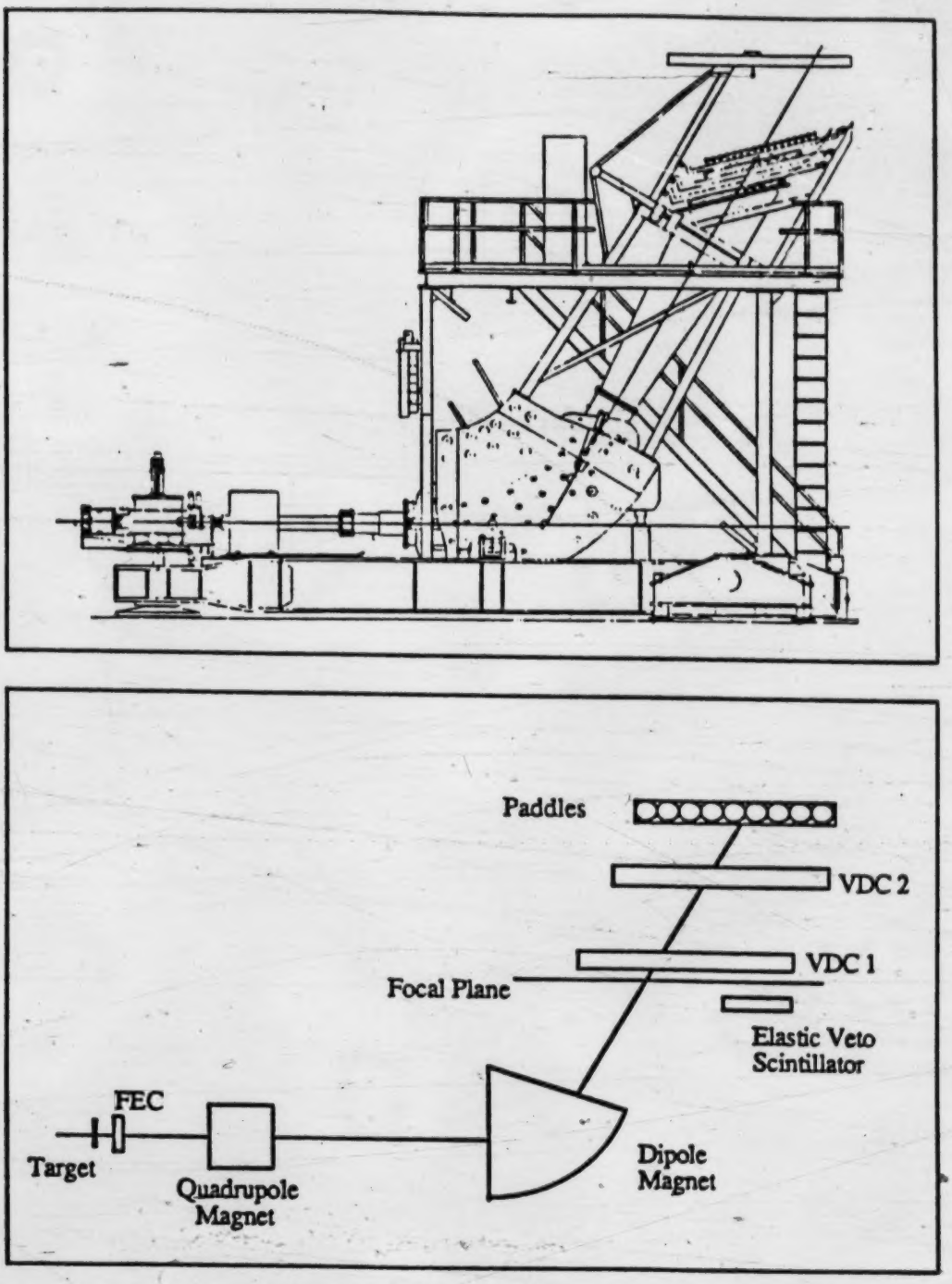

Figure 3.3 A layout of the Medium Resolution Spectrometer.

two vertical drift chambers (VDC1 and VDC2) and a series of segmented trigger scintillators (paddles) placed after the spectrometer. The focal plane is located just below VDC1 and oriented at 45° to the optical axis, parallel to the VDCs.

The coordinates of the trajectories are measured by three sets of wire chambers. The first is located in front of the entrance of the quadrupole, and is called the front end chamber (FEC). It is located directly after the scattering chamber, so it is the first detector to analyze the scattered particles. The FEC is a standard 8cm by 8cm drift chamber which consists of four planes, two in each direction (X and Y). They are labeled X_0, X_0', Y_0, and Y_0'. Each plane consists of sixteen pairs of alternating anode and cathode wires. The primed planes are offset by one half of the anode spacing. This gives an indication of whether the particle passed to the left or to the right of a struck wire and allows position interpolation using drift times. Both the wire number and the drift time are passed on to the computer and a resolution of less than 0.5 mm is achieved. The FEC provides many useful functions. First, it allows ray-tracing back to the target in order to set gates which are used to define the solid angle of the spectrometer and to correct for aberrations in the MRS. Second, the FEC serves, in conjunction with the top scintillators as a trigger for the MRS electronics.

The remaining two wire chambers (VDCs) are located 37 cm apart and about 4 m beyond the exit of the dipole at an inclination of 15° to the horizontal (45° to the Y-Z plane). Each VDC consists of two crossed wire planes which give positions in the X and U (30° to X) direction, this is shown schematically in figure 3.4. The "X" and "U" coordinates provided by the lower and upper VDCs are labeled X_1, U_1 and X_2, U_2, respectively. This information is transformed into X and Y coordinates. Using simple geometric relations based on figure (3.5), one can show that

$$Y = (\sqrt{3})\, X - 2U. \qquad 3.1$$

There are 160 and 176 wires in the VDC1 and VDC2 planes, respectively. The centre wires in the X and U planes (X_{1C} and U_{1C}) cross in the centre of the chamber at the following positions in 50 μm units, 8640 and 10650, respectively. Offsets have to be added to the calculated Y coordinates so they would be in the centre of the VDCs

$$Y_1 = \sqrt{3}\, X_1 - 2U_1 + 2315$$

$$Y_2 = \sqrt{3}\, X_2 - 2U_2 + 2830. \qquad 3.2$$

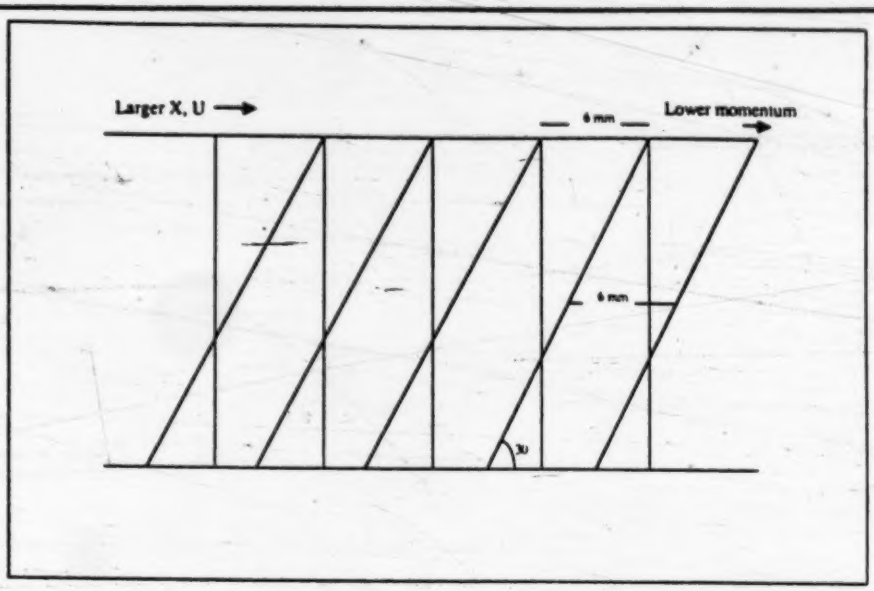

Figure 3.4 Schematic diagram showing the 'X' and 'U' wires in a VDC.

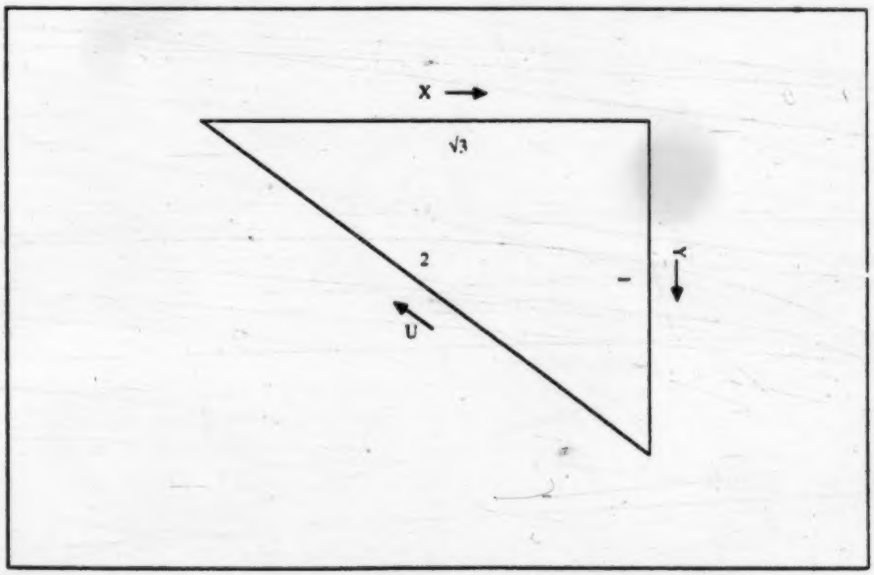

Figure 3.5 Vector diagram showing the calculation of 'Y' from 'X' and 'U' of the VDCs.

Since the X and U planes are not coincident in the z direction, a small correction must be made when calculating Y. Based on the geometry illustrated in figure (3.6), the correction is given by

$$Xcor = (D_1-D_2)\,(XUsep)\,(G)^{-1} \quad , \qquad 3.3$$

with $D_1 = X_1+H$, $D_2 = X_2$ and G is the distance between the VDCs . The correct Y coordinates are then given by the following equations

$$Y_1 = \sqrt{3}\,(X_1-Xcor) - 2U_1 + 2315$$

$$Y_2 = \sqrt{3}\,(X_2-Xcor) - 2U_2 + 2830. \qquad 3.4$$

The VDC information is used to calculate the position of the scattered particle on the focal plane

$$X_F = [GD_1-F(D_1-D_2)]\,[G-(D_1-D_2)\tan(\delta)]^{-1}. \qquad 3.5$$

For ray tracing through the spectrometer, it is necessary to know the particle's trajectory as it crosses the VDCs. This may be specified in terms of the angles

$$\theta = (1/2)[G-H+(X_2-X_1)][H-(X_2-X_1)]^{-1}, \qquad 3.6$$

in the dispersion plane, as illustrated in figure (3.6), and similarly

$$\Phi = (Y_2-Y_1)\,(G^2+(D_1-D_2)^2)^{-1/2} \quad , \qquad 3.7$$

in the transverse plane.

The VDCs and the FEC information may be used to reconstruct the path of the particle back to the target. The calculated coordinates,

$$X_I = a\,X_0+b\,\theta$$

and

$$Y_I = c\,Y_0+d\,\Phi\,, \qquad 3.8$$

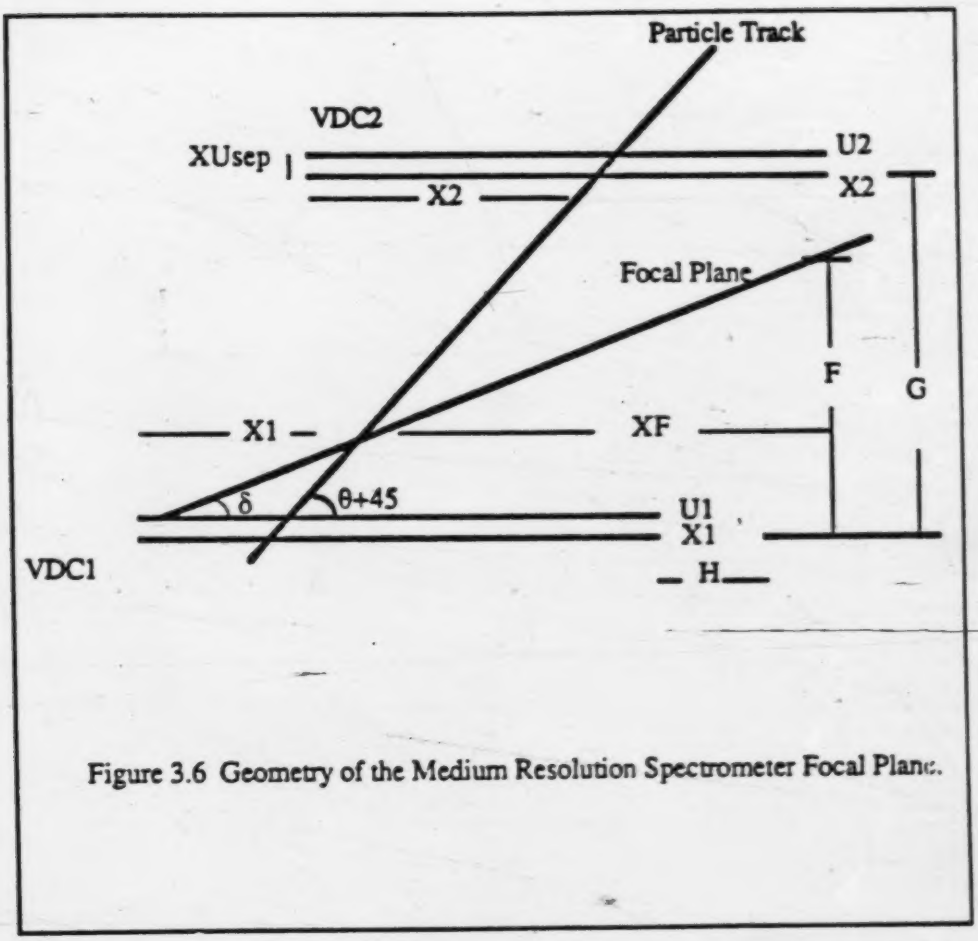

Figure 3.6 Geometry of the Medium Resolution Spectrometer Focal Plane.

refer to the position of the particle at the target. To help reduce the background, the X_I and Y_I coordinates may be constructed to require that any detected particle originate at the target within the beam spot.

The MRS can be rotated about the target position so that angular distributions over the range of angles from 3° to 135° can be measured. The FEC rotates with the MRS while the scattering chamber remains fixed. In the large angle configuration (LAC) a flexible aluminium " bellows " connects the entrance of the FEC to any of the ports of the scattering chamber. These ports are located at scattering angles 28°, 53°, 78°, 103°, 128°, 133°and 152°. The minimum scattering angle attainable in this configuration is 16°. In this mode, the unscattered beam goes through a continuation of the beam pipe, exits through the opposite side of the scattering chamber, passes through the SEM and eventually is stopped in a beam dump located outside the south-west corner of the proton hall.

In the small angle configuration (SAC) the maximum scattering angle attainable is 16°. In this mode, the beam pipe downstream of the scattering chamber must be removed. The quadrupole magnet of the MRS is moved closer to the dipole magnet and a short extension piece " horn " is installed to replace the removed section of the beam line and to connect the scattering chamber to the FEC. The unscattered beam is stopped by a small beam-stop inside the horn. In this mode, the FEC can be installed either inside the horn (before the beam-stop), or after the horn. The former arrangement allows the MRS quadrupole to be closer to the target position, with good resolution and larger solid angle, but results in higher FEC rates at very small angles (less than 5°); the latter allows angles down to 3° but moves the MRS quadrupole and FEC back which worsens resolution.

Located in the dispersion plane above the VDCs, is an array of 6mm thick by 10 cm wide plastic scintillators (paddles) which select the desired momentum acceptance of the MRS.

A veto scintillator paddle is available to prescale the number of events which are accepted from a certain region of the focal plane. This is necessary to suppress strong peaks, such as the elastic scattering peak, which would otherwise make the study of weakly excited states or the continuum impossible. This increases the proportion of interesting data on tape, and reduces the computer dead-time. However, one should note that the counting rate in the focal plane detectors is not reduced by the vetos.

One of the attractive features of the MRS is its relatively large momentum acceptance. For example it is possible to look at a very wide energy range of nuclear excitations (about 45 MeV) with one dipole field setting. This feature allows experimenters to study weakly excited states at large excitation energy without producing background due to elastically scattered protons.

3.3) Dispersion Matching

The beam produced by the TRIUMF cyclotron is momentum dispersed in the horizontal plane, perpendicular to the MRS dispersion plane. If an MRS experiment was performed under these conditions, resolution of a state at some excitation energy would be limited by the energy spread of the beam. Since the beam energy spread is typically 1 MeV or more, depending on the beam tune, the resolution of excited nuclear states would be very limited in this mode of operation.

High energy resolution MRS experiments (typically between 100 and 150 keV) have been performed in the last two years, with the help of the "dispersion matching" technique which makes the energy resolution independent of the energy spread in the incident beam. This principle is illustrated in figure (3.7). It is achieved by rotating the horizontally momentum dispersed beam into the vertical plane by the use of an assembly of six 4 inch quadrupoles known as the "TWISTER". The dispersion matching principle is discussed in more detail in the MRS manual (Hi86), but a brief discussion will be given here.

If a non-monoenergetic electron source were placed at one point P in the focal plane of the spectrometer, the electrons of different momenta would be spread out by amount

$$\Delta X' = (D_s / M_s) (P'_H - P'_L) / P' , \qquad 3.9$$

where D_s (M_s) is the dispersion (magnification) of the spectrometer, P'_H (P'_L) is the highest (lowest) momentum of electrons from the source, and P' is the average momentum of electrons; which is given by

$$P' = (1/2) (P'_H + P'_L) . \qquad 3.10$$

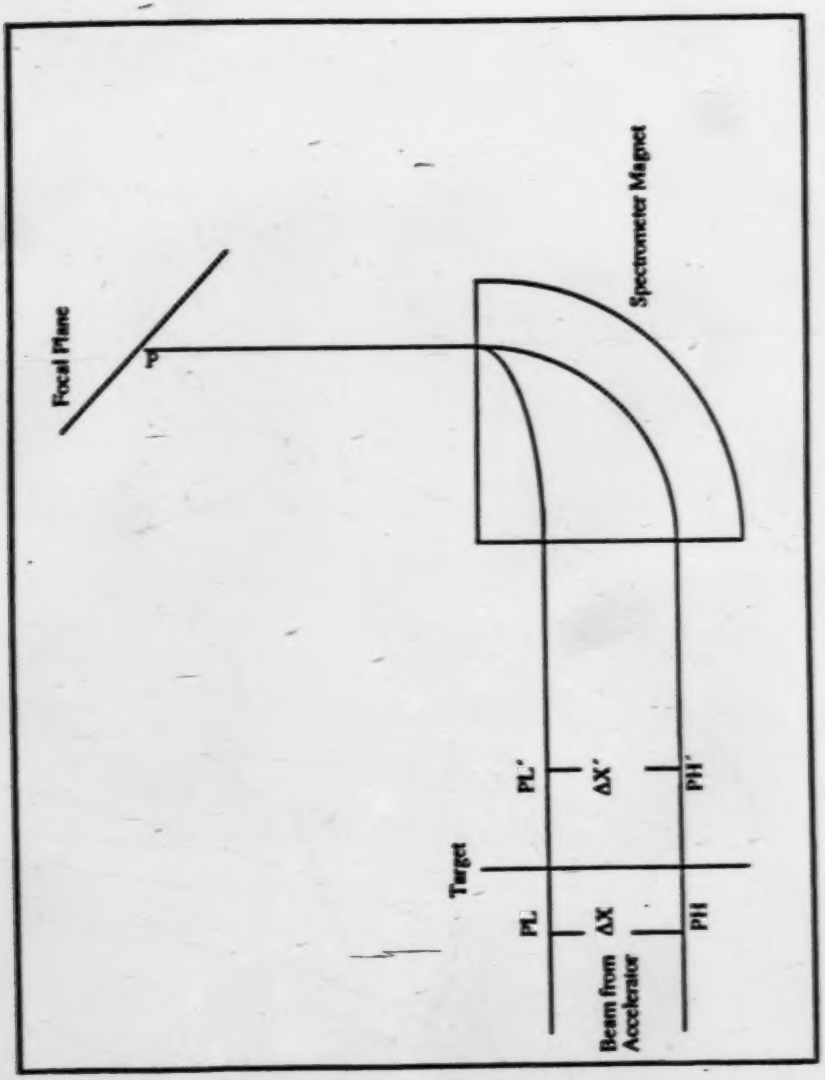

Figure 3.7 Operation of the Medium Resolution Spectrometer with dispersion matching.

By reversing the particle trajectories, we see that the incident beam with momentum spread (P'_H -P'_L) and dispersed by an amount $\Delta X'$ would all focus at the single point P in the focal plane.

Suppose we now let an incident beam with a range of momenta impinge on the target. This beam will be spread out by an amount

$$\Delta X = (D_t) (P_H - P_L) / P , \qquad 3.11$$

where D_t is the dispersion of beam transport system, P_H (P_L) is the highest (lowest) momentum in the incident beam, and P is the average incident momentum. From figure (3.7), if we assume $\Delta X = \Delta X'$ all the particles will focus at one point in P in the focal plane. Based on equations (3.9) and (3.11), the dispersion matching condition can be written as follows

$$(D_t) (P_H - P_L) / P = (D_s / M_s) (P'_H - P'_L) / P' . \qquad 3.12$$

For elastic scattering from a thin target of large mass, $P'_L \approx P_L$ and $P'_H \approx P_H$ and equation (3.12) reduces to

$$D_t = D_s / M_s . \qquad 3.13$$

For the MRS D_s / M_s = -11 cm / % for LAC

$$= -7 \text{ cm} / \% \text{ for SAC.} \qquad 3.14$$

The dispersion condition based on equation (3.13) is usually adequate for any inelastic scattering experiment where the energy loss is small compared to the beam energy. Otherwise, the required dispersion must be computed using equation (3.12). Essentially, the scattered particles must leave the target with dispersion

$$\Delta X' = D_s (\Delta P' / P') , \qquad 3.15$$

and the incident beam must be dispersed appropriately to ensure this.

3.4) Data Acquisition

Data Acquisition is handled by the Computer Automated Measurement and Control (CAMAC) system and the data acquisition program (DACS) using the Eclipse/200 computer in the MRS counting room. A fast microprocessor controls the transfer of data from the CAMAC modules to the Eclipse computer in a buffered mode which in turn records them on magnetic tape for further analysis. A fraction of the events is analyzed on-line to monitor the quality of beam, data and scalers; which would result finally to a shorter and more reliable replay (off-line) analysis.

For the FPP experiments, an on-line J11 starburst microprocessor is used to put some constraints on the FPP data taking, and to analyze a fraction of it on-line; this will be discussed in more detail in section (3.7).

3.5) Event Trigger and Data Stream

The passage of a particle, after being scattered at the target and analyzed by the MRS, with proper correlation in time through a desired set of detectors constitutes an event and generates a trigger signalling the CAMAC electonics modules to read the information about the event. The MRS electronics is illustrated in figure (3.8). The system uses programmable Lecroy CAMAC modules that allow a keyboard command to change the logic for various inputs. A detailed description of the trigger and the meanings of the different variables indicated in the figure is given in both the MRS manual (Hi86) and the DACS handbook (Gr84), but for the sake of completeness a short description will be given.

The timing signals from the scintillator photomultipliers and the outputs of the wire chambers are input into time-to-digital convertors (TDC's). The pulse heights are also fed into amplitude-to-digital convertors (ADC's). The CAMAC system is used to read the scalers, TDC's, and ADC's in the order specified by the user in DACS. When a TDC or an ADC stores an event in its buffer it sends a signal to a device known as the Event Trigger Module to indicate that this has occured, which would

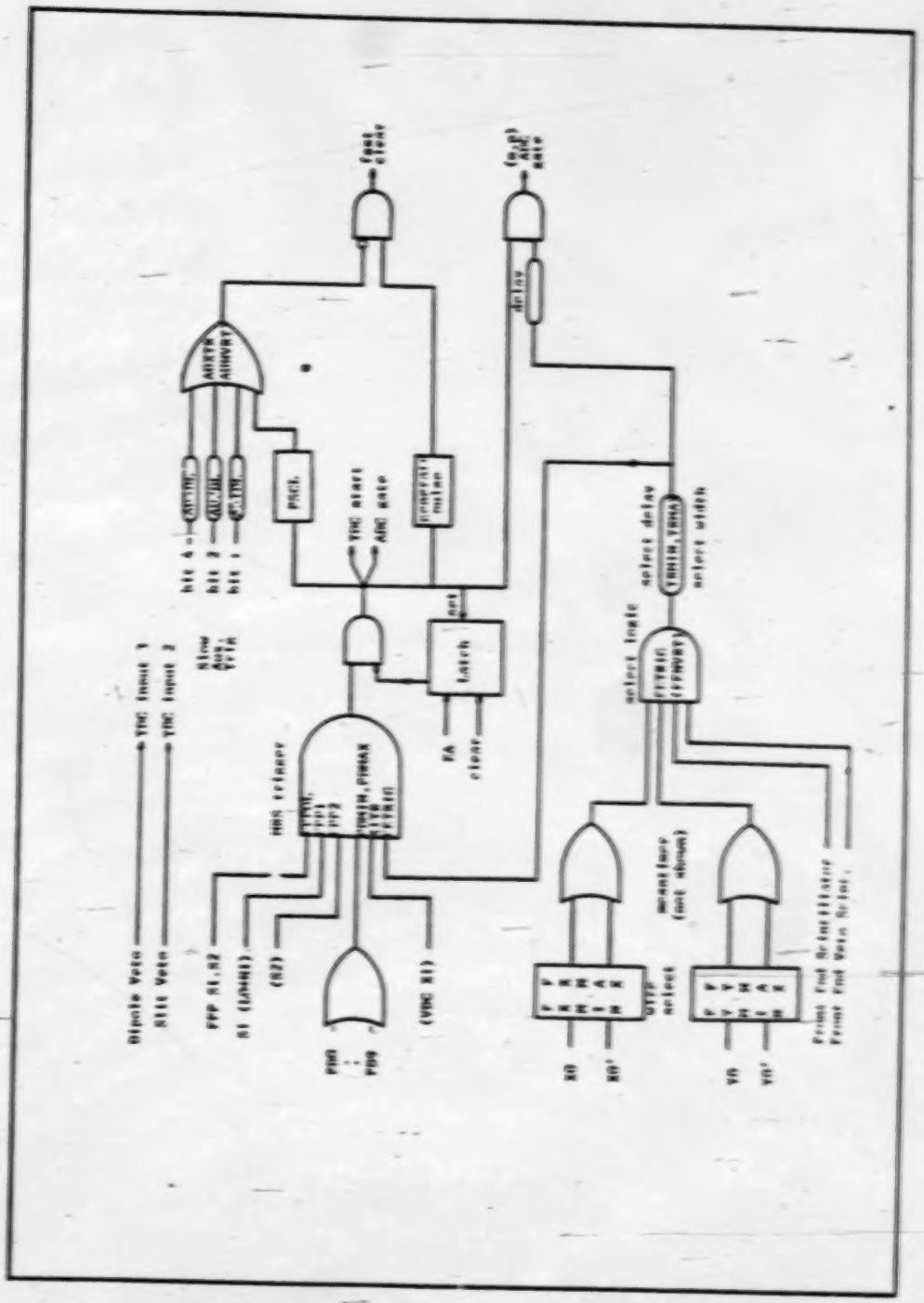

Figure 3.8 A layout of the Medium Resolution Spectrometer electronics.

generate a flag as a signal to the CAMAC to read and clear a buffer in the TDC's and ADC's. This readout can occur simultaneously with the conversion of another event by the TDC and ADC. The CAMAC also periodically receives a message (typically every 5 seconds) from the computer to read the scalers. The TDC's and ADC's cannot simultaneously acquire and digitize signals, so a gate is needed to inhibit data acquisition when conversion for each event (about 12 μs/event) is occuring. This is known as the Computer Busy gate and an event that occurs when this gate is off is refered to as a Trigger.

In the normal MRS mode of operation, a typical data stream usually consists of the following

1) 3 header words (event length, event type, sequence number.)

2) The digital Coincidence Register (DCR) plus a word for the termination code.

3) The 6 TDC signals (usually TTB, TRF, TSLT, TDIP, TTOP, TUSR where SLT and DIP are the slit and dipole veto scintillators, TOP is a signal of the first FPP scintillator S1, and USR is a start to the auxiliary trigger (AUXTR) which turns the veto scintillator on and off), plus a termination code.

4) The 12 ADC signals (usually ESLT, EDIP, PD0, PD1,.....,PD9 where PDn are the trigger paddle scintillators), plus a termination code.

5) A VDC header word plus a word for each of the VDC TDC's that did not time out (this word is variable in length and is handled appropriately by DACS).

In the FPP mode, for each detector plane three timing signals are encoded, the TDC times for each end of the delay line Tl and Tr, and the cathode timing signal Tc. Also encoded are the ADC amplitudes of the two cathode pulses, Eodd and Eeven. The on-line J11 starburst microprocessor computes the delay line time difference (Tl-Tr) and sum (Tl+Tr) for each detector wire plane. The trigger paddle scintillators are usually taken out and replaced by the FPP scintillators S1 and S2. In this mode of operation we have, excluding the paddles, the normal data stream plus the following

1) The eight TDC signals for the delay line time difference and sum for the X planes; (usually WR1X, DR1X,.....,WR4X, DR4X).

2) The eight TDC signals for the delay line time difference and sum for the Y planes; (usually WR1Y, DR1Y,....., WR4Y, DR4Y).

3) The eight TDC signals for the odd drift times for the X and Y planes; (usually TD1X, TD1Y,....., TD4X, TD4Y).

4) The ten ADC pulses for the odd cathode wires in the X and Y planes and the first FPP trigger scintillator S1; (usually OD1X, OD1Y,....., OD4X, OD4Y, S1H, S1L).

5) The twelve ADC pulses for the even cathode wires in the X and Y planes and the second FPP trigger scintillator S2; (usually EV1X, EV1Y,....., EV4X, EV4Y, S2LS, S2HS, S2HL, S2LL).
6) The seven TDC signals for the two scintillators and the MRS start signal.
This information is recorded on magnetic tapes by the data acquisition system for further off-line analysis.

3.6) Particle Identification

The pulse height of a scintillator signal is proportional to $(ZE/P)^2$, where Z, P and E are the charge, momentum and energy of the particle, respectively. On the other hand, the time of flight is proportional to $(E/P)^{-1}$. Therefore, a two dimentional spectrum (usually called SPID) of ESUM vrs TTB is used to distinguish particles with different masses and charges; ESUM is the maximum energy lost by the particle in any of the trigger paddles and TTB (Time Top-Bottom) is the time of flight of the particles from the FEC to the paddles.

The intense peak seen in figure (3.9) consists of protons with the correct TTB values, so a window must be set around it to select proton events. Other peaks corresponding to other charged particles like pions, deuterons...etc, might exist in the spectrum. The latter should be eliminated by hardware cuts to increase the good event rate on magnetic tape.

3.7) The Focal Plane Polarimeter (FPP)

The focal plane polarimeter shown schematically in figure (3.10) is located at the downstream end of the MRS and is capable of measuring the transverse polarization of the scattered particles over a broad range of momenta. Since the standard detection system (the VDCs) maintains the desired high energy resolution, no compromise between energy resolution and FPP efficiency needs to be made. This allows for the use of a very thick carbon analyzing target to achieve high FPP efficiency. A detailed description of the FPP is given in references (Ha86a, He86).

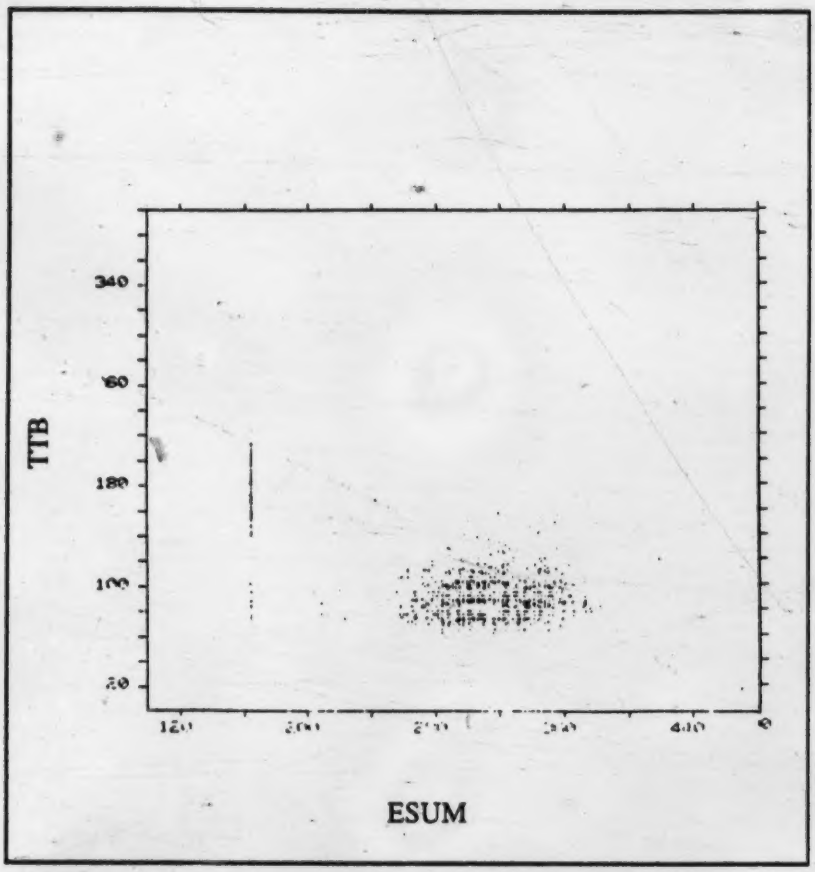

Figure 3.9 A particle identification scatter plot (SPID).

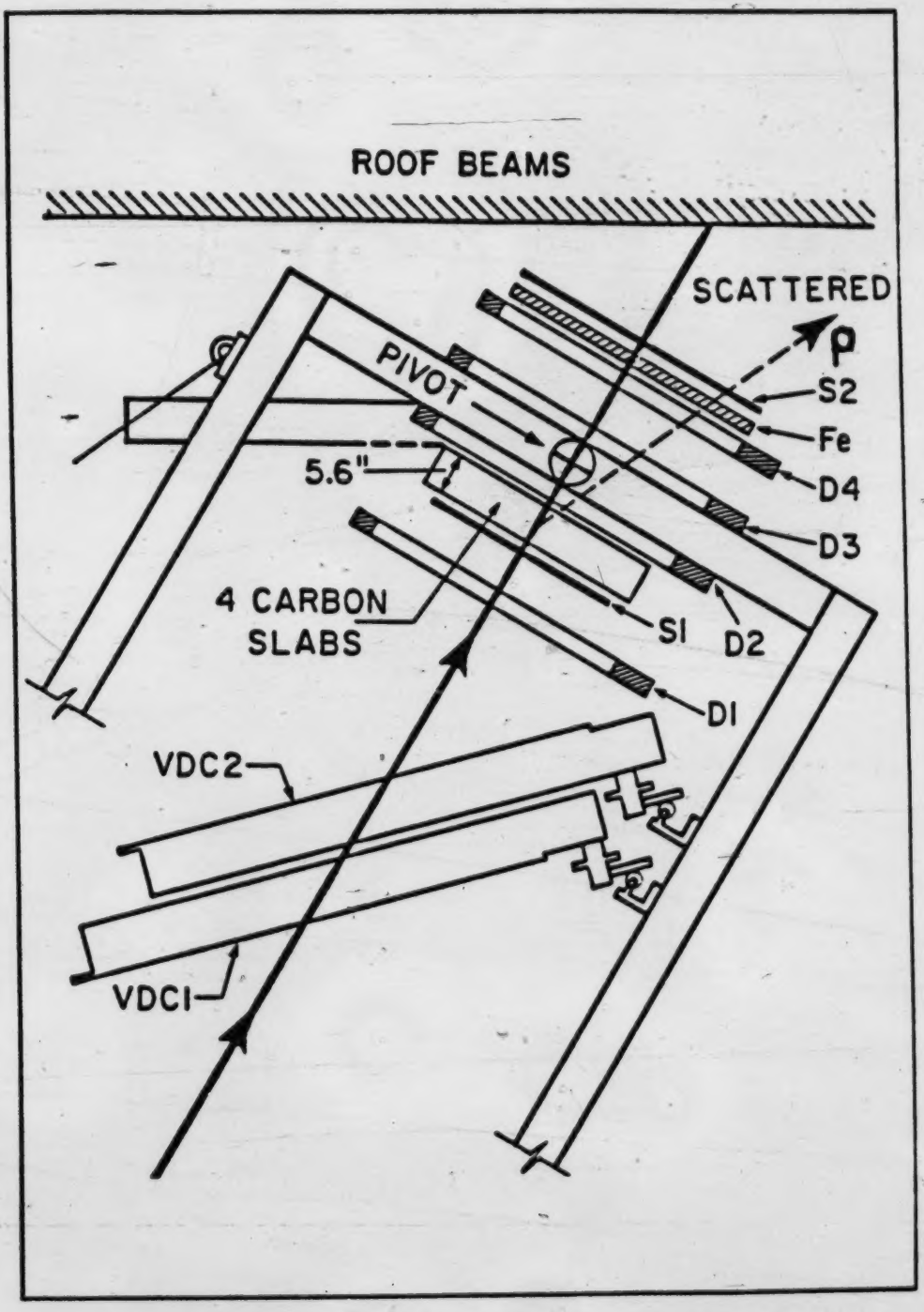

Figure 3.10 A layout of the Focal Plane Polarimeter.

However for the sake of completeness, a brief description will be given here.

The FPP elements are mounted in a cage which can be rotated about a horizontal axis; as illustrated in figure (3.11). The FPP consists of four delay line wire chambers, as many as four slabs of carbon scatterer, a trigger scintillator viewed by two phototubes in front of the scatterer, a mount for steel absorber plates (used for deuteron experiments only), and a large final scintillator viewed by four phototubes . The coordinates are chosen along the optical axis (Z), parallel to the dipole field (Y), and in the direction of the dispersion (X). In the normal "proton" mode chamber D1 is separated from chamber 2 by 40 cm, with the carbon scatterer immediately in front of the latter, with chamber 3 and 4 following with successive 20 cm separations. The wire chambers have active areas of 89 cm by 49 cm and consist of 110 and 60 active anode wires in the X and Y directions, respectively. The four delay line chambers together with the VDCs are used to determine the directions of incoming and scattered protons.

The carbon analyzer is a set of four carbon slabs of different thicknesses, the number of these slabs can be adjusted for the needs of a particular experiment (up to a thickness of 15 cm). The thickness of carbon chosen for a given measurement depends on the energy of the scattered protons. It is desired that the carbon analyzer be as thick as possible in order to maximize the number of protons scattered. A limit on the thickness is given by the magnitude of the multiple-Coulomb-scattering angle, which increases with the carbon thickness. One does not want the angular range dominated by multiple-Coulomb-scattering events to infringe on the angular range where the inclusive analyzing power and cross section for nuclear scattering events is large. For TRIUMF energies, the angular distributions of the scattered events for scattering angles between 5 and 20 are used to obtain simultaneously the polarization components normal and sideways relative to the scattering plane.

The on-line J11 starburst microprocessor is used to perform few tests on the FPP data. A "good " event is one which has satisfied the following tests. First, a test for a pulser-generated event, second, a software prescaler test which is set to pass one of n events unconditionally, and third, tests for scattering angle and collinearity, plus checksum tests on each plane. The checksum test is the difference between the drift time as measured from the cathode time signal (corrected for propagation time along the bus line) and the measured average of times from the two ends of the delay line. Multiple track events are those in which the signal at one end of the delay line is due to one track and that at the other end is due to another. These events will fail the

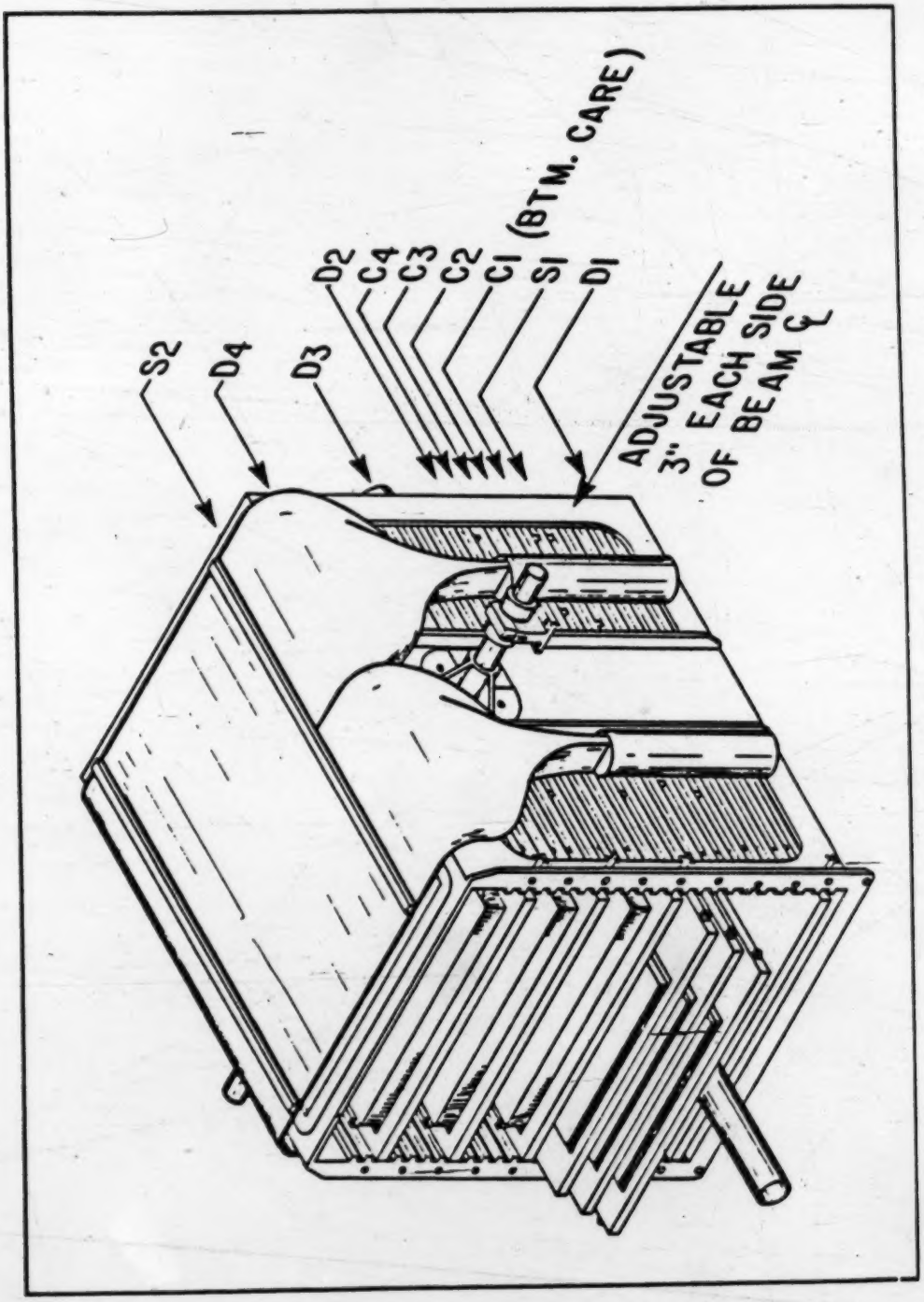

Figure 3.11 The Focal Plane Polarimeter Cage Assembly.

checksum test. The scattering angle test is performed on the delay line time differences with an on-line resolution of ±4 mm corresponding to the anode wire spacing. The linear combinations are

$$X124 = X1 - 2X2 + X4$$

$$Y124 = Y1 - 2Y2 + Y4\,, \qquad 3.16$$

(where Xn is the bend plane coordinate of wire chamber n, and similarly for the Y-direction) is zero if no scattering occured in the carbon, and is used as a test of scattering angle. If the sum of the squares of deviations in the X and Y directions is less than a specified amount the event is rejected as "bad". The third test, a straight line test of the X and Y coordinates for chambers 2, 3, and 4

$$X234 = X2 - 2X3 + X4 \qquad 3.17$$

$$Y234 = Y2 - 2Y3 + Y4, \qquad 3.18$$

it is intended to catch those multiple track events in which the "false" track had a much shorter drift time than the "true" track, so that it was the first signal to reach both ends of the delay line. The most common cause of an event being rejected is that the scattering angle is too small, for which the processing time (including TDC conversion time) is 460 μs. The maximum time required to determine that an event is "good" is about 1100 μs, which happens for only 10% of the events. This should be compared with the nearly 3 ms spent by the computer to read and process it.

3.8) Beam Monitors

The measurement of cross sections, requires the precise knowledge of the total integrated charge. There are three different ways to obtain such information for experiments performed on BL4B. The first is the in-beam Polarimeter (IBP), then the secondary electron emission monitor (SEM), and the third is the Faraday cup (FCUP). The beam polarization is continuously monitored by the IBP.

The IBP uses free p-p scattering from a polyethylene target to monitor both the beam polarization and beam current. The polarimeter layout is illustrated in figure (3.12). On either side of the beam line a pair (L1.L2 or R1.R2) of scintillators detect elastically scattered protons at 17°. Each of these telescopes is in coincidence with it's recoil counter (L3 or R3, respectively). L3 and R3 are located at 70° on either side of the beam line. Triple coincidences (L1.L2.L3 and R1.R2.R3) are called prompts (consisting of real plus randoms) and are counted. To measure the contribution of random events (acc), coincidences between these same sets of detectors, but with L3 and R3 delayed by 43 nsec, are also counted. This delay ensures that the protons come from different beam bursts. Seperate runs with a carbon target in the IBP allows for corrections due to the carbon content in the polyethylene target to correct for $^{12}C(p,2p)$ events. The "sum of events" in the normal direction is defined as

$$Sum = L(real) - L(acc) + R(real) - R(acc). \qquad 3.19$$

This number should be proportional to the integrated beam charge (beam flux), it is listed in table (3.1) for some of TRIUMF energies. The polarimeter asymmetry is given by

$$\varepsilon = [\{ L(real) - L(acc)\} - \{R(real) - (Racc)\}] / Sum. \qquad 3.20$$

The beam polarization is then given by

$$P_B = \varepsilon / A_{yp} \pm (1 / A_{yp}) . \sqrt{\{(1- \varepsilon^2) / (Sum)\}}, \qquad 3.21$$

where A_{yp} is the analyzing power of polyethylene. A_{yp} depends on energy, and it is calculated empirically as a function of the analyzing power of H (A_y (H)). It is given by the following formula

$$A_{yp} = A_y(H) [1.0830 - (T_p/100) (0.07486 - (T_p/100) 0.00823)], \qquad 3.22$$

where T_p is the proton incident energy, and A_{yp} is listed in table (3.1) for TRIUMF energies. The values of $A_y(H)$ are given by the phase shift analysis program SAID

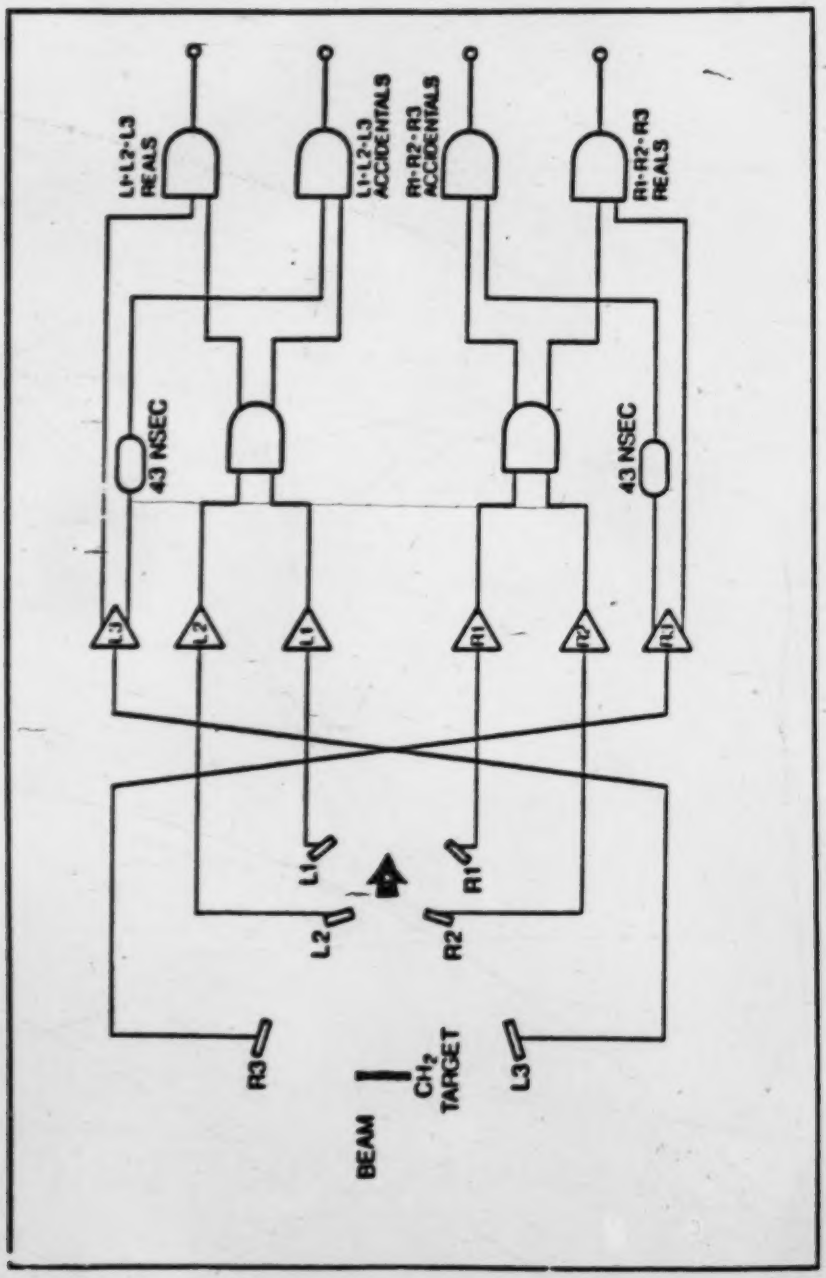

Figure 3.12 Arrangement of the In-Beam-Polarimeter scintillator-photomultiplier detector and electronics assembly.

Table 3.1

Beam normalization values for beam line 4b (4BLB) in-beam polarimeter:

T_p (MeV)	(L+R)*	A_{yp}	SEM
200	46.9	0.283	10.82
250	49.7	0.327	9.467
300	52.6	0.370	8.514
350	55.4	0.414	7.869
400	60.1	0.433	7.346
450	64.9	0.449	6.947
500	69.7	0.466	6.639

* this is in units of counts/sec.nA.(mg/cm^2)

Two corrections of the beam polarization calculated in equation (3.21) are usually needed. First, is the spin-off (unpolarized) correction factor

$$\varepsilon_{corr} = \{ \varepsilon_{on} + \varepsilon_{off}) / (1 + \varepsilon_{on} \cdot \varepsilon_{off} \} \qquad 3.23$$

This correction factor could be very large if the beam tune is poor . Since a CH_2 target was in place instead of pure hydrogen, the $^{12}C(p,2p)$ reaction can contribute, so a small carbon correction factor is needed. A seperate run with a carbon target in the IPB instead of the CH_2 is needed. The final correction of the carbon can be written as

$$\varepsilon_{corr}(H) = P \cdot A_y(H) = \{ \varepsilon_{corr} + \varepsilon_c) / (1 + \varepsilon \cdot \varepsilon_{corr} \} \qquad 3.24$$

with

$$\varepsilon_c = \{ N_L(C) - N_R(C) \} / \{ N_L(C) + N_R(C) \} \qquad 3.25$$

where $N_X = X(C) - X_{ac}(C)$.

The beam current monitor (in LAC) is the SEM. The SEM collects (negative) electrons from surface emission as the protons pass through several aluminum foils. The number of electrons given off is proportional to the stopping power (dE/dx) and is independent of the foil thickness. The SEM rates normalized to the Faraday Cup are listed in table (3.1)The SEM is located downstream of 4BT2 just in front of the beam dump. Care must be taken to focus the beam through the SEM using the cleanup quadrupoles (and beam centered on the beam profile monitor 4BM8). In SAC, the SEM is not used, and instead the beam is stopped by a copper block; which is positioned on a trolly that rolls on the small angle configuration horn floor, therefore remaining at a fixed angle (0°) with respect to the beam direction; and electrons emitted are collected.

3.9) Experiments 272 and 335

Experiment 272 is a study of the $^{24}Mg(p,p')^{24}Mg^*$ reaction at 250 MeV. This

experiment represents the first measurement of the spin-flip probability $S_{NN'}$ at TRIUMF. It was carried out in two phases during the months of September and June of 1985. The first and second phases were measurements of $S_{NN'}$, P, A_y and $d\sigma/d\Omega$ at 2.9° and 6.55°, respectively.

The major difficulty of this experiment consists in the fact that a large number of events from the target need to be accumulated to achieve good statistics, although they constitute only a small fraction (about 10^{-3}) of the protons passing through the MRS, because of the low efficiency of the FPP system. Several experimental steps were taken to overcome this problem. First, elastic scattering and the first excited states were either scaled down by a large factor using a scintillator at the focal plane, or eliminated completely using a lead blocker, which was installed after the focal plane VDCs and before the FPP detection system. Second, inelastic background was reduced by operating the wire planes of the FEC to define an optimal solid angle for the MRS. This was established by installing masks between the wire planes to elliminate the edges of the FEC mainly at the small angle side, which would result finally into lower rates. Thirdly, careful definition of the spectrometer acceptance using the FEC planes in a coincidence mode which means requiring a hit in each single plane. The fourth step, neutron-induced counting rates in the FP and FPP detectors were reduced by water and polyethlene shielding, which was put around the small angle configuration horn in an attempt to shield against neutrons from the beam stopper. This hydrogenous shielding reduced neutron-induced background rates by about a factor of two.

For the second phase, we used a new on-line J11 starburst microprocessor event analysis program, which enriched the number of good events on tape by a factor of three, however the total event rate could not be pushed beyond a value of typically 50 events/second because of deadtimes imposed by the J11.

For spin flip cross section measurement, several auxiliary runs are necessary for each run. First, the cross sections and analyzing powers were measured at each angle seperately. This is to ensure having a reliable live time estimate to obtain absolute cross sections. Second, the overall normalization was checked using the elementary H(p,p) reaction. This is usually achieved by having a seperate run on a polyethylene target at each corresponding angle. Third, the momentum acceptance of the MRS was measured to be flat within ± 2% over an energy interval of about 40 MeV by stepping the elastic peak from ^{24}Mg across the focal plane. Fourth, the momentum calibration of the MRS was established from the latter data and verified by

comparing measured and known level spacings in $^{12}C(p,p')$. Fifth, the absolute angle calibration was obtained from the relative positions of proton groups from H and ^{12}C at forward angle scattering. The sixth step, the longitudinally polarized component of the beam was estimated to be negligable at 250 MeV by stepping through several turns in the cyclotron and observing the transverse polarization components at 4BT1 using the in-beam polarimeter.

Experiment 335 is a cross-sections measurement for the 11.45 MeV ($\Delta T=1$) and the 9.5 MeV ($\Delta T=0$) 1^+ transitions in the $^{28}Si(p,p')^{28}Si^*$ reaction at 200, 250, 290, 360 and 400 MeV. As in experiment 272, several auxiliary runs for angle calibration and normalization were done, this will be discussed in more detail in chapter four.

4. Data Analysis

4.1) The LISA Data Analysis Program

The LISA data analysis program is used for the offline analysis of this work. LISA is an interactive data analysis program designed to process large amounts of event mode data. Although many of its features are general, the current version of LISA is only capable of decoding MRS type event structure. This type of event structure contains three event types, of which currently only two are in use. Event type 1 contains only scaler information, while event type 2 consists of two parts; the first is a fixed length part for TDC's and ADC's and the second is a variable length part containing the TDC information from the MRS drift chambers.

The experiment can be defined by the user in two FORTRAN routines, they are refered to as the "INSERT" and "EVBEV" routines which are called event-by-event. In these routines, experiment dependent event-by-event transformations of the data are performed, new event coordinates are generated and coordinate corrections are applied.

Many one- and two-dimensional spectra can be defined, linear and complex conditions on the different event coordinates can be generated. During the processing of each event, conditions are tested and the defined spectra can be histogrammed according to the specified conditions. For further description of the LISA data analysis program the reader can refer to the LISA documentaion manual (Fr83).

4.2) Coordinate Corrections

In the replay analysis, corrections are applied to the X_f and θ coordinates to improve the resolution of the focal plane spectrum. The θ coordinate depends on the

momentum of the detected particle and is corrected, to make it momentum independent, according to its position on the focal plane using

$$\theta_{PC} = \theta + a X_F \qquad 4.1$$

By substituting θ_{PC} into equation (3.8), an improved expression for X_I may be written as

$$X_I = a X_0 + b \theta_{PC} \qquad 4.2$$

Several corrections must be applied to the focal plane position X_F to optimize the resolution of the focal plane spectrum. The corrections depend on some combinations of the initial positions (X_I, Y_I) and angles (θ, Φ). The corrected focal plane position is given by

$$X_{FPC} = X_F + a \theta_{PC} + b (\theta_{PC})^2 + c (\theta_{PC})^3 + d (\theta_{PC})^4$$

$$+ e (Y_0) + f (Y_0)^2 + g (X_0) + h (X_0)^2 + k \theta_{PC} (X_0) \qquad 4.3$$

where the coefficients of each of the correction terms are adjustable parameters chosen such that X_{FPC} is independent of the correction coordinates, as illustrated in figures (4.1) and (4.2). The optimum correction coefficients are calculated automatically with the FFIT routine (Hi85) contained in the LISA software package. When the data is replayed with these corrections, the focal plane spectrum X_{FPC} is histogrammed with optimum resolution.

4.3) Angle calibration

Determination of the exact scattering angle relative to the beam axis is an important constraint on a precise scattering experiment. The front-end chamber in the MRS defines the solid angle for the scattering process. The Y_0 plane defines the scattering plane, its maximum width is 1600 channels, where each channel corresponds to 0.005 cm. It would be nice if the centre of the chamber corresponds to

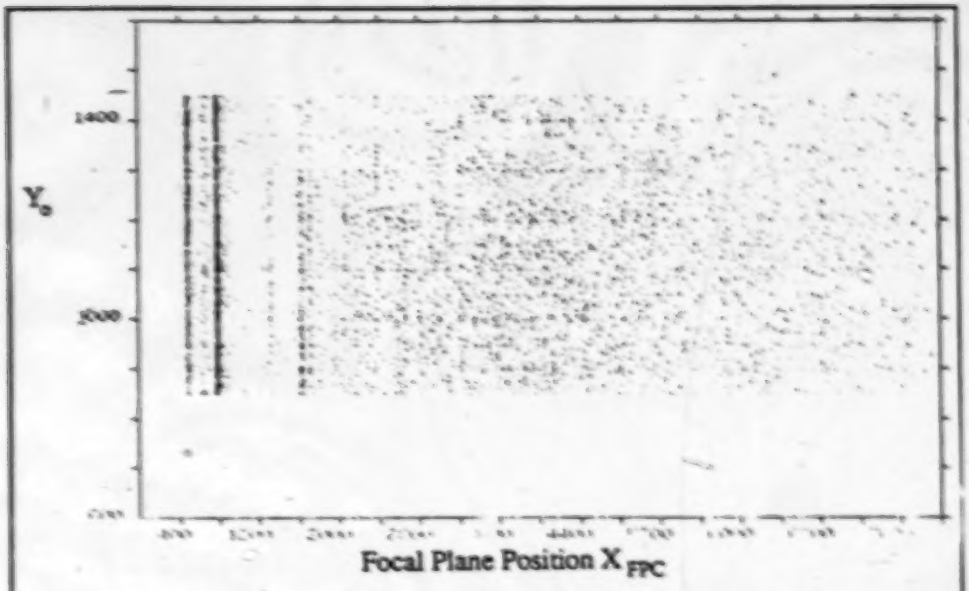

Figure 4.1. Spectrun showing independence of focal plane position on Y_0

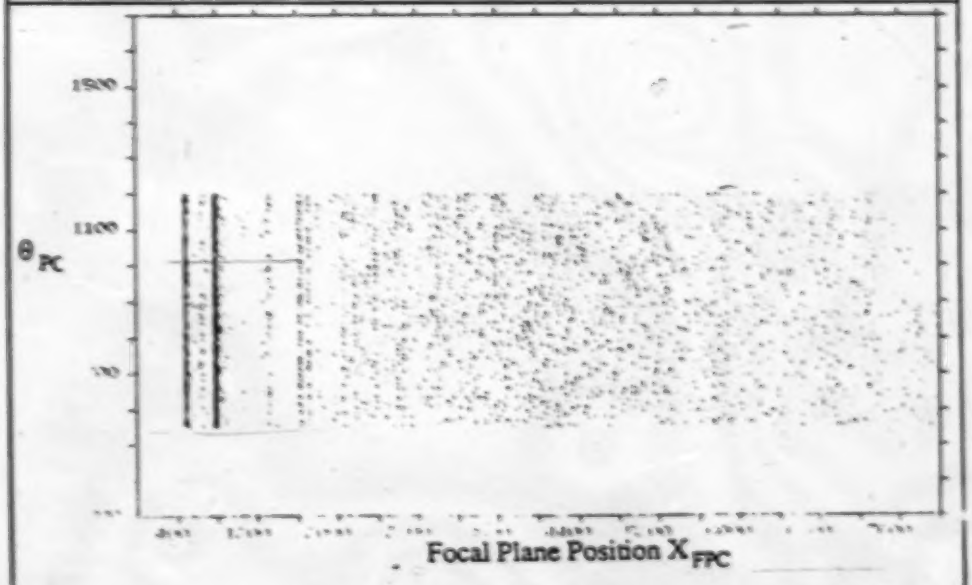

Figure 4.2. Spectrun showing independence of focal plane position on θ_{PC}

the right MRS angle, but it is not usually the case. Thus, the real setting for the MRS angle has to be calculated.

Data from the CH_2 normalization runs were used to calibrate the angular position of the MRS relative to the beam axis by measuring the energy difference of the scattering from protons and carbon nuclei in the polyethelene target. The energy difference is dictated by the reaction kinematics governing the two processes. At a certain forward angle, the energy of a proton scattered in the pp elastic scattering reaction is equal to that of a proton which excites a certain lowlying state of carbon like the 2^+ state at 4.44 MeV or the 1^+ state at 15.11 MeV. The kinematics of the two reactions at an incident energy of 250 MeV, are illustrated in figure (4.3).

An experiment with a CH_2 target in place was performed at the crossing angle between pp elastic and a certain carbon excited state. In the replay analysis, two methods were used to find the crossing angle. The first method, a two dimensional spectrum of Y_0 varsous X_F was histogrammed, and hence the crossing point was observed. The second approach, the data was divided into small angular bins and the two peaks were resolved in order to find the Y_0 channel which corresponds to the crossing angle. With this knowledge, the angle of any other Y_0 channel, or the centre of some Y_0 bin, may be calculated directly from the target-FEC geometry.

4.4) Normalization

The front-end chamber determines the solid angle acceptance of the MRS. It is often not necessary to normalize the data to other states of known cross sections like pp elastic. Auxiliary runs with a CH_2 target to obtain pp elastic cross section at different angles are usually done to compare them with known experimental data or with those calculated from phase shift analysis programs like SAID (Ar84). The uncertainty is usually within (5-10%).

4.5) Determination of Overall MRS Efficiency

Any complex detection system which consists of many elements does not

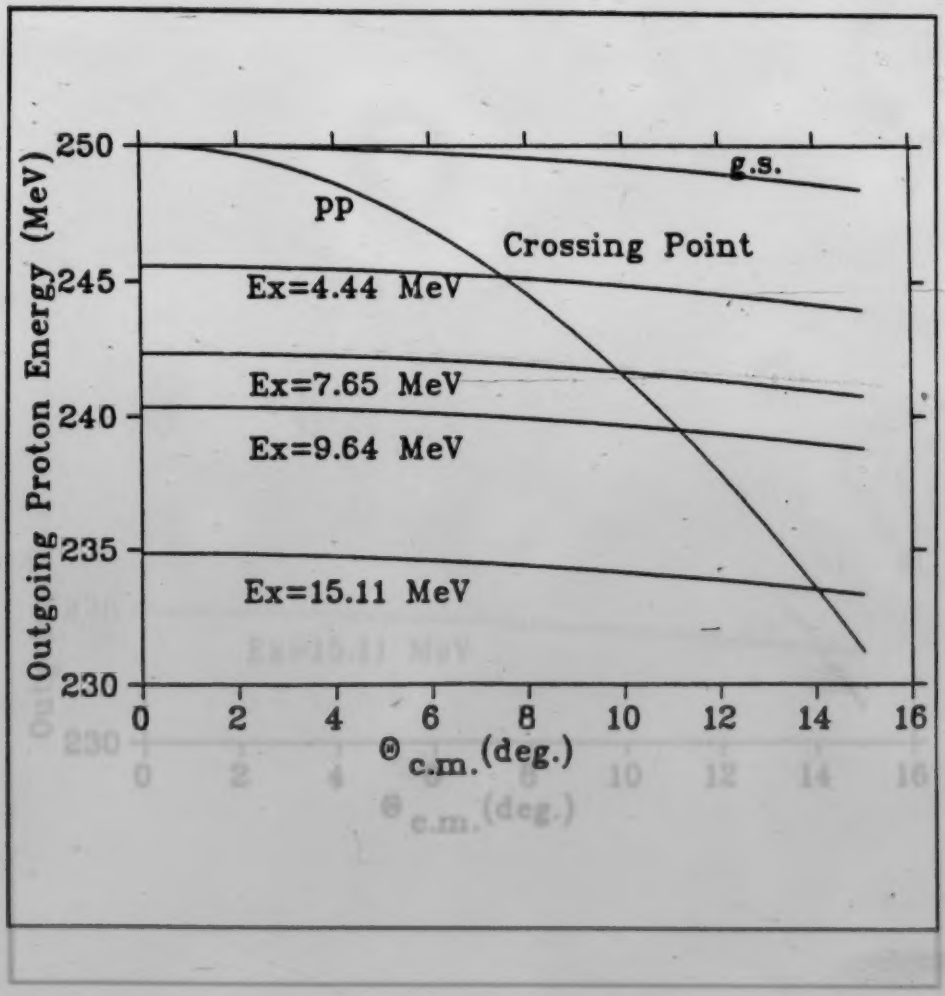

Figure 4.3 Energy of outgoing proton after scattering from a polyethelene target at 250 MeV.

have a 100% efficiency. The MRS detection system consists of two vertical drift chambers and a front end-chamber with six wire planes namely X_0, Y_0, X_1, X_2, U_1 and U_2 .The detailed calculations of the overall effeciency is given in the following references (Hi86 and Mi86), but for the sake of completeness a brief discussion will be given.

When a particle passes through a set of detectors {A, B, C, D...}, the overall efficiency of the detector system ε is defined as the probability that the particle is detected by all of the detectors in the set. This may be determind from the individual detector efficiencies { ε_A, ε_B, ε_C, ε_D...} using

$$\varepsilon = \varepsilon_A \varepsilon_B \varepsilon_C \varepsilon_D \cdots \qquad 4.4$$

assuming that there are no correlations between the detector inefficiencies.

It is possible to determine an individual detector efficiency by measuring the probability that it detects a particle which is also detected by all of the other detectors in the set. For example, the efficiency of detector A is given by

$$\varepsilon_A = [A \cdot B \cdot C \cdot D...] \; / \; [B \cdot C \cdot D...] \; , \qquad 4.5$$

where $\cdot$ represents the logical "and" operation. Assuming that the paddles are 100% efficient, the overall efficiency of the MRS is given by

$$\varepsilon_{MRS} = \varepsilon_{X0} \varepsilon_{Y0} \varepsilon_{X1} \varepsilon_{X2} \varepsilon_{U1} \varepsilon_{U2} \cdot \qquad 4.6$$

Following equation (4.5), the effeciency of the FEC for detecting protons is given by

$$\varepsilon_{FEC} = [X_0 \cdot Y_0 \cdot X_1 \cdot X_2 \cdot U_1 \cdot U_2 \cdot PROT] \; / \; [X_1 \cdot X_2 \cdot U_1 \cdot U_2 \cdot PROT], \qquad 4.7$$

where PROT refers to the condition that the detected particle is identified as a proton. The efficiencies of the upper VDCs { X_1, X_2, U_1, U_2} may be calculated similarly, usually they are of the order of 99% individually. During the data acquistion, it is necessary that the MRS trigger requirement be set to (X_0 or Y_0) and assume that this will cause the MRS to trigger on all scattering events.

4.6) Calculations of Measured Observables and Uncertainities

4.6.a) Differential Cross Section and Analyzing Power

The measured differential cross section is given by

$$d\sigma/d\Omega = N \cdot [\, LT \cdot \varepsilon_{MRS} \cdot d\Omega \cdot T_{THX} \cdot F \,]^{-1}, \qquad 4.8$$

where, N is the number of counts in the peak of interest in the focal plane spectrum, LT is the computer live time during data taking which is calculated as the ratio of the number of pulser events recorded by the computer to the number presented to it, ε_{MRS} is the overall MRS efficiency, $d\Omega$ is the solid angle acceptance of the MRS calculated from the target-FEC geometry based on cuts on the X_0 , Y_0 . T_{THX} is the target thickness which is given in nuclei per unit area, and F is the incident beam flux which is determined from the IPB (see equation 3.19).

The polarized differential cross section depends on the beam polarization P and the analyzing power of the target A_Y

$$(d\sigma/d\Omega)_p = (d\sigma/d\Omega)_0 [\, 1 + P \cdot A_Y \,] \qquad 4.9$$

where $(d\sigma/d\Omega)_0$ is the unpolarized differential cross section, the up and down differential cross sections are given accordingly by

$$(d\sigma/d\Omega)_u = (d\sigma/d\Omega)_0 [\, 1 + P_u \cdot A_Y \,] \qquad 4.10$$

$$(d\sigma/d\Omega)_d = (d\sigma/d\Omega)_0 [\, 1 - P_d \cdot A_Y \,] \qquad 4.11$$

One can solve equations (4.10) and (4.11), for the unpolarized differential cross section and the analyzing power as follows

$$(d\sigma/d\Omega)_0 = [\, P_d (d\sigma/d\Omega)_u + P_u (d\sigma/d\Omega)_d \,] / [\, P_u + P_d \,] \qquad 4.12$$

$$A_Y = [\, (d\sigma/d\Omega)_u - (d\sigma/d\Omega)_d \,] / [\, P_d \cdot (d\sigma/d\Omega)_u + P_u \cdot (d\sigma/d\Omega)_d \,] \qquad 4.13$$

The beam polarization and its statistical error is given by equation (3.21). The statistical error in the beam polarization is sufficiently small to be ignored. The statistical errors in $(d\sigma/d\Omega)_0$ and A_Y are given by

$$\Delta (d\sigma/d\Omega)_0 = [P_u + P_d]^{-1} [\{P_d \cdot \Delta (d\sigma/d\Omega)_u \}^2 + \{P_u \cdot \Delta (d\sigma/d\Omega)_d \}^2]^{1/2} , \quad 4.14$$

$$\Delta A_Y = [P_u + P_d] [\{(d\sigma/d\Omega)_u \cdot \Delta (d\sigma/d\Omega)_d \}^2 + \{(d\sigma/d\Omega)_d \cdot \Delta (d\sigma/d\Omega)_u\}^2]^{1/2}$$

$$\cdot [P_d \cdot (d\sigma/d\Omega)_u + P_u \cdot (d\sigma/d\Omega)_d]^{-2} . \quad 4.15$$

If we introduce the following assumptions

$$P_u \approx P_d , \quad 4.16$$

$$P_N = (1/2) (P_u + P_d) , \quad 4.17$$

$$\sigma \equiv d\sigma/d\Omega , \quad 4.18$$

then one can write the following

$$\sigma = (1/2) [\sigma_u + \sigma_d] , \quad 4.19$$

$$A_Y = [P_N]^{-1} [\sigma_u - \sigma_d] / [\sigma_u + \sigma_d] , \quad 4.20$$

$$\Delta \sigma = (1/2) [(\Delta \sigma_u)^2 + (\Delta \sigma_d)^2]^{1/2} , \quad 4.21$$

$$\Delta A_Y = [2 P_N]^{-1} [\{\sigma_u \cdot \Delta \sigma_d \}^2 + \{\sigma_d \cdot \Delta \sigma_u\}^2]^{1/2} \cdot [\sigma_u + \sigma_d]^{-2} . \quad 4.22$$

Based on equation (4.8), one can write

$$\sigma_u = N_u \cdot (C_u)^{-1} , \quad 4.23$$

$$\sigma_d = N_d \cdot (C_d)^{-1} , \quad 4.24$$

where

$$C_u = [\, LT \cdot \varepsilon_{MRS} \cdot d\Omega \cdot T_{THX} \cdot F \,]_u \quad , \qquad 4.25$$

$$C_d = [\, LT \cdot \varepsilon_{MRS} \cdot d\Omega \cdot T_{THX} \cdot F \,]_d \quad , \qquad 4.26$$

and N_u , N_d are the number of counts in the peak of interest in the up and down directions, respectively. The statistical errors in the measured up and down differential cross-sections are given by the following relations

$$\Delta^{\circ}\sigma_u = \sigma_u \cdot (1/\sqrt{N_u})$$

$$= (\sqrt{N_u}) / (C_u) \qquad 4.27$$

and

$$\Delta \sigma_d = \sigma_d \cdot (1/\sqrt{N_d})$$

$$= (\sqrt{N_d}) / (C_d) \qquad 4.28$$

4.6.b) Spin-Flip Probability

As illustrated in figure (4.4), an incident proton with polarization directed longitudinally (L), sideways (S), or normally (N) to the scattering plane may scatter by an angle θ with final polarization components along the longitudinal (L´), sideways (S´) or normal (N´) directions in the final state. The sideways (S´) component is unaffected by the magnetic field of the MRS dipole, whereas both N´ and L´ components precess relative to the momentum direction by an angle χ, which is given as a function of the kinetic energy (T) as follows

$$\chi = (\, g/2 - 1) \, \theta_D \, (1 + T / mc^2), \qquad 4.29$$

where g/2 = 2.79276 is the magnetic moment of the proton, and θ_D is the deflection

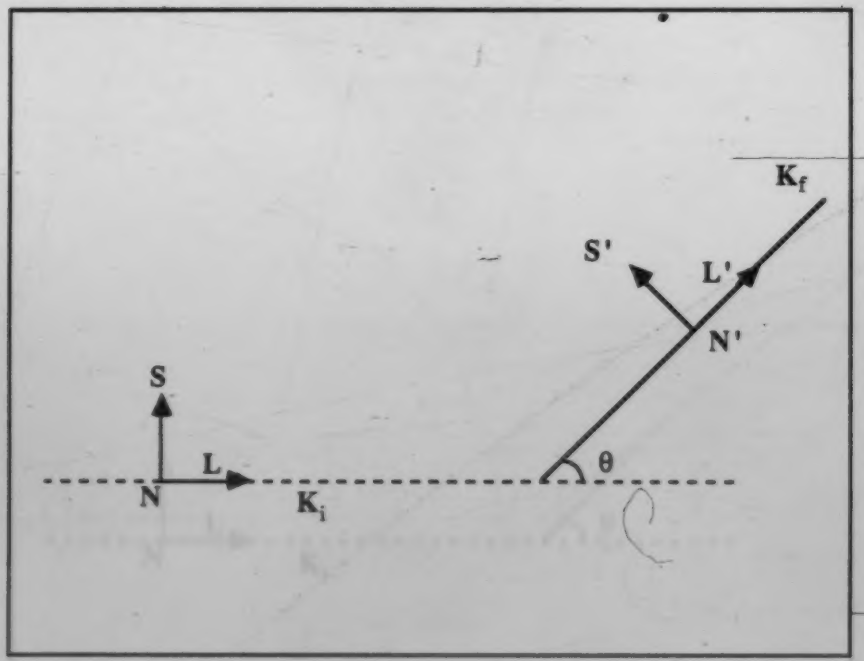

Figure 4.4 Schematic representation of scattering process coordinates

Figure 4.4 Schematic representation of scattering process coordinates

angle in the MRS dipole. With three kinds of polarization transfer and a focal plane polarimeter, a total of five polarization transfer coeffecients can be determined: $D_{SS'}$, $D_{NN'}$, $D_{SL'}$, $D_{LL'}$ and $D_{LS'}$, (terms connecting N with either S′ and L′ are forbidden because of parity conservation). These observables relate the polarization components of the incident proton beam (P_L, P_N, P_S) to those of the scattered beam ($P_{L'}$, $P_{N'}$, $P_{S'}$) through the following relations

$$\begin{aligned} P_{S'} &= [\, P_S\, D_{SS'} + P_L\, D_{LS'}\,] / (1+P_N\, D_{N0}) \\ P_{N'} &= [\, P_N\, D_{NN'} + D_{0N'}\,] / (1+P_N\, D_{N0}) \\ P_{L'} &= [\, P_S\, D_{SL'} + P_L\, D_{LL'}\,] / (1+P_N\, D_{N0}), \end{aligned} \qquad 4.30$$

where

$$D_{0N'} = P(\theta),$$

and

$$D_{N0} = A_Y(\theta). \qquad 4.31$$

The spin-flip probability $S_{NN'}$ is related to the $D_{NN'}$ through the following relation

$$S_{NN'} = (1/2)\,(1 - D_{NN'}). \qquad 4.32$$

It has been shown (Mc84), that with the inclusion of all realistic effects neglected in the assumptions above, the full expressions for $D_{NN'}$ and $P(\theta)$ are

$$D_{NN'} = \{1/(\,2\,P_N \langle\cos\chi\rangle)\}[\, P_{ND}(FP) + P_N\, A_Y\, P_{NS}(FP)\,], \qquad 4.33$$

and

$$P(\theta) = \{1/(\,2\,P_N \langle\cos\chi\rangle)\}[\, P_{NS}(FP) + P_N\, A_Y\, P_{ND}(FP)\,], \qquad 4.34$$

where

$$P_{NS}(FP) = P_N{}^{u}(FP) + P_N{}^{d}(FP)\ , \qquad 4.35$$

and

$$P_{ND}(FP) = P_N^{u}(FP) - P_N^{d}(FP) \quad . \qquad 4.36$$

Here $P_N^{u}(FP)$ and $P_N^{d}(FP)$ are the normal components of the polarization measured at the FPP in the focal plane coordinate system for up and down beam polarization, respectively, and < > refers to the average over events. Since the $P_N^{u(d)}(FP)$ components are measured by the two dimensional wire chambers, certain criterion for the acceptance of the scattered particles in these chambers must be taken into account in order to compute asymmetries. If θ_c and ϕ_c are the polar and azimuthal scattering angles of particles scattered by the carbon analyzer, the distribution of the scattered particles may be written as

$$I(\theta_c,\phi_c) = I_0(\theta_c)\,(\,1 + P_N(FP)\cdot A_c(\theta)\cos\phi_c\,)\,F(\,\theta_c,\phi_c\,)\,, \qquad 4.37$$

where $A_c(\theta)$ is the (inclusive) analyzing power of carbon, and $F(\,\theta_c,\phi_c\,)$ defines the criterion for the acceptance of an event by the FPP with values of

$$\begin{aligned} F(\,\theta_c,\phi_c\,) &= 1; \quad \text{accepted} \\ &= 0; \quad \text{rejected.} \end{aligned} \qquad 4.38$$

If we restrict the accepted trajectories of the scattered particles for a given θ_c to lie within the physical acceptance limits of the wire chambers for all possible values of ϕ_c, we have the so called " Cone Test " as illustrated in figure (4.5). The cone test has no azimuthal dependence, and its dependence on the polar angle is determined by the physical acceptance of the detector system. Since the focal plane polarization component $P_N(FP)$ is the desired quantity, the form of equation (4.37) suggests Fourier analysis as a means to extract it. Proceeding accordingly yields

$$P_N(\theta) = (\,2/\,A_c(\theta)\,)\cdot\{\textstyle\int_0^{2\pi} I(\theta,\phi)\cos\phi\,d\phi\}\,/\,\{\int_0^{2\pi} I(\theta,\phi)\,d\phi\,\}\,. \qquad 4.39$$

Experimentaly, the integrals are approximated by sums over a finite number of events for a given interval of θ. If the analyzing power of the carbon analyzer $A_c(\theta)$ is known for each bin, the weighted average of the polarization in the individual bins may be formed over the acceptance limits for θ_c to yield the final polarization of the scattered particles. It has been shown (Mc84) that for events satisfying the cone test, the $P_N(FP)$ is given by

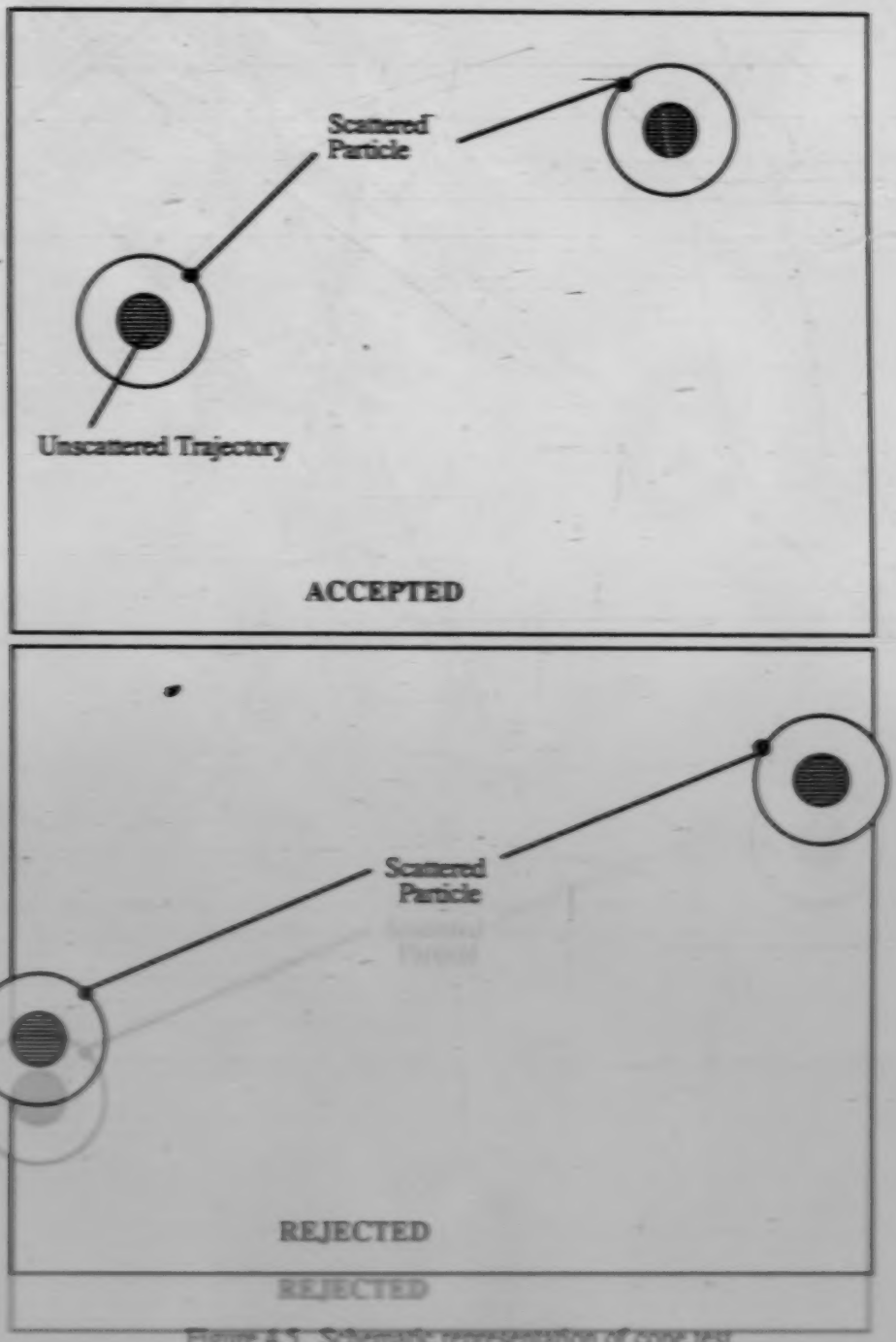

Figure 4.5 Schematic representation of cone test.

$$P_N(FP) = 2\{\Sigma_{ev} I(\theta,\phi) \cos\phi\, A_c(\theta)\} / \{\Sigma_{ev} I(\theta,\phi)\, A_c^2(\theta)\}\,. \qquad 4.40$$

Therefore, the measurement of $P_N^{u(d)}(FP)$ with the acceptance test requires the accumulation of the following sums by the FPP for both normal and reverse beam polarization states

$$\Sigma_{ev} I(\theta, \phi) \cos\phi\, A_c(\theta)$$

and $$\Sigma_{ev} I(\theta, \phi)\, A_c^2(\theta). \qquad 4.41$$

The statistical errors in $D_{NN'}$ and $P(\theta)$ are given by the following equations

$$\Delta D_{NN'} = \sqrt{[\,\{\partial D_{NN'}/\partial P_N^u \cdot (\Delta P_N^u)\}^2 + \{\partial D_{NN'}/\partial P_N^d \cdot (\Delta P_N^d)\}^2 + \{\partial D_{NN'}/\partial A_Y \cdot (\Delta A_Y)\}^2\,]}, \qquad 4.42$$

$$\Delta P(\theta) = \sqrt{[\,\{\partial P/\partial P_N^u \cdot (\Delta P_N^u)\}^2 + \{\partial P/\partial P_N^d \cdot (\Delta P_N^d)\}^2 + \{\partial P/\partial A_Y \cdot (\Delta A_Y)\}^2\,]}. \qquad 4.43$$

Now if we introduce the following quanities

$$T1 = (\Delta P_N^u)^2 \cdot (1 + P_N A_Y)^2\,, \qquad 4.44$$

$$T2 = (\Delta P_N^d)^2 \cdot (1 - P_N A_Y)^2\,, \qquad 4.45$$

$$T3 = (\Delta A_Y \cdot P_N \cdot P_{NS}(FP))^2\,, \qquad 4.46$$

$$T4 = (\Delta A_Y \cdot P_N \cdot P_{ND}(FP))^2\,, \qquad 4.47$$

then one can rewrite equations (4.42) and (4.43) as follows

$$\Delta D_{NN'} = \{1/(2 P_N \langle\cos\chi\rangle)\}\sqrt{(T1+T2+T3)}, \qquad 4.48$$

and

$$\Delta P(\theta) = \{1/ (2 P_N \langle \cos\chi \rangle)\} \sqrt{(T1+T2+T4)}. \qquad 4.49$$

The statistical error in $S_{NN'}$ is given by

$$\Delta S_{NN'} = (1/2) \Delta D_{NN'}. \qquad 4.50$$

The spin-flip cross section ($\sigma S_{NN'}$) is defined as the direct product of the differential cross section σ and the spin-flip probability $S_{NN'}$. The statistical error in $\sigma S_{NN'}$ is given by

$$\Delta (\sigma S_{NN'}) = \sqrt{ [\partial (\sigma S_{NN'}) / \partial \sigma]^2 + [\partial (\sigma S_{NN'}) / \partial S_{NN'}]^2 } \qquad 4.51$$

where

$$\partial (\sigma S_{NN'}) / \partial \sigma = (S_{NN'} \cdot \Delta \sigma)^2, \qquad 4.52$$

$$\partial (\sigma S_{NN'}) / \partial S_{NN'} = (\Delta S_{NN'} \cdot \sigma)^2, \qquad 4.53$$

so one can rewrite equation (4.51) as

$$\Delta (\sigma S_{NN'}) = \sqrt{ (S_{NN'} \cdot \Delta \sigma)^2 + (\Delta S_{NN'} \cdot \sigma)^2 }. \qquad 4.54$$

Systematic uncertainities due to target nonuniformity and errors in beam charge integration usually contribute to the total experimental errors.

5. Results and Comparison with Theory

The study of spin excitations in nuclei has been an active field in the last few years. This study has been performed with different probes like (p,n), (n,p), (p,p´)..... and (e,e´), (Al86, Al87, An84, Dj83, Dj84, Go84,Na85 and references therein). In this chapter we will report results for the ^{26}Mg(p,p´)^{26}Mg* and the ^{28}Si(p,p´)^{28}Si* reactions, carried out with intermediate energy protons at TRIUMF.

This work consists of two different experiments E272 and E335. E272 is a measurement of differential cross sections, analysing powers, polarizations, spin-flip probabilities and spin-flip cross sections for the ^{26}Mg(p,p´)^{26}Mg* reaction at 250 MeV. A typical off-line momentum spectrum for the ^{26}Mg(p,p´)^{26}Mg* reaction is shown in figure (5.1). E335 is a measurement of differential cross sections for the 11.45 MeV (ΔT=1) and the 9.5 MeV (ΔT=0) 1^+ transitions in the ^{28}Si(p,p´)^{28}Si* reaction at 200, 250, 290, 360 and 400 MeV. A typical off-line momentum spectrum for the ^{28}Si(p,p´)^{28}Si* reaction is shown in figure (5.2). First we will present the experimental data then a comparison with theory will follow later in this chapter.

5.1) ^{26}Mg(p,p´)^{26}Mg* Results

Here we present the results of measurements of the spin-flip probability ($S_{NN'}$) for inelastic proton scattering from ^{26}Mg. This measurement was carried out with a 250 MeV transverse polarized beam at the small-angle MRS facility at TRIUMF with the focal plane polarimeter at the Medium Resolution Spectrometer, where the entire excitation energy (E_x) range could be measured at one magnetic field setting up to about 40 MeV. The ^{26}Mg target was 48mg/cm^2 thick. Measurements were taken at two angles in the lab, namely 2.9° and 6.6°. The polarization of the incident beam was continuously monitored with an in-beam polarimeter upstream of the target, typical

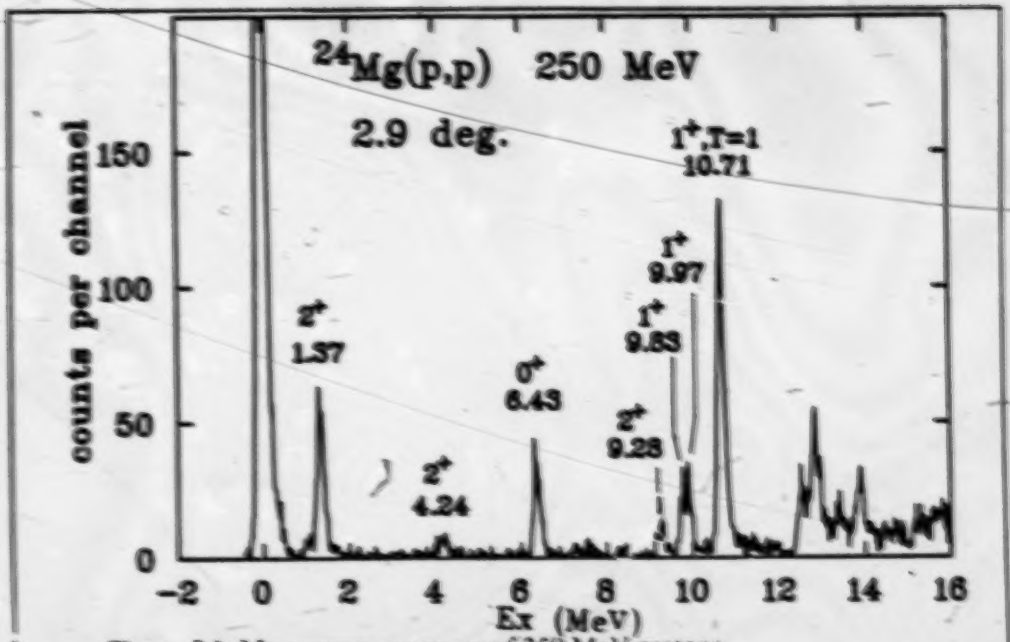

Figure 5.1. Momentum spectrum of 250 MeV protons scattered from ^{24}Mg at θ_{lab}=2.9°.

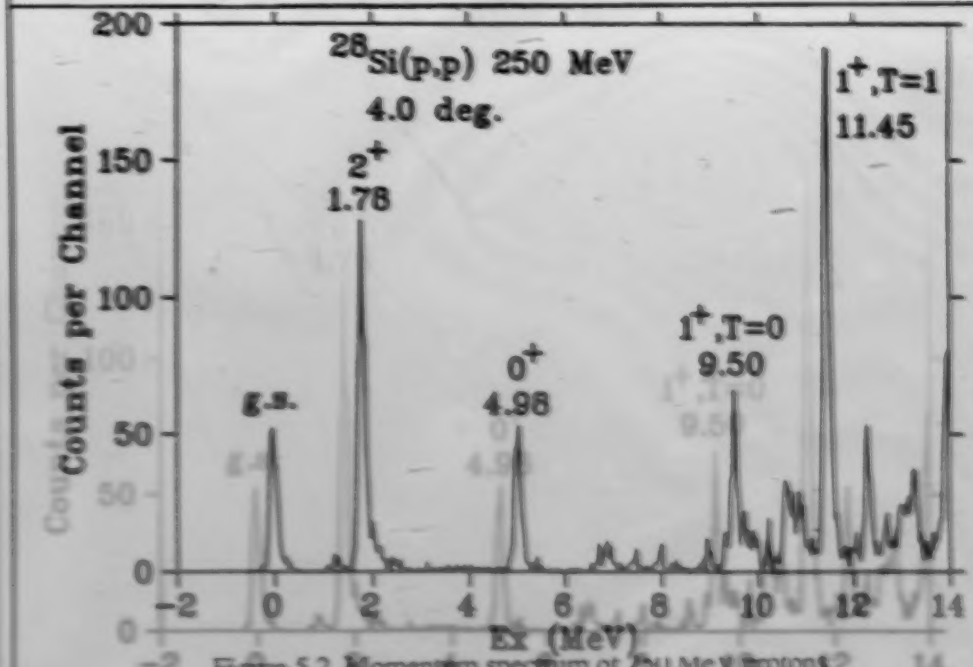

Figure 5.2. Momentum spectrum of 250 MeV protons inelastically scattered from ^{28}Si at θ_{lab}=4°.

values were about 0.75. Systematic errors in the absolute values of $S_{NN'}$ were controlled by doing several auxilliary runs discussed in sections (3.9, 4.3 and 4.4). In addition to the $S_{NN'}$ data of primary interest here, differential cross sections ($d\sigma/d\Omega$), analyzing powers (A_y), and spin-flip cross sections ($\sigma S_{NN'}$) were also measured during the same experiment. These data are listed in Appendix II.

The measured differential cross sections for the (T=1,1⁺) level at 10.71 MeV at both 200 and 250 MeV are listed in appendix AIII. The quoted uncertainity includes only the statistical errors. From frequent inter-comparisons with the reproducibility of individual runs we assess a systematic uncertainty of ±5% to the experimental cross sections. This includes contributions from target nonuniformity and from errors in beam charge integration. The 200 MeV measurement was carried out at the MRS in collaboration with C. Djalali, A. Galonsky and G. Crawley from Michigan State University.

Examples of σ and $\sigma S_{NN'}$ spectra, for ^{24}Mg at 2.9° and 6.6°, are shown in Figures (5.3, 5.4, 5.5 and 5.6). The σ spectra show the standard features of individual nuclear states up to roughly 12 MeV of excitation energy, then giant resonances up to about 20 MeV, and a featureless spectrum beyond. The $\sigma S_{NN'}$ spectra reveal little strength below about 9 MeV, large cross sections with noticeable gross structure up to about 20 MeV, and then flat strength beyond. Examples of P, A_y and $S_{NN'}$ spectra, for ^{24}Mg at 2.9° and 6.6°, are shown in Figures (5.7, 5.8, 5.9 and 5.10). It is clear from the spectra that the equality of P and A for certain discrete natural parity states and the continuum is holding. This agreement is a good indication that the Focal Plane Polarimeter is working well. Also one notices that the slope of the analysing power data versus excitation energies increases with increasing angle.

The $S_{NN'}$ spectra shows that the strong natural parity states with ΔS=0 are suppressed because they have very small spin-flip probability, while as expected, the unnatural parity ΔS=1,1⁺ states around 10 MeV have large spin-flip probabilities about 0.6, then $S_{NN'}$ is almost 0.4 up to 40 MeV of excitation energy. In summary, we have determined for the first time the spin-flip probability for protons scattering from ^{24}Mg over a wide range of E_x at 250 MeV.

Another important observation from the data is the large $S_{NN'}$ values (about 0.4) around 40 MeV of excitation. This gross feature can be explained as arising from quasielastic NN scattering. Also the similarity between the spin-flip spectra in light, medium and heavy nuclei at higher excitation energies is a point worth mentioning and needs to be lookad at more carefully.

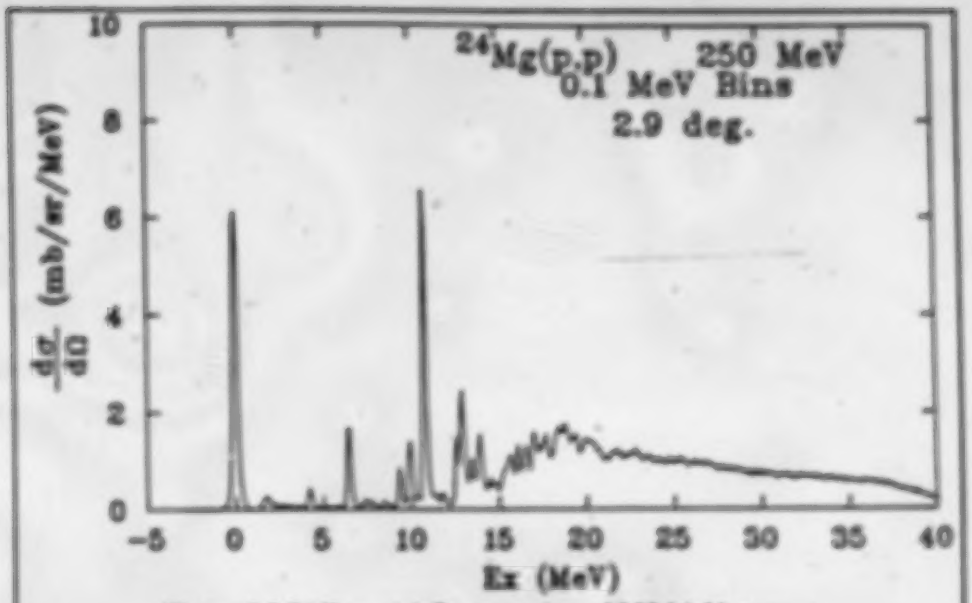

Figure 5.3.Differential Cross section of 250 MeV protons inelastically scattered from ^{24}Mg at θ_{lab}=2.9° .

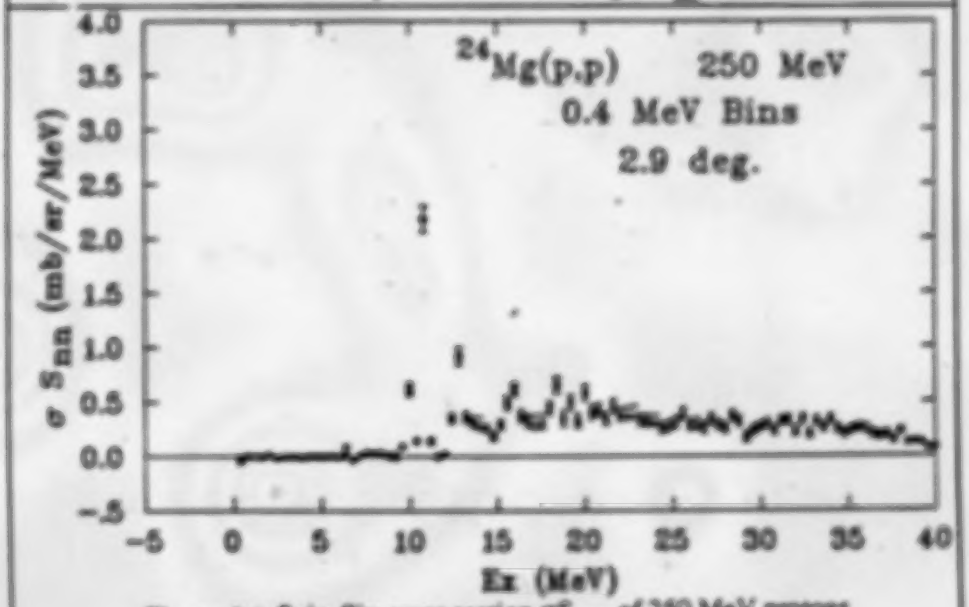

Figure 5.4. Spin-flip cross section σS_{spp} of 250 MeV protons inelastically scattered from ^{24}Mg at θ_{lab}=2.9° .

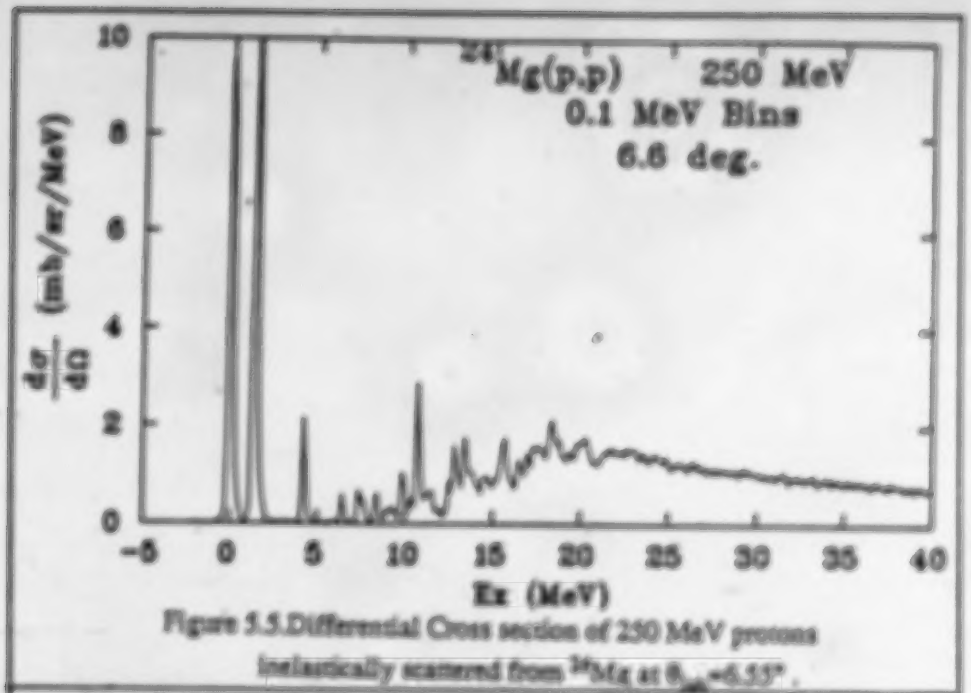

Figure 5.5.Differential Cross section of 250 MeV protons inelastically scattered from ^{24}Mg at θ_{lab}=6.55°.

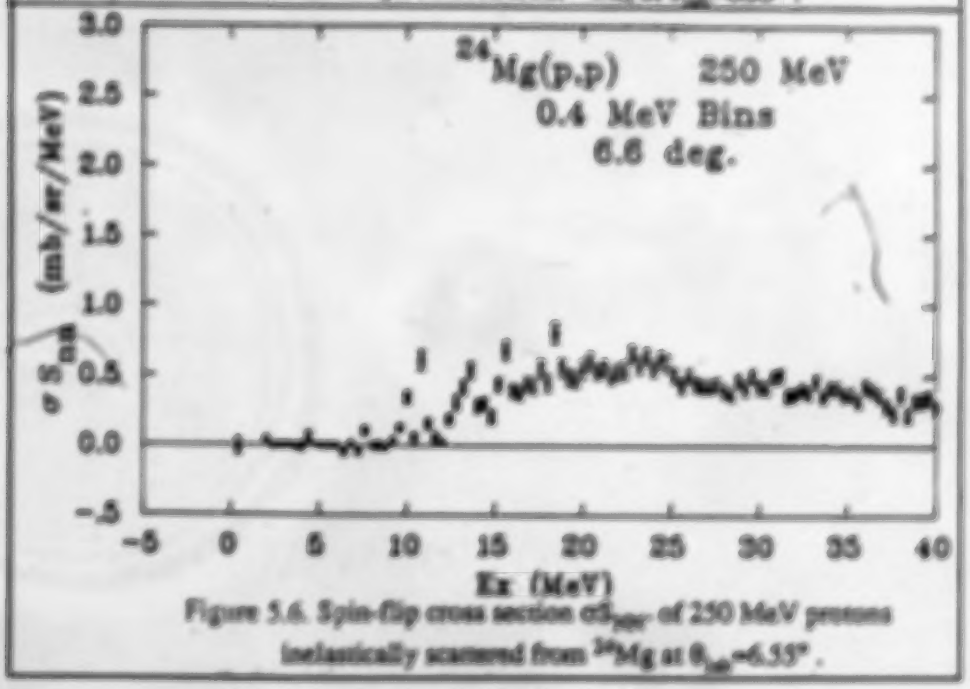

Figure 5.6. Spin-flip cross section σS_{spin} of 250 MeV protons inelastically scattered from ^{24}Mg at θ_{lab}=6.55°.

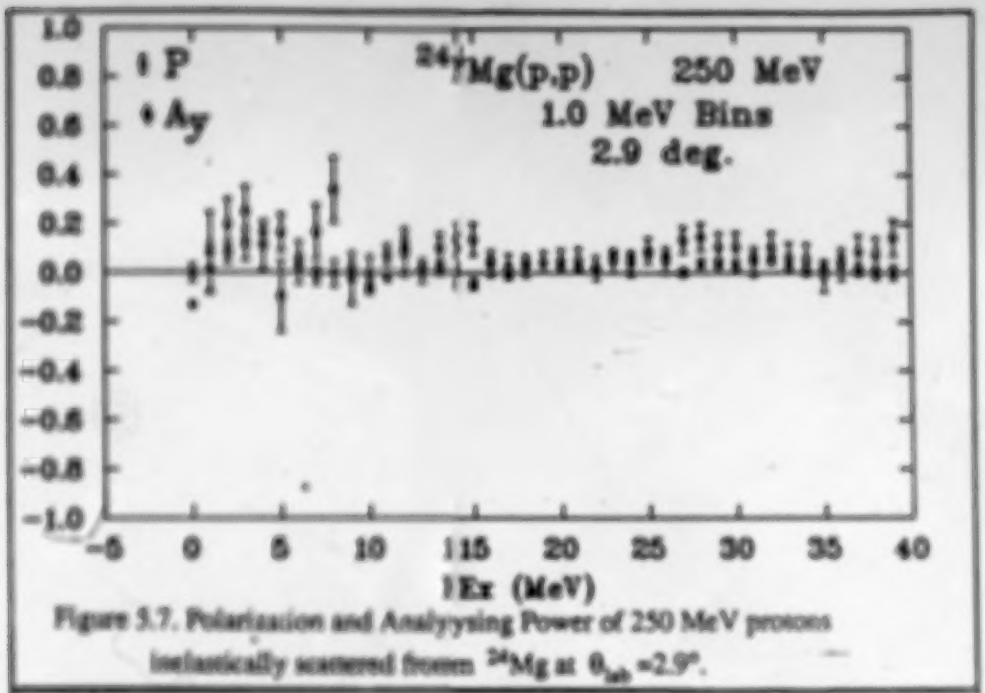

Figure 5.7. Polarization and Analyysing Power of 250 MeV protons inelastically scattered from ^{24}Mg at θ_{lab}=2.9°.

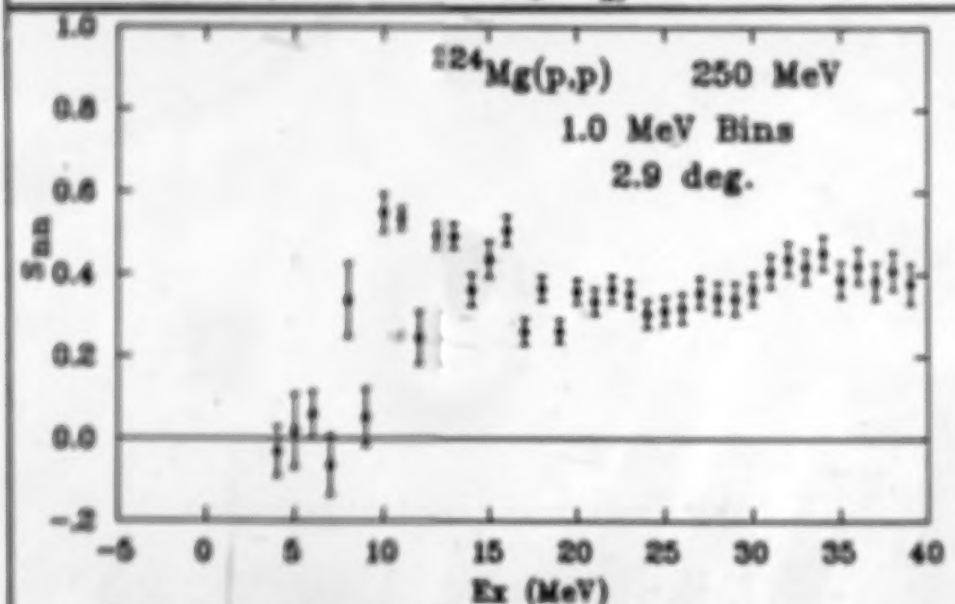

Figure 5.8. Spin-flip probability $S_{NN'}$ of 250 MeV protons inelastically scattered from ^{24}Mg at θ_{lab}=2.9° .

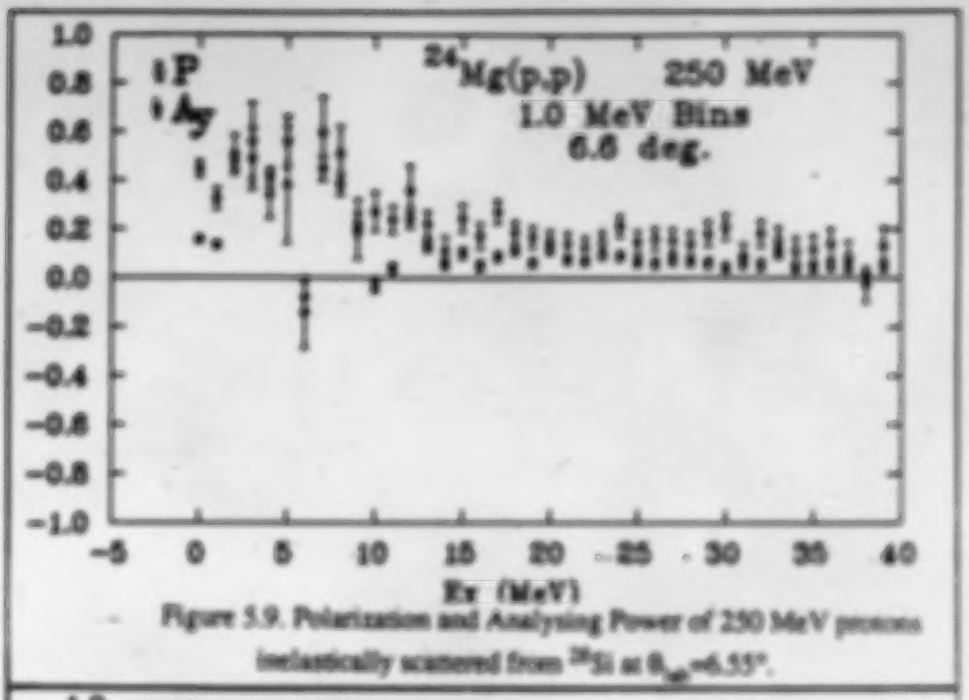

Figure 5.9. Polarization and Analysing Power of 250 MeV protons inelastically scattered from ^{28}Si at θ_{lab}=6.55°.

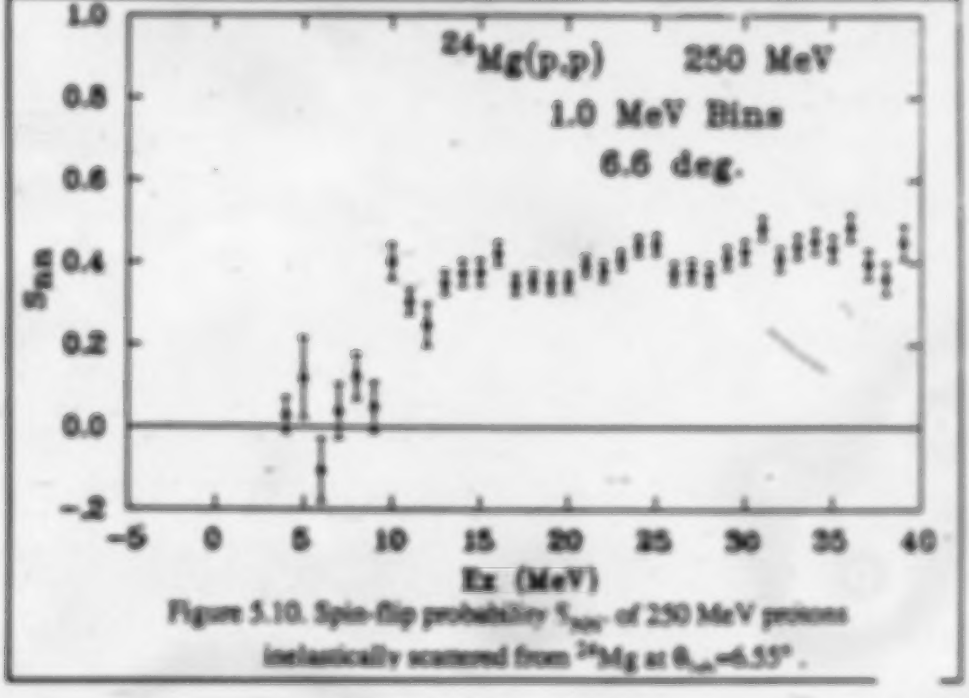

Figure 5.10. Spin-flip probability $S_{NN'}$ of 250 MeV protons inelastically scattered from ^{24}Mg at θ_{lab}=6.55°.

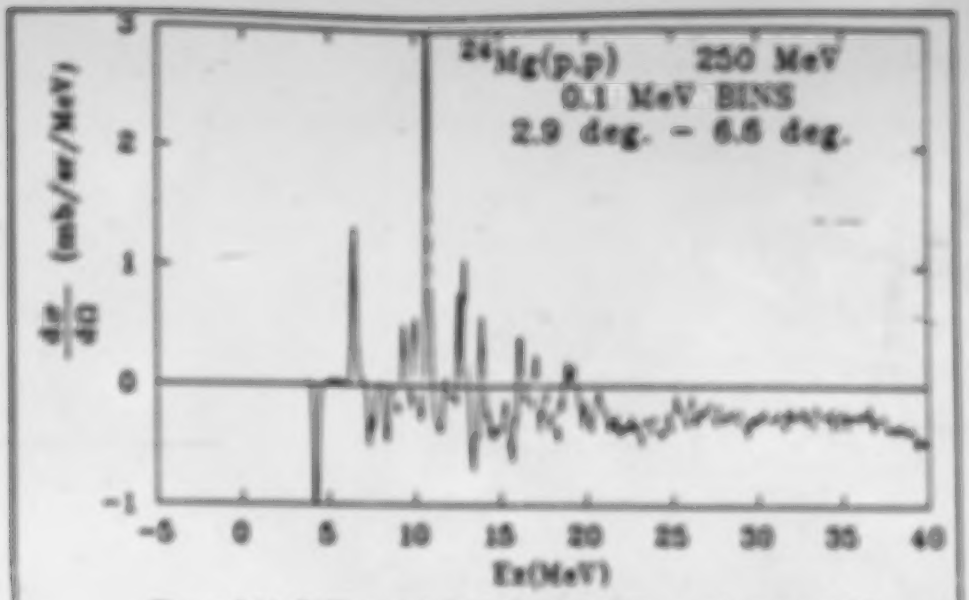

Figure 5.11. Differential Cross-Section difference between 2.9° and 6.55° for the ^{24}Mg(p,p')^{24}Mg reaction.

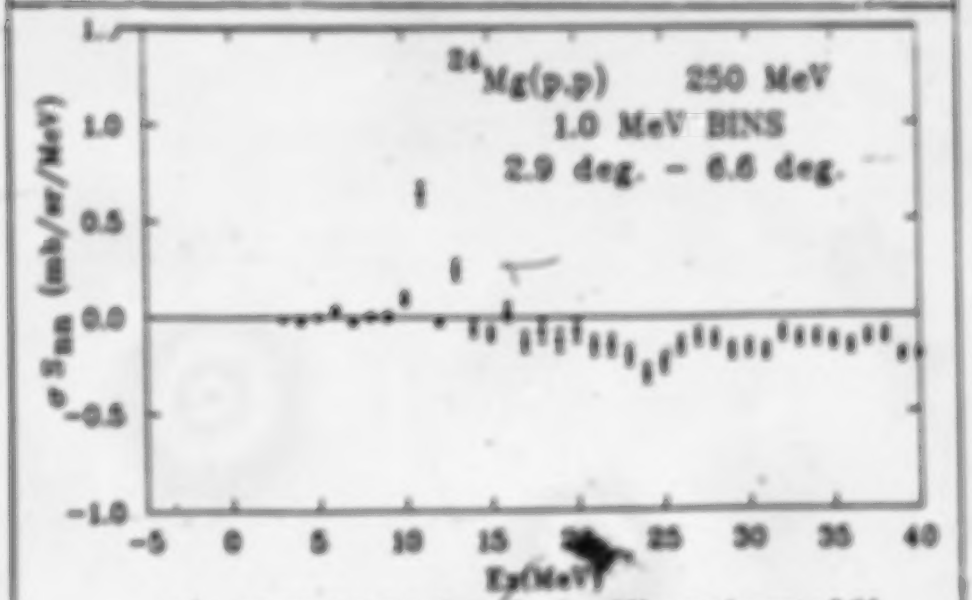

Figure 5.12. Spin Flip Cross-Section difference between 2.9° and 6.55° for the ^{24}Mg(p,p')^{24}Mg reaction.

5.2) $^{28}Si(p,p')^{28}Si^*$ Results

This experiment was carried out at the small-angle MRS facility at TRIUMF using both polarized and unpolarized beams. We have studied inelastic proton scattering from ^{28}Si at five incident energies (200, 250, 290, 360 and 400 MeV) to examine parts of the N-nucleus interaction which contribute to $\Delta S=1$ spin-flip excitation. The ^{28}Si target used was 26.2 mg/cm^2, the natural abundance of the ^{28}Si isotope is 92.23%. The 9.5 MeV state observed in the $^{28}Si(p,p')^{28}Si^*$ spectrum of figure (5.2) is a rare example of a pure (T=0,1$^+$) excitation in nuclei. Its isospin purity can be inferred from the fact that it is not excited in the $^{28}Si(\alpha,\alpha')^{28}Si^*$ reaction (Sc79). Together with the strong (T=1,1$^+$) state at 11.45 MeV it has been used as a probe to study separately the isoscalar and isovector components of the N-nucleus interaction and their energy dependence. Another objective for this experiment is to try to distinguish between the different sources of quenching mechanisms discussed in chapter one.

A study of the same reaction at 200 MeV was carried out at Orsay (An84), and its conclusion was that the Δ-isobar nucleon hole admixture is rather small since it is blocked from contributing to the isoscalar channel, and the two channels are quenched by the same factor, namely 0.34 and 0.29 for the isovector and isoscalar channels, respectively. Based on these results, we decided to carry out the same measurement at TRIUMF with different incident proton energies from 200 to 400 MeV. The 200 MeV measurement was carried out at the MRS in collaboration with C. Djalali, A. Galonsky and G. Crawley from Michigan State University to check the Orsay measurement (An84), while the others were done to study the energy dependence of the 1$^+$ states in the $^{28}Si(p,p')^{28}Si^*$ reaction. Our results show that the Orsay cross sections (An84) were low by about a factor of two at 200 MeV, which would bring the quenching factors up to about 0.6, and then make it comparable with predictions from other probes (see section 5.4).

The measured differential cross sections for both the (T=0,1$^+$) level at 9.5 MeV and the (T=1,1$^+$) level at 11.45 MeV at all measured energies are listed in appendix III. The quoted uncertainty includes only the statistical errors. From frequent inter-comparisons with the reproducibility of individual runs we assess a

systematic uncertainty of 25% to the experimental cross sections. This includes contributions from target nonuniformity and from errors in beam charge integration.

– Before we compare the experimental data with theory, a short description of the spin-flip probability and its properties will be given.

5.3) Spin-Flip Probability Properties

The ability to measure a complete set of observables for (p,p') reactions; equations (2.63) and (2.64); has explored new powerful tools in probing certain aspects of nuclear structure and forces. By measuring all these observables, one would hope to learn something about the reaction model, so it is important to know what observable might shed light on such a problem. One observable, namely $S_{NN'}$ is a special quantity because it is mediated largely by the central spin dependent and tensor components of the effective interaction, and is very weakly influenced by its spin-orbit component. So a study of $S_{NN'}$ may give an insight into these components. $S_{NN'}$ could be described in a nuclear reaction in terms of the transfer of polarization from the incident particle to the nucleus. In other words, it is the probability that an incident particle with spin up (down) relative to the scattering plane leaves with spin down (up) after scattering. Let us recall equation (2.65)

$$S_{NN'} = 0.5\,(1 - D_{NN'})\,,$$

based on the previous equation, an $S_{NN'}=1$ corresponds to $D_{NN'}=-1$, which implies that the scattered particle polarization flips upside down (complete flipping). In order to understand the significance of this observable, consider a simple model, a plane wave impulse approximation (PWIA) with central forces only. For a transition (J^{π}_i) from a 0^+ ground state, the $S_{NN'}$ reduces to a simple form dependent on the angular momentum coupling from the initial to a final state, but independent of the kinematics and dynamics of the reaction such as momentum transfers (Cot81b). This could be demonstrated as follows, for $\Delta s = 1$

$$S(J^{\pi}_j) = (2j+1)/(2\cdot(2J+1)) \qquad j = J \pm 1$$

$$S(J^{\pi}) = (2j+2)/(2(2J+1)) \qquad j = J-1$$

$$S(J^{\pi}) = 1/2 \qquad j = J_{\pm} \qquad 5.1$$

and for $\Delta s = 0$

$$S(J^{\pi}) = 0 \qquad 5.2$$

Thus one finds that $S(J^{\pi})$ is dependent only on the angular momentum transfer of the reaction, and this can be summarized as follows

$$S(J^{\pi}) \geq 0.5 \quad \text{for } s = 1$$

and $$S(J^{\pi}) < 0 \quad \text{for } s = 0. \qquad 5.3$$

Because spin transfer only occure when there is a coupling between spin operators of the interacting nucleons, $S(J^{\pi})$ is large (small) only if spin-dependent forces are present (absent) in a given inelastic transition. As an example, for M1 transition $0^{+} \rightarrow 1^{+}$ ($s=1$, $j=0$), the value of $S_{spp} = 2/3$. The latter remark establishes the credibility of S_{spp} as a signature of spin-flip transitions . Other more realistic models which include the knock on exchange contributions or distortion of the projectile wave functions in both the initial and final channels, support the previous argument especially at small momentum transfers.

5.4) Comparison with Theory

Before we compare the experimental data with theory, a short description of the theoretical calculations performed for this purpose will be given. We have carried out microscopic DWBA calculations based on the Density Dependent Hamburg Interaction (DDI) formalism discussed in section 2.5. In this type of calculation the transition operator is identified with the G-matrix and the required distorted waves are generated with the microscopic optical potential using three-parameter Fermi density and the size of the proton is then unfolded table (5.1). The experimental data (cross

Table 5.1

The three-parameter Fermi density with the size of the proton unfolded has the following geometry

Target	R(fm)	a(fm)	w(fm)
^{208}Pb	3.1970	.5340	-.1950
^{197}Au	3.0062	.6000	-.1748

sections and analysing powers) for elastic scattering and the low lying collective state (2^+) in both ^{26}Mg and ^{28}Si at incident energies between 200 and 400 MeV suggest an empirical reduction of this type of dilatation potential by about 80%, (Li86). The nuclear structure information required about the target nucleus is derived from the elastic scattering for the ground state : density and shell model wave functions for the transition amplitudes. Theoretical calculations depend on the nuclear structure assumptions, so they were performed using two sets of nuclear transition densities namely, Wildenthal and Chung (Wi779), and Brown (Br86), appendix IV. We have found that the two calculations agree : within 10%. The Brown wave functions give a better account of the spectroscopic features like B(M1), B(GT) tables (5.2, 5.3) . The B(M1↑) values predicted by the Brown wave functions for both ^{26}Mg and ^{28}Si, are in good agreement with the electron scattering data (Fe70, Jo74 and Sc79). The Fagg et al (Fe70) and the Johnson and Deakin (Jo74) data give a total B(M1↑) value for the 9.97 and the 10.71 states in ^{26}Mg of 15.67±1.15 μ_N^2 and 4.01±0.35 μ_N^2 , respectively, while the shell model calculations of Brown with free operators predict a total value of 4.3 μ_N^2 and a value of 3.94 μ_N^2 if effective operators fitted to a large body of isovector magnetic moment and M1 transitions : were used (To83 and Ar86).

The B(M1↑) values predicted by the Brown transition densities for ^{28}Si, are in good agreement with the electron scattering data (Fe70 and Sc79). The Schneider et al (Sc79) and the Fagg et al. (Fe70) data : give a total B(M1↑) value for the first five states in ^{28}Si of 5.9±0.24 μ_N^2 and 6.2±1.1.54 μ_N^2 , respectively, (table 5.2),. The shell model calculations of Brown with free operators predict a total value of 6.51 μ_N^2 and a value of 4.8 μ_N^2 if the same effective operators mentioned above were used. We notice that the free operator gives a better account of the experimental data table (5.3), and while the total predicted B(M1↑) value agrees with the experimental values, the distribution of the strength among the different states is overestimated for both ^{26}Mg and ^{28}Si compared to both (e,e') (Sc779) and (p,p') experiments. Since the shell model calculations based on Brown wave functions give a good account of (e,e) experimental data, we will show only this type of calculations.

Angular distributions for the (T=1,1$^+$) level at 10.71 MeV at both 200 and 250 MeV are shown in figure (5.113). The theoretical angular distributions are multiplied by "quenching factors"

$$QF = \sigma_{exp}/\sigma_{theory}$$

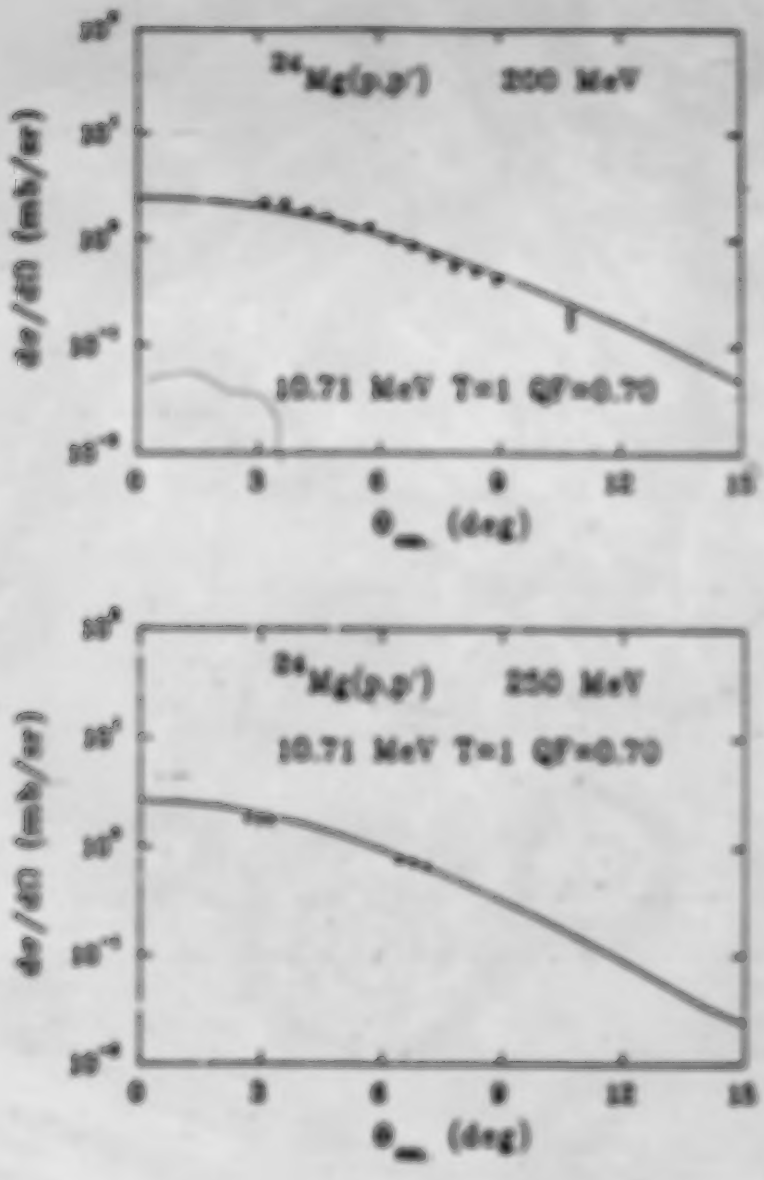

Figure 5.13. Angular distributions for the (T=1,1$^+$) state at Ex=10.71 MeV in the ^{24}Mg(p,p')^{24}Mg* reaction at 200 MeV (up) and at 250 MeV (down). The solid curves are the results of the DWBA calculations discussed in the text.

Table 5.2

B(M1) and B(GT) values for the first five ($1^+,T=1$) states in ^{28}Si according to Brown transition densities.

No.	Ex	B(GT)	$B(M1)_{free}$	$B(M1)_{eff}$
1	10.810	1.058	1.518	0.983
2	11.592	0.108	0.538	0.517
3	11.919	1.164	3.063	2.449
4	12.644	0.959	1.397	0.810
5	12.970	0.000	0.026	0.039

Table 5.3

B(M1) and B(GT) values for the ($1^+,T=1$) states in ^{24}Mg according to Brown transition densities.

No.	Ex	B(GT)	$B(M1)_{free}$	$B(M1)_{eff}$
1	9.991	0.090	1.002	1.321
2	10.635	1.510	3.298	2.618
3	12.733	0.814	0.465	0.164
4	13.142	0.062	0.136	0.068
5	14.053	0.092	0.288	0.242
6	14.453	0.013	0.041	0.070
7	14.627	0.047	0.029	0.015
8	15.075	0.032	0.089	0.053
9	15.410	0.001	0.018	0.018
10	15.687	0.013	0.078	0.116

to obtain agreement with experiment. The strong 1⁺ peak at Ex =10.71 MeV is a pure $\Delta T=1$ isovector excitation whose cross section should be proportional to the Gamow-Teller strength B(GT) for this particular state. The QF for the (T=1, 1⁺) in the $^{26}Mg(p,p')^{26}Mg^*$ reaction at both 200 and 250 MeV is constant, namely (QF=0.7).

Theoretical calculations based on the microscopic DWBA of Petrovy and Love (Pet81) and distorting potentials based on phenomenological optical model potentials fitted to elastic scattering data (σ and A_y) for ^{28}Si (Li86) were also performed. The QF for the (T=1, 1⁺) in the $^{26}Mg(p,p')^{26}Mg^*$ reaction at both 200 and 250 MeV is constant, namely QF=0.82 or 0.90 depending on whether Brown transition densities or Chung and Wildenthal's were used. The quenching factors obtained from this type of calculation are listed in table (5.4).

The spin-flip cross section $d\sigma/d\omega_{spf}$ is a direct measure of $\Delta S=1$ spin transfer to ^{26}Mg. At small angles (2.9°) and small excitation energies (E_x < 16 MeV) most of the strength arises from the 1⁺, $\Delta T=1$ Gamow-Teller excitations with small contribution from isoscalar (1^+, $\Delta T=0$) and higher multipole ($\Delta L_z > 0$) excitations. We show here that Gamow-Teller strength extracted from $d\sigma/d\omega_{spf}$ in (p,p') agrees with existing data on (p,n) and (n,p) charge exchange reactions in this mass region.

According to equations (3.1 and 3.2), higher multipoles should contribute to the expected values of S_{spf}. The experimental data supports this argument, the angular distribution of $d\sigma/d\omega_{spf}$ is almost flat beyond 20 MeV between 2.9° and 6.6°, whereas a pure M1 distribution would decrease by a factor of about three over this range. Thus a determination of the M1 contribution in this excitation energy range will require a multipole decomposition of the $d\sigma/d\omega_{spf}$ spectra. A microscopic RPA calculation for $d\sigma/d\omega_{spf}$ in ^{90}Zr (Ost87, Yak86), shows large $\Delta L_z > 0$ (i.e. L=1 and L=2) contributions in the continuum. E1 states are excited by coulomb excitation. The angular distribution of the cross section for the E1 states is very similar to that for the M1 states, it is the spin-flip probability which distinguishes between them. To perform this analysis properly, the angular range of the data must be broadened considerably. Such calculations are not available for the $^{26}Mg(p,p')^{26}Mg^*$ data, but according to the DD calculations (Dyk86) which were discussed earlier in this chapter, the experiment can account for about 60% of the predicted strength. We have found that the M1 strength from the $d\sigma/d\omega_{spf}$ spectrum at 2.9°, is concentrated in the 9-16 MeV region and it can account for about 2.50 mb/sr. From differences in the spectra at 2.9° and 6.6° (figures 5.11 and 5.12) we estimate an L=0 fraction of 0.83 thus $(d\sigma/d\omega_{spf}, 1^+)_{corr}$=2.13

Table 5.4

Quenching of Gamow-Teller and M1 strength in ^{24}Mg:

E_x	Measured quantity	(p,p') QF(WB)	(p,p') QF(WC)	(e,e') QF(WB)	(e,e') QF(WC)
9-15	σS_{NN}	0.78 (0.66)*	0.84 (0.70)*		
10.71	σ	0.82 (0.70)*	0.90 (0.80)*		
10.71	B(M1)			1.18	1.13

( )* QF based on the DD approach.

Table 5.5

Quenching factors for the strongest isovecor (1^+,T=1) and isoscalar (1^+,T=0) states in 28Si according to two different calculations, the first is based on Franey and Love interaction and Wildenthal and Chung Transition densities (FL,WC), while the second is based on the Density Dependent Hamburg interaction and Wildenthal and Brown transition densities (DD,WB):

E_p	(FL,WC) QF(T=0)	(FL,WC) QF(T=1)	(DD,WB) QF(T=0)	(DD,WB) QF(T=1)
200	0.46±0.035	0.74±0.05	0.40±0.050	0.72±0.05
250	0.70±0.042	0.84±0.05	0.60±0.050	0.70±0.05
290	0.60±0.060	0.70±0.06	0.50±0.060	0.70±0.06
360	0.69±0.070	0.77±0.06	0.60±0.070	0.70±0.06
400	0.72±0.044	0.84±0.05	0.60±0.070	0.70±0.05

mb/sr. The quenching factors for the combined isovector and isoscalar 1^+ states $QF(\sigma S_{NN}, 1^+)$, (table 5.4), in the 9-16 MeV region are in good agreement with those for the 10.71 MeV (1^+,T=1) state.

In table (5.4) , the quenching factors for the hadronic reaction QF(p,p') are compared to those for the electromagnetic reactions QF(e,e'). The latter are calculated with effective g factors which contain effects of meson-exchange currents and higher-order configuration mixing, i.e. QF(e,e') =1 would be expected for ideal transition densities. The fact that QF(p,p')/QF(e,e') < 1.0 implies that the effective axial vector coupling constant $g_A^{eff} < g_A^{free}$ in ^{24}Mg.

Another model which has proved its success in explaining the spin-flip data is the semi infinite slab model (Sh83, Sm86). This model examines the surface response function of nuclei to spin-dependent probes. In this model the nucleus is approximated by a semi-infinite slab of interacting fermions. The two dimensional geometry makes the calculations possible, the features of the response due to nuclear structure effects are not predicted, ground state correlations are included via the RPA. Giant resonances do not appear in the predicted cross sections since these do depend on the specific orbits of the nucleons. Nucleon-nucleon scattering amplitudes are taken directly from the analysis of free NN scattering, and the reaction is treated in terms of an approximation to Glauber theory. One of the advantages of this model is that it avoids the problem of multipole decomposition, but it is a rough model since it has no real structure input. But the calculations for ^{90}Zr (Sh83) and ^{54}Fe (Sm86) suggest that there is little or no quenching of the integrated spin strength in this region.

Angular distributions for the dominant isovector and isoscalar 1^+ states at (200, 250, 290, 360 and 400 MeV) are shown in figures (5.14, 5.15, 5.16, 5.17 and 5.18). The theoretical angular distributions are multiplied by quenching factors "QF" to obtain agreement with experiment. The peak at 9.5 MeV in figure (5.2) is an unresolved doublet, consisting of a known (T=0, 2^+) level at 9.48 MeV and a (T=0,1^+) level at 9.5 MeV, (An84). Since the resolution achieved is not adequate to resolve these two levels, we have used an experimental 2^+ shape (Li86) to add to the calculated IPM angular distribution to compare with the measured cross sections. The extracted quenching factors based on the DD approach are listed in table (5.5) versus incident proton energy. The quenching factor for the (T=0,1^+) level at 200 MeV is significantly smaller than those at 250 MeV and above. Excluding the 200 MeV data an average value of QF = 0.57±0.05 for this level is obtained. The results for the (T=1,1^+) level at 11.45 MeV are consistent with an average value QF = 0.70±0.05 for

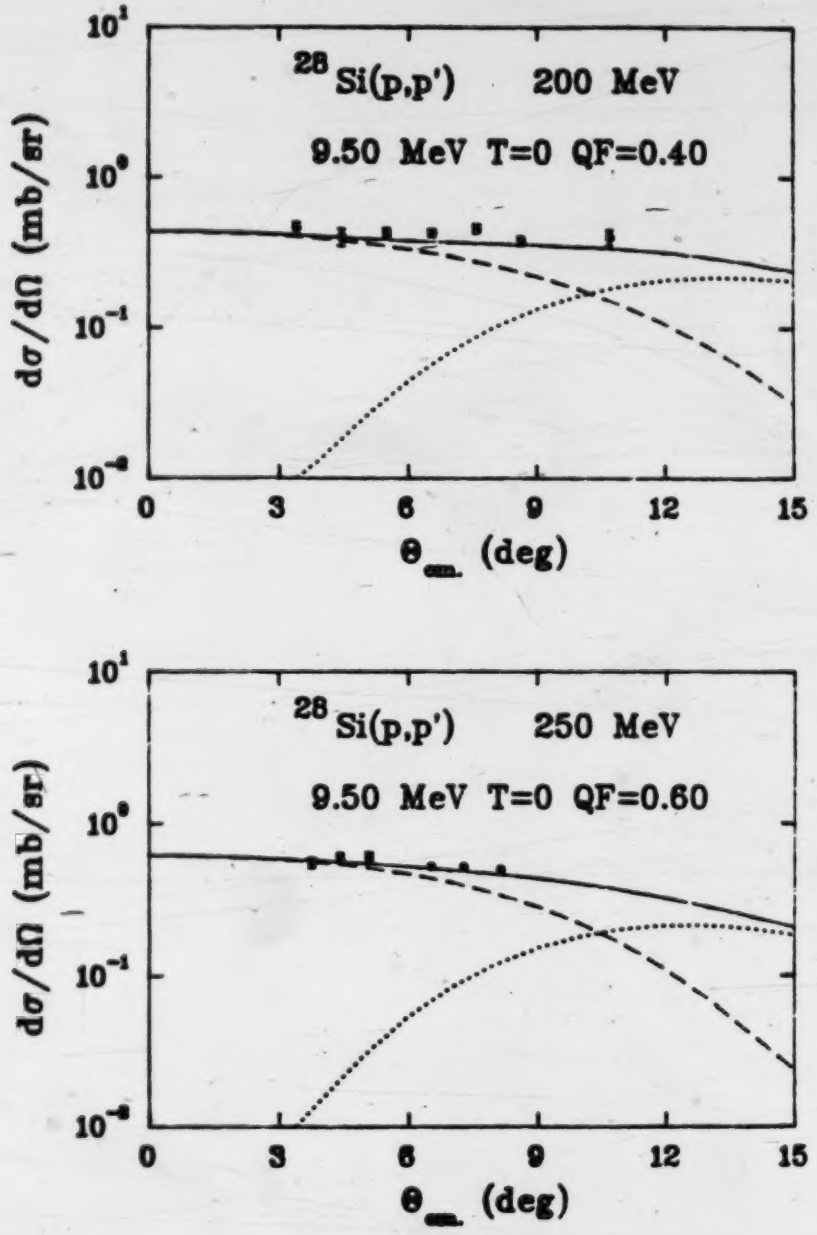

Figure 5.14. Angular distributions for the (T=0,1$^+$) state at Ex=9.5 MeV in the ^{28}Si(p,p$'$)^{28}Si* reaction at 200 MeV (up) and at 250 MeV (down). The dashed curves are the results of the DWBA calculations discussed in the text. The dotted curves represent the experimental shape for a 2$^+$ state and the solid line is the sum of the dashed and the dotted curves.

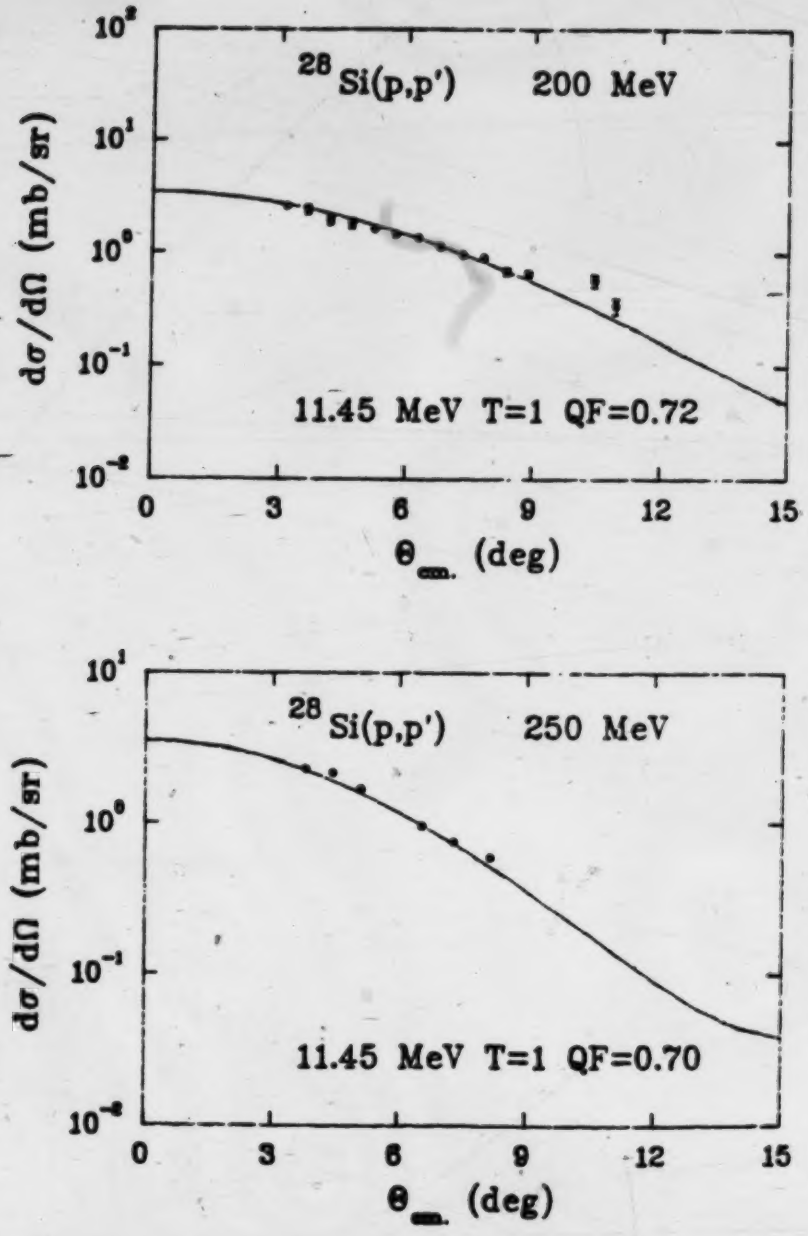

Figure 5.15. Angular distributions for the (T=1,1$^+$) state at Ex=11.45 MeV in the ^{28}Si(p,p')^{28}Si* reaction at 200 MeV (up) and at 250 MeV (down). The solid curves are the results of the DWBA calculations discussed in the text.

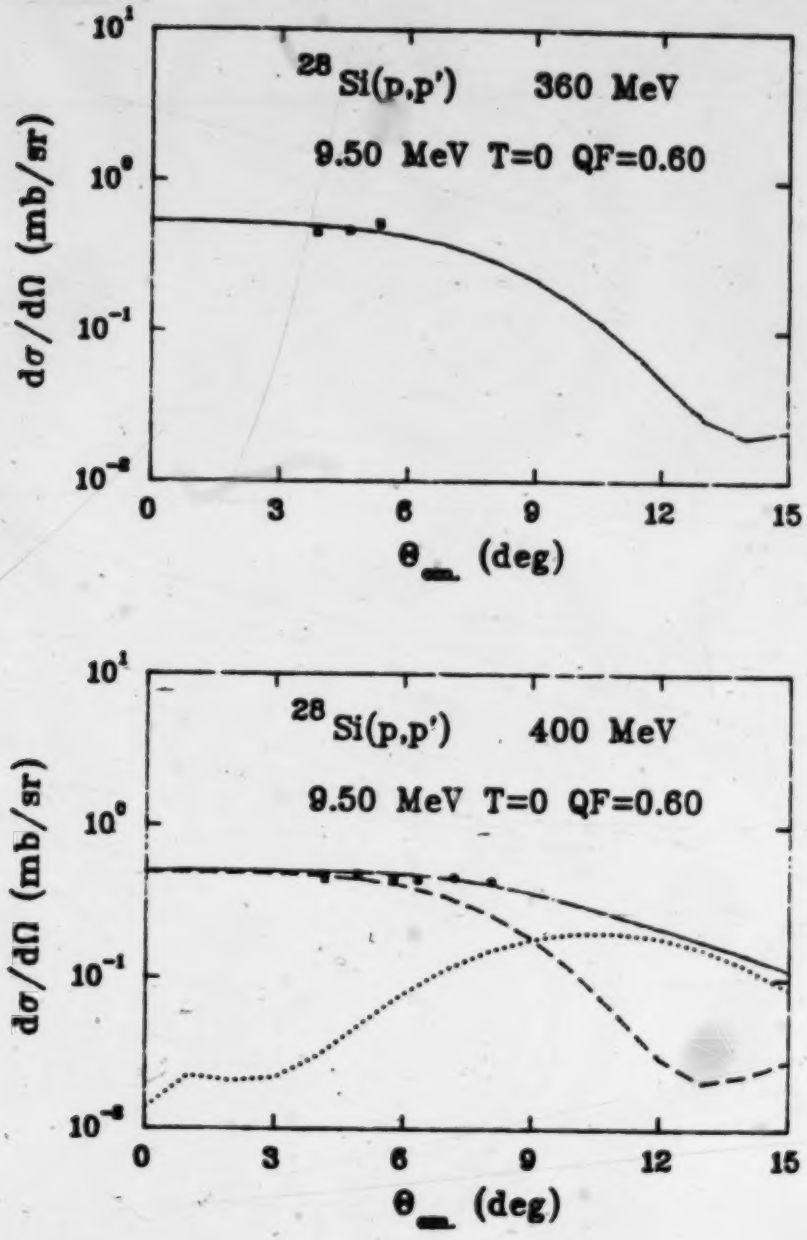

Figure 5.16. Angular distributions for the ($T=0,1^+$) state at Ex=9.5 MeV in the $^{28}Si(p,p')^{28}Si^*$ reaction at 360 MeV (up) and at 400 MeV (down). The dashed curves are the results of the DWBA calculations discussed in the text. The dotted curves represent the experimental shape for a 2^+ state and the solid line is the sum of the dashed and the dotted curves.

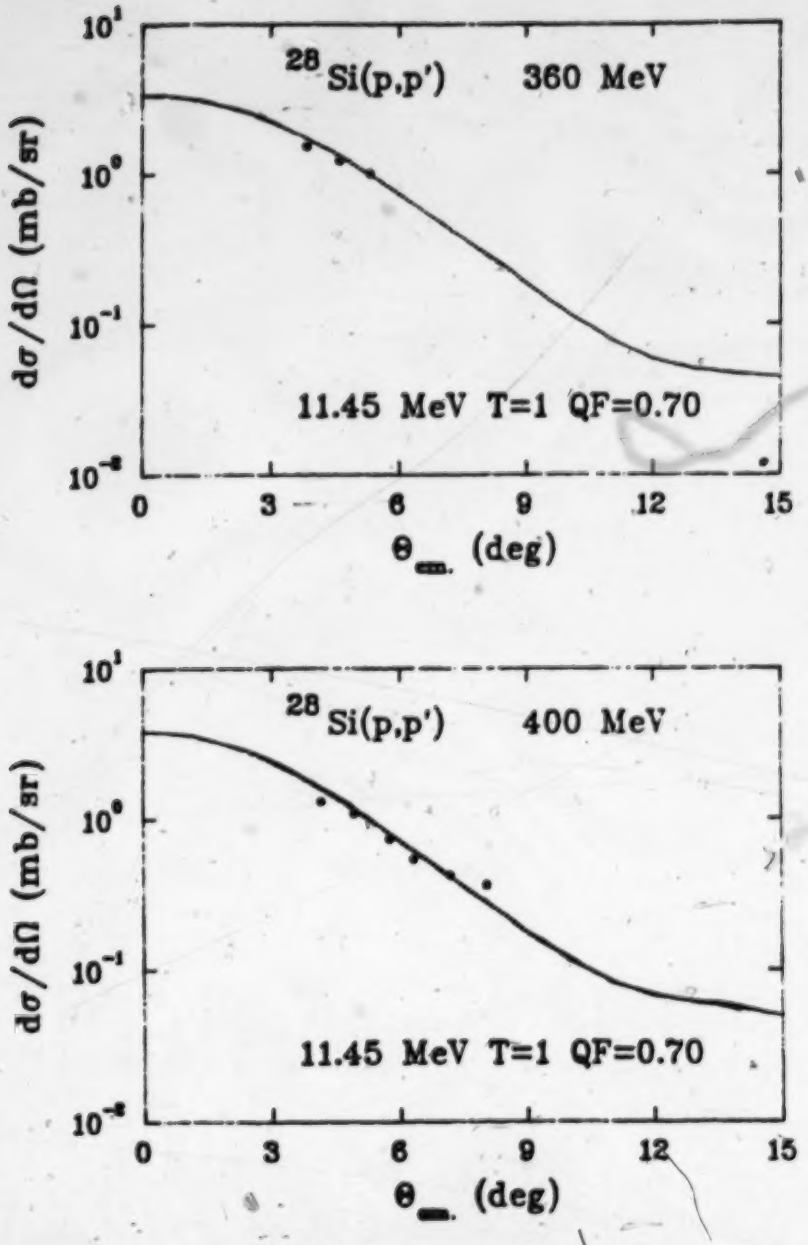

Figure 5.17. Angular distributions for the (T=1,1$^+$) state at Ex=11.45 MeV in the ^{28}Si(p,p')^{28}Si* reaction at 360 MeV (up) and at 400 MeV (down). The solid curves are the results of the DWBA calculations discussed in the text.

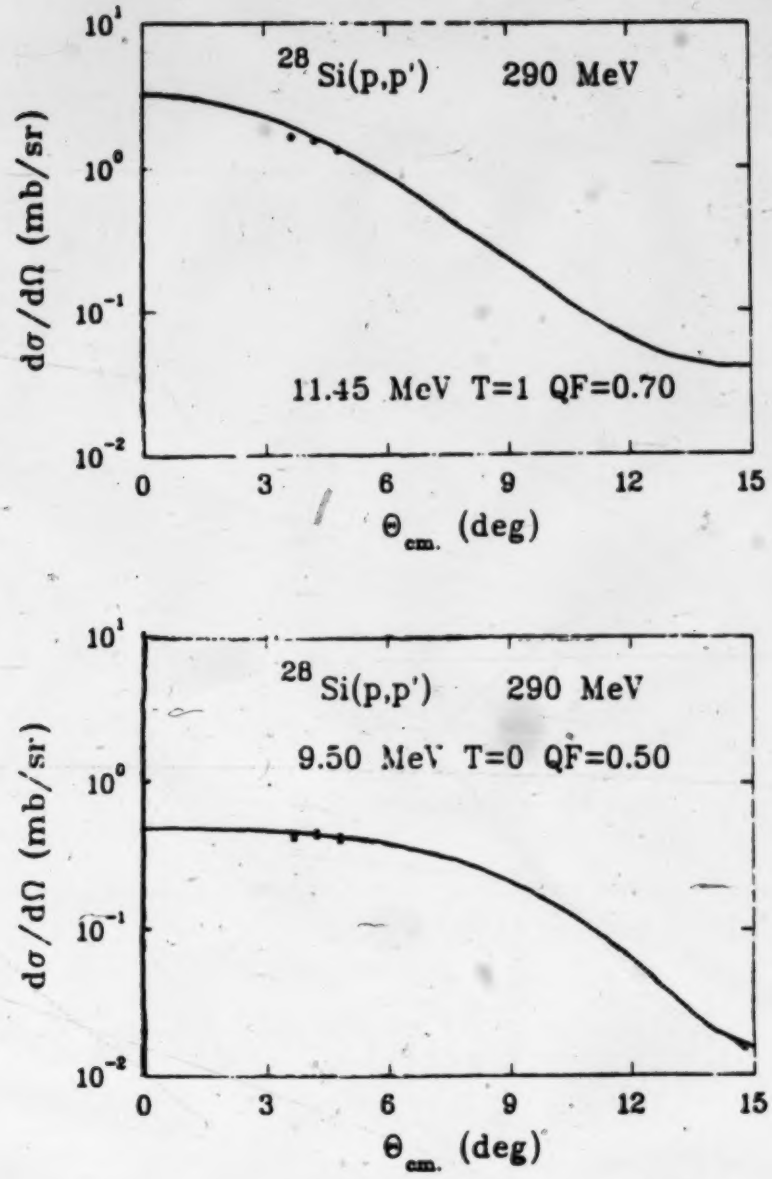

Figure 5.18. Angular distributions for the (T=1,1$^+$) state at Ex=11.45 MeV in the ^{28}Si(p,p$'$)^{28}Si* reaction at 290 MeV (up) and for the (T=0,1$^+$) state at Ex=9.50MeV at 290 MeV (down). The solid curves are the results of the DWBA calculations discussed in the text.

all measured energies, this is shown in figure (5.19).

Theoretical calculations based on the microscopic DWIA of Franey and Love (Fr85) and distorting potentials based on phenomenological optical model potentials fitted to elastic scattering data (σ and A_y) for ^{28}Si (Li86) were also performed. In this type of calculation, the transition densities of Chung and Wildenthal (Wi79) were used. Excluding the 200 MeV data, an average value of QF = 0.69±0.05 is obtained for the ($T=0,1^+$) level at 9.5 MeV, and an average value of QF = 0.78±0.05 for the ($T=1,1^+$) level at 11.45 MeV is also obtained for the other measured energies. The quenching factors obtained from this type of calculations are listed in table (5.5), and shown in figure (5.20) .

The quenching factor (QF) is a nuclear structure property, and should be energy independent. The results of ^{28}Si(p,p´)^{28}Si* reaction support this argument, the QF for both the 1^+ isoscalar and the isovector transitions are comparable at all measured energies. This supports the Orsay conclusion (An84) that the Δ-isobar quenching mechanism cannot be the main source for GT quenching, since the isoscalar and isovector channels are quenched by comparable factors and this mechanism is blocked from contributing to the isoscalar channel being an isovector by nature. The QF for the (1^+, ΔT=1) in the ^{24}Mg(p,p´)^{24}Mg* reaction at both 200 and 250 MeV is constant. It is the same (QF=0.7) as for the strongest (1^+, ΔT=1) state in the ^{28}Si(p,p´)^{28}Si* reaction. This means that the quenching factors for 1^+ states in the same shell are the same or comparable.

It is now well established (Go84, Ma86) that in the (p,n) reaction on heavier targets (A >16) only 50-60% of the GT strength calculated in the shell model with free-nucleon operators is actually observed in the low-energy region. Recent (n,p) experiments at TRIUMF (Al87, Ve86) account for about 60% or more of the total GT strength in the ^{24}Mg(n,p) and ^{54}Fe(n,p) reactions, which implies a universal quenching for the three probes, this is demonstrated in figure (5.21).

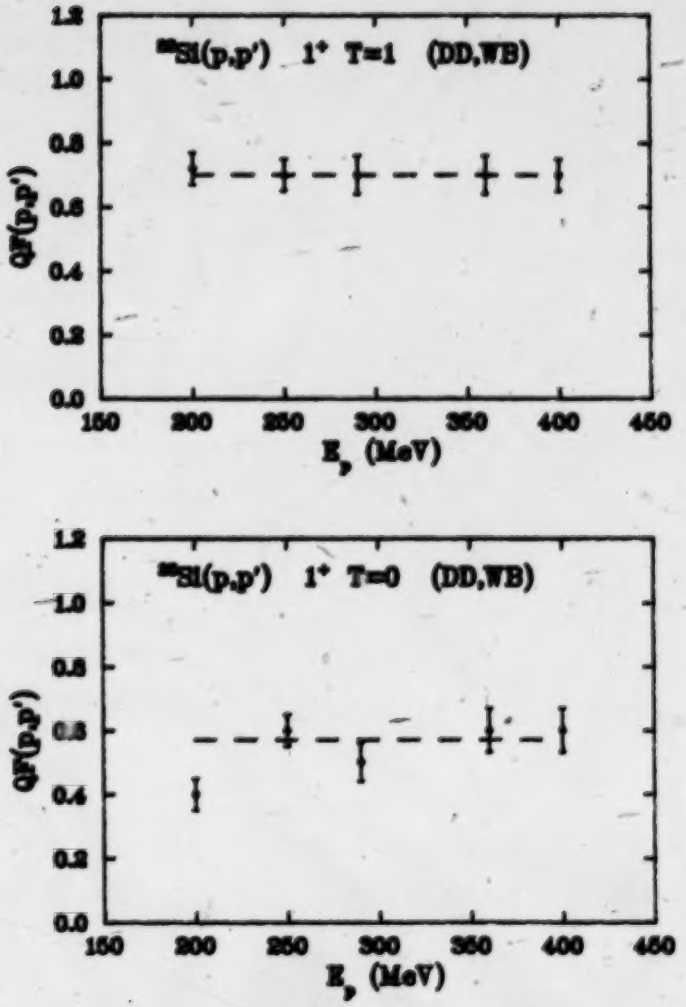

Figure 5.19. Quenching factors for the strongest isovector (up) and isoscalar (down) states in ^{28}Si between 200 MeV and 400 MeV using the density dependent interaction and Brown and Wildenthal transition densities.

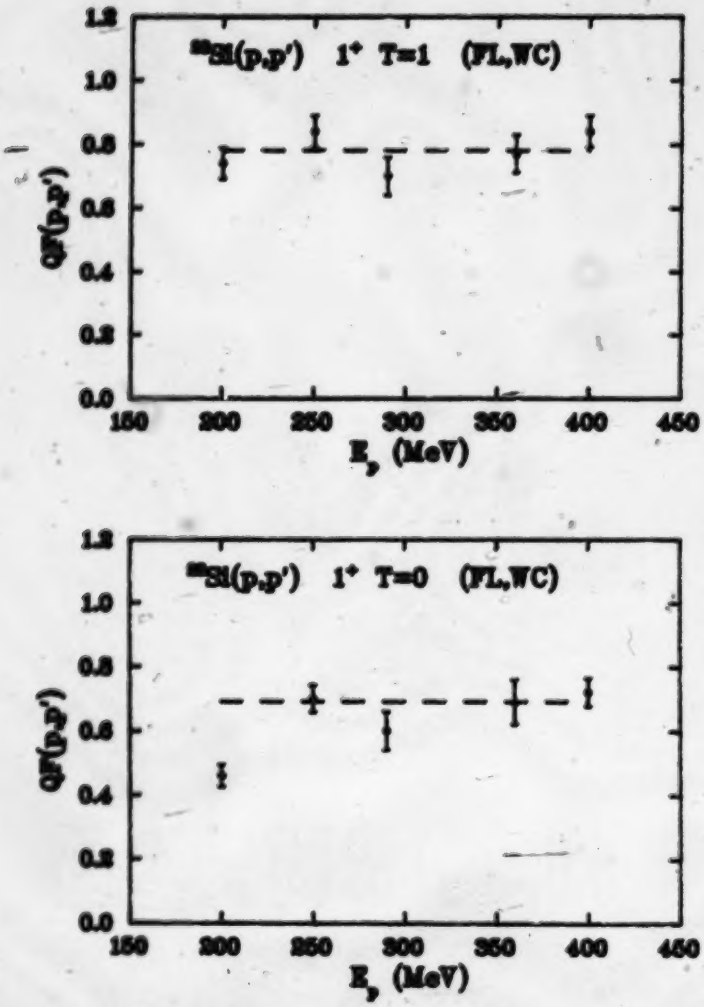

Figure 5.20. Quenching factors for the strongest isovector (up) and isoscalar (down) states in ^{28}Si between 200 MeV and 400 MeV using the Franey and Love interaction and Wildenthal and Chung transition densities.

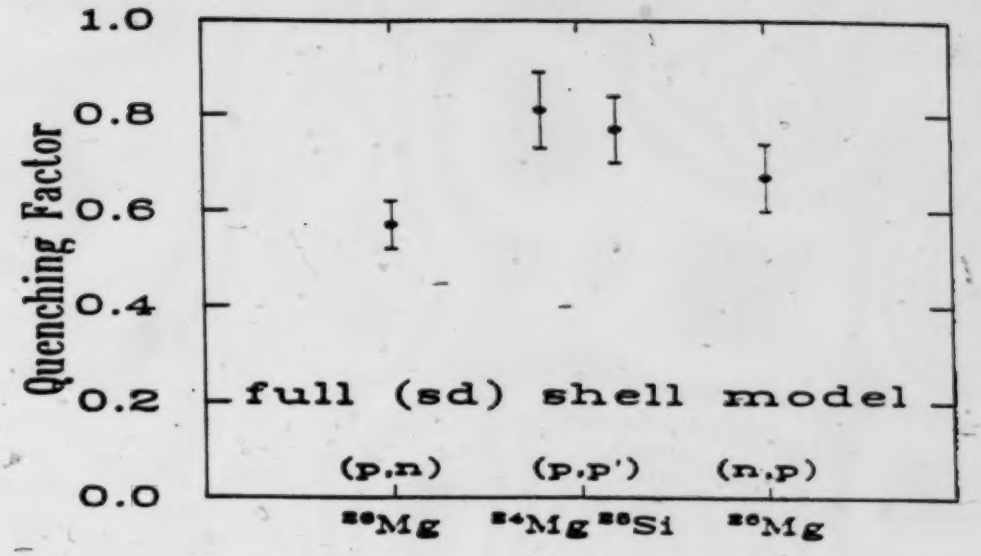

Figure 5.21. Summary of GT quenching in s-d shell nuclei.

6. Conclusion

This work was carried out with many objectives in mind. First, we have investigated the suitability of the nucleon-nucleus interaction for deducing nuclear structure information; secondly, the study of spin-isospin excitations, which are strongly excited at forward angles, to investigate the properties of the effective interaction at small momentum transfer. The third objective is concerned with the missing Gamow-Teller (GT) strength.

Various mechanisms have been proposed to explain the missing strength in the low-lying spectrum, including Δ-hole admixtures and configuration mixing within and across major shells. Probably both mechanisms contribute, but the quantative degree of each piece is still not known reliably.

Based on the DD calculations, the quenching factor for the isoscalar (1^+,Ex=9.5 MeV) and isovector (1^+, Ex=11.45 MeV) states in the $^{28}Si(p,p')^{28}Si^*$ reaction is 0.58 and 0.7, respectively. The fact that both the isovector and isoscalar channels are quenched by a comparable factor, suggests that the Δ-hole admixtures approach is not the most likely explanantion for the missing strength. This is because the Δ-hole coupling is an isovector by nature, it is blocked from contributing to the isoscalar channel. Also, the spin-flip data obtained from the $^{24}Mg(p,p')^{24}Mg^*$ reaction shows that most of the M1 strength is concentrated in the 9-16 MeV region. So based on these data, one may conclude that configuration mixing is the most likely or dominant of the two processes.

The spin-flip cross section σS_{NN} is the absolute measurement of spin-excitation strength and also effectively eliminates instrumental background which should have zero spin flip probability. Based on the σS_{NN} data for the $^{24}Mg(p,p')^{24}Mg^*$ and DD calculations (Dy86) based on the shel. nodel, the experiment can account for about 66% of the predicted strength. Theoretical calculations depend on the nuclear structure assumptions, so the calculations were performed using two sets of nuclear wave functions namely, Wildenthal and Chung (Wi79), and Brown and Wildenthal (Br86). We have found that the two calculations agree within 10%.

The quenching factor (QF) is a nuclear structure property, and should be energy independent. The data obtained in this work supports this argument since the QF for both the strongest 1^+ isoscalar and the isovector transitions in the $^{28}Si(p,p')^{28}Si^*$ reaction is comparable at all measured energies. The QF for the strongest (1^+, $\Delta T=1$) in both the $^{24}Mg(p,p')^{24}Mg^*$ and the $^{28}Si(p,p')^{28}Si^*$ reaction reactions at all the measured energies is constant (QF=0.7). This means that the quenching factors for 1^+ states in the same shell are the same or comparable.

It is now well established that there is a universal quenching for the three probes; (p,p'), (p,n) and (n,p); (Al86, Al87, Ha86c, Go84, Ma86 and present work). The experimental data available from the three probes can account for about 60% of the IPM strength.

Finally, one can draw the following conclusions. First, the nucleon-nucleus interaction at intermediate energies provides a comprehensive, quantitative description of spin-isospin excitation in nuclei. Second, in the (p,p') experiments at small momentum transfer, the spin-flip cross sections and small instrumental background are essential for reliable determination of GT strength at low excitation energies. Third, the quenching of GT strength remains an outstanding problem, but the Δ isobar quenching mechanism is likely to be small. And fourth, there is a universal quenching factor for (p,n), (n,p), and (p,p') reactions.

Refrences

Al86 W.P. Alford, R.L. Helmer, R. Abegg, A. Celler, O. Hausser, K. Hicks, K.P. Jackson, C.A. Miller, S. Yen, R.E. Azuma, D. Frekers, R.S. Henderson, H. Baer, C.S. Zafiratos, Phys. Lett. B179, 20 (1986).

Al87 W.P. Alford et al , Physics Letters, in the press, (1987).

An84 N. Anataraman, B.A. Brown, G.M. Crawley, A. Galonsky, C. Djalali, N. Marty, M. Morlet, A.Willis, J.C. Jourdian, and B.H. Wildenthal, Phys. Rev. Lett. 52, 1409, (1984).

Ar79 A. Arima and H. Hyuga, Mesons in nuclei, edited by D. Wilkinson, p. 683 (1979).

Ar84 R.A. Arndt and D. Roper, Virginia Polytechnic Institute Scattering Analysis Interactive Dial-in program (SAID), solution SP84, (1984).

At81 L. G. Atencio, J. A. Amann, R. L. Boudrie and C. L. Morris, Nuc. Inst. Meth. 187, 381 (1981).

Be81 G.F. Bertsch, Nuc. Phys. A354, 157c, (1981)

Be82a G.F. Bertsch, O. Sholten , Phys. Rev. C25, 804(1982).

Be82b G.F. Bertsch and I. Hamamoto, Phys. Rev. C26, 1323 (1982).

Br83a B.A. Brown and B.H. Wildenthal Phys. Rev. C27, 1296(1983).

Br83b B.A. Brown and B.H. Wildenthal Phys. Rev. C28, 2397(1983).

Br86 B.A. Brown, MSUNSC internal report No.572, (1986).

Co81a W.D. Cornelius, J.M. Moss, and T. Yamaya, Phys. Rev. C23, 1364 (1981).

Co81b E.D. Cooper, Ph.D. thesis, university of Alberta, unpublished, (1981).

Dj83 C.D. Djalali, N. Marty, M. morlet, A. willis, J.C. Jourdian, N.A. Anantarman, G. M. Crawley, A. Galonsky and J. Duffy. Nuclear Phys. A410, 399 (1983).

Dj84 C. Djalali, Ph.D. thesis, university of Paris, unpublished, (1984).

Do71 B.L. Donnally, Proc. 3rd International Symposium on Polarization phenomena in nuclear reactions, ed. H.H Barschall and W. Haeberli, 295 (1971).

Dw83 J. R. Comfort, modified version by of the computer program DWBA70 by R. Shaeffer and J. Raynal, (1983).

Dy86 R. Dymarz, theoretical calculations based on reference Dw83, private communication, (1986).

Er73 M. Ericson, A. Figureau and C. Thevenet, Phys. Lett. 42, 51 (1973).

Fa70 L.W. Fagg, W.L. Bendel, S.K. Numrich and B.T. Chertok. Phys. Rev. C1, 1137 (1970).

Fa75 L. W. Fagg, Rev. Mod. Phys. 47, 683 (1975).

Fr83 D. Frekers, LISA documentation manual, unpublished, (1983).

Fr85 M.A. Franey and W.G. Love Phys. Rev. C31, 488 (1985).

Go84 C. Goodman, Spin Excitations in Nuclei, Plenum, New York, 143 (1984).

Gr84 P.W. Green, DACS handbook, unpublished, (1984).

Ha 86a O. Hausser, K. Hicks, C.W. Glover, R. Abegg, W.P. Alford, A. Celler, C. Gunther, R.L. Helmer, R. Henderson, D.J. Horen, C.J. Horowitz, K.P. Jackson, J. Lisantti, D.K. Mcdaniels, C.A. Miller, R. Sawafta, L.W. Swenson. Phys. Lett. B184, 316, (1987).

Ha 86b O. Hausser, R. Henderson, K. Hicks, D.A. Hutcheon, D. Clark, C. Gunther, R. Sawafta, and G. Waters.Nuc. Inst. and Methods, A254, 61, (1987).

Ha 86c O. Hausser, Int. Sym. on Weak and Electromagnetic Interactions in Nuclei, edited by H.V. Klapdor (Springer: Heidelberg), p270.

He 86 R. Henderson, O. Hausser, K. Hicks, C. Gunther, W. Faszer, R. Sawafta, and N. Pope. Nuc. Inst. and Methods , A254, 67, (1987).

Hi84 K. Hicks and C.A. Miller, FFIT routine, unpublished, (1984).

Hi86 K. Hicks, MRS manual, unpublished, (1986).

Hu72 J. Hufner and C. Mahaux, Ann. of Phys. 73 , 525 (1972).

Ik64 K. Ikeda, Prog. Theor. Phys., 31, 434 (1964).

Je76 J.P. Jeukenne, A. Lejeune and C. Mahaux, Phys. Rev. C25, 83, (1976).

Jo74 A. Johnston and T.E. Drake, J. Phys. A7, 898 (1979).

Kl85 A. Klein, W.G. Love and N. Auerbach, Phys. Rev. C31, 710 (1985).

La80 M. Lacombe, B. Loiseau, J.M. Richard, R. Vinh Mau, J. Cote, P. Pires and R. de Tourreil, Phys. Rev. C21, 861 (1980).

Li86 K. Lin, M.Sc. thesis, Simon Fraser University, unpublished (1986).

Lo81 W.G. Love and M.A. Franey, Phys. Rev. C24, 1073 (1981).

Lo83 W.G. Love and M.A. Franey, Phys. Rev. C27, 438 (1983).

Ma86 R.D. Madey et al., Int. Sym. on Weak and Electromagnetic Interactions in Nuclei, edited by H.V. Klapdor (Springer: Heidelberg), p280.

Mc84 J. B. McClelland, J. F. Amann, W. D. Cornelius, H. A. Thiessen, and B. Aas, Los Alamos Report No. LA-UR-84-1671. (1984).

Mi86 R. Mitchell, M.Sc. thesis, university of Alberta, unpublished (1986).

Mo58 G. Morpurgo, Phys. Rev 110, 721 (1958).

Na85 S.K. Nanda, Ph.D. Thesis, Rutgers University (1985) unpublished.

Os85 F. Osterfeld, D. Cha and J. Speth, Phys. Rev. C31, 372 (1985).

Os79 E. Oset and M. Rho, Phys Rev. Lett. 42, 47 (1979).

Ri84 L. Rikus and H. von Geramb, Nuc. Phys. A426, 496 (1984).

Sa84 R. Sawafta, M.Sc. Thesis, University. of Alberta (1984) unpublished.

Sc79 R. Schneider, A. Richter, A. Schwierczinski, E. Spamer and O. Titze, Nucl. Phys. A323, 13 (1979).

Sh74 K. Shimizu, M. Ichimura and A. Arima, Nucl. Phys. A226, 282 (1974).

Sh83 O. Sholten, G. F. Bertsch, and H. Toki, Phys. Rev. C27, 2975 (1983).

Sh85 H.S. Sherif, E.D. cooper and R.I. Sawafta, Phys. Lett. 158b, 193 (1985).

Sh86 H.S. Sherif, R.I. Sawafta and E.D. Cooper. Nucl. Phys. A449, 709 (1986).

Sm86 R. Smith, Private communication.

To79 I.S. Towner and F.C. Khanna, Phys. Rev. Lett. 42, 51 (1979).

Ve86 M. Vetterli, private communication, (1986).

Wi79 B.H. Wildenthal and W. Chung, The (p,n) Reaction and the Nucleon-Nucleon Force, edited by C. Goodman et al, 89 (1979).

Wo54 L. Wolfenstein, Phys. Rev. 96, 1654 (1954).

Ya86 M. Yabe, F. Osterfeld, D. Cha, Phys. Lett. B178, 5 (1986)

Yo72 S. Yoshida and L. Zamick, Ann. Rev. Nuc. Sci. 22, 121 (1972)

Appendix I

Optical Model Potential

According to the optical model, the nucleon-nucleus interaction is represented by a complex potential. One can parametrize the non relativistic optical potential based on the Schrodinger equation as follows

$$U_{op} = V_{coul} + V_c F_c + i (W_{cv} - 4 W_{cs} \partial/\partial r) F_{ic}$$

$$+ (h/m_\pi c)^2 [V_{so} 1/r \partial/\partial r F_{so} + iW_{so} 1/r \partial/\partial r F_{iso}] \sigma.L \qquad \text{AI.1}$$

where V and W denote the real and imaginary potential depths, respectively, while F_x is a radial function giving a shape to the associated potential. The subscripts 'c', 'cv', 'cs', 'i', and 'so' denote central, central volume part, central surface-peaked part, imaginary, and spin-orbit, respectively. V_{Coul} denotes the Coulomb interaction due to a uniformly charged sphere of radius R_c and charge Ze. It is necessary for proton scattering to take account of the interaction of the incident proton with the charge distribution due to the protons in the nucleus. It has the form

$$V_{Coul} = (Ze^2 /2R_c) \{ 3 - (r/R_c)^2 \} \qquad r \le R_c$$

$$= (Ze^2 /r) \qquad r \ge R_c \qquad \text{AI.2}$$

The spin-orbit potential is necessary for particles with non-zero spin because it is needed to explain the polarization of the elastically scattered particles.

Different theoretical calculations have shown that F_x has the same shape as the nuclear density distribution. Various forms for this function have been introduced, some of them are for the purpose of computational convenience. The most common form is that of the Wood-Saxon function which is given as

$$F_x = [1 + \exp \{ (r-R_x)/a_x \}]^{-1} \qquad \text{AI.3}$$

where $R_x = r_x A^{1/3}$, and in general the radius and the diffuseness parameters r_x and a_x are different for different parts of the potential.

The optical model potential is used extensively to describe elastic scattering data, both in its microscopic and phenomenological forms. In the last few years a relativistic form of the optical potential based on the Dirac equation was introduced, and it proved to be more successful than its nonrelativistic counterpart in describing experimental data at intermediate energies, especially spin observables and the reaction cross section. The relativistic optical model potential is a mixture of a Lorentz scalar potential U_s, and the time like component of a four-vector potential, U_v. The latter two potentials are complex and have the following form

$$U_s = V_s F_s + i W_s F_{is}$$

$$U_v = V_v F_v + i W_v F_{iv} \qquad \text{AI.4}$$

The Dirac equation (with $\hbar$=c=1) is given by

$$[\, \alpha \cdot p + \beta (m + U_s)] \Psi = (E - U_v - V_{Coul}) \Psi \qquad \text{AI.5}$$

where α and β are the 4 by 4 Dirac matrices, m is the rest mass of the projectile, E is the total projectile energy in the center of momentum frame, and Ψ is a 4 by 4 Dirac spinor which could be written in terms of upper Ψ_u and lower Ψ_l components. In order to compare both the relativistic and nonrelativistic approaches, it is convenient to write equation (AI.5) in second order form (Sa84, Sh86), which is given by

$$[\, (p^2/2m) + U_{cent}(r) + U_{s.o.}(r)\, \sigma.L \,]\, \phi_u = (k^2/2m)\, \phi_u \qquad \text{AI.6}$$

where

$$K^2 = E^2 - m^2 \qquad \text{AI.7}$$

$$\phi_u = s^{-1/2} \Psi_u \qquad \text{AI.8}$$

$$s = (E - U_v - V_{coul} + m + U_s) \qquad \text{AI.9}$$

the total central potential is

$$U_{cent}(r) = -[(E - U_v - V_{coul})^2 - (m + U_s)^2 - (E^2 - m^2)] / (2m)$$

$$-[1/r\, s'/s - 3/4 (s'/s)^2 + 1/2\, s''/s] / (2m) \qquad \text{AI.10}$$

and the spin-orbit potential is

$$U_{s.o.}(r) = - s' / (2mrs) \qquad \text{AI.11}$$

where s´ is the radial derivative of s, given by

$$s' = \partial s / \partial r \qquad \text{AI.12}$$

The optical model potential parameters (Li86) based on both the relativistic and non relativistic approaches, which are obtained from fitting the elastic data using the code RUNT (Co81b) for both ^{28}Si and ^{24}Mg at different energies are listed in table (AI.1).

Table AI.1

Non-relativistic and Relativistic Optical Model Parameters for ^{24}Mg(p,p) and ^{28}Si(p,p) using the code RUNT Co81b.

	Non-Relativistic				Relativistic			
	^{28}Si		^{24}Mg		^{28}Si		^{24}Mg	
E_p	200	250	400	250	200	250	400	250
V_0	10.10	8.08	19.00	7.61	274.4	326.1	326.1	337.7
R_0	1.45	1.37	1.03	1.46	1.00	0.95	1.08	0.94
a_0	0.50	0.74	0.43	0.83	0.58	0.63	0.68	0.63
W_0	23.09	26.85	37.31	25.04	-167.3	-116.4	-83.16	-103.9
R_w	1.12	1.09	1.10	1.09	1.09	0.92	1.33	1.10
a_w	0.60	0.66	0.58	0.72	1.56	0.89	0.75	0.63
V_{so}	4.14	3.67	1.21	3.63	-367.7	-448.9	-577.7	-471.5
R_{so}	0.86	0.93	0.94	0.93	0.98	0.93	1.00	0.91
a_{so}	0.66	0.60	0.47	0.59	0.63	0.67	0.73	0.66
V_{soi}	-3.42	-3.66	-3.88	-2.56	195.2	125.4	111.9	111.9
R_{soi}	0.98	0.93	0.96	0.94	1.07	0.84	1.34	1.08
a_{soi}	0.55	0.62	0.59	0.70	0.55	0.99	0.70	0.63

Appendix II

AII.1

Cross Sections, Spin-Flip Probabilities and Spin-Flip Cross Sections in steps of 1 MeV without background subtraction for the $^{24}Mg(p,p')^{24}Mg^{*}$ reaction at 250 MeV at θ_{lab}=2.9°.

Ex (MeV)	Cross Section (mb/sr/MeV)	Snn	Snn .Cross Section (mb/sr/MeV)
0.0	0.222E+01 ± 0.181E -01	0.020 ± 0.023	0.448E -01 ± 0.522E -01
5.0	0.475E -01 ± 0.265E -02	0.019 ± 0.090	0.917E -03 ± 0.429E -02
6.0	0.355E+00 ± 0.723E -02	0.059 ± 0.056	0.209E -01 ± 0.199E -01
8.0	0.101E+00 ± 0.386E -02	0.336 ± 0.090	0.340E -01 ± 0.914E -02
9.0	0.243E+00 ± 0.598E -02	0.052 ± 0.070	0.126E -01 ± 0.170E -01
10.0	0.530E+00 ± 0.883E -02	0.548 ± 0.047	0.290E+00 ± 0.256E -01
11.0	0.179E+01 ± 0.162E -01	0.535 ± 0.027	0.957E+00 ± 0.496E -01
12.0	0.233E+00 ± 0.586E -02	0.245 ± 0.064	0.570E -01 ± 0.151E -01
13.0	0.131E+01 ± 0.139E -01	0.493 ± 0.031	0.644E+00 ± 0.417E -01
14.0	0.803E+00 ± 0.109E -01	0.361 ± 0.039	0.289E+00 ± 0.319E -01
15.0	0.603E+00 ± 0.943E -02	0.436 ± 0.044	0.263E+00 ± 0.267E -01
16.0	0.997E+00 ± 0.121E -01	0.506 ± 0.035	0.504E+00 ± 0.357E -01
17.0	0.124E+01 ± 0.135E -01	0.260 ± 0.032	0.323E+00 ± 0.395E -01
18.0	0.138E+01 ± 0.143E -01	0.365 ± 0.030	0.505E+00 ± 0.414E -01
19.0	0.156E+01 ± 0.152E -01	0.261 ± 0.028	0.407E+00 ± 0.445E -01
20.0	0.136E+01 ± 0.142E -01	0.357 ± 0.030	0.485E+00 ± 0.411E -01
21.0	0.113E+01 ± 0.129E -01	0.333 ± 0.032	0.375E+00 ± 0.366E -01
22.0	0.114E+01 ± 0.130E -01	0.363 ± 0.032	0.414E+00 ± 0.372E -01
23.0	0.111E+01 ± 0.128E -01	0.351 ± 0.033	0.390E+00 ± 0.365E -01
24.0	0.101E+01 ± 0.122E -01	0.303 ± 0.034	0.307E+00 ± 0.345E -01

25.0	0.994E+00 ± 0.121E -01	0.311 ± 0.034	0.309E+00 ± 0.343E -01
26.0	0.958E+00 ± 0.119E -01	0.317 ± 0.036	0.304E+00 ± 0.342E -01
27.0	0.915E+00 ± 0.116E -01	0.355 ± 0.036	0.325E+00 ± 0.329E -01
28.0	0.840E+00 ± 0.111E -01	0.343 ± 0.037	0.288E+00 ± 0.314E -01
29.0	0.778E+00 ± 0.107E -01	0.340 ± 0.039	0.264E+00 ± 0.302E -01
30.0	0.744E+00 ± 0.105E -01	0.363 ± 0.039	0.270E+00 ± 0.292E -01
31.0	0.701E+00 ± 0.102E -01	0.407 ± 0.040	0.286E+00 ± 0.282E -01
32.0	0.679E+00 ± 0.100E -01	0.438 ± 0.040	0.298E+00 ± 0.277E -01
33.0	0.670E+00 ± 0.994E -02	0.419 ± 0.041	0.281E+00 ± 0.277E -01
34.0	0.625E+00 ± 0.960E -02	0.452 ± 0.041	0.282E+00 ± 0.263E -01
35.0	0.599E+00 ± 0.940E -02	0.388 ± 0.043	0.233E+00 ± 0.259E -01
36.0	0.571E+00 ± 0.917E -02	0.421 ± 0.043	0.240E+00 ± 0.249E -01
37.0	0.522E+00 ± 0.877E -02	0.384 ± 0.045	0.201E+00 ± 0.240E -01
38.0	0.423E+00 ± 0.789E -02	0.409 ± 0.047	0.173E+00 ± 0.201E -01
39.0	0.327E+00 ± 0.694E -02	0.377 ± 0.049	0.123E+00 ± 0.162E -01
40.0	0.212E+00 ± 0.558E -02	0.369 ± 0.051	0.781E -01 ± 0.111E -01

AII.2

Cross Sections, Spin-Flip Probabilities and Spin-Flip Cross Sections in steps of 1 MeV without background subtraction for the $^{24}Mg(p,p')^{24}Mg$ reaction at 250 MeV at θ_{lab}=6.55°.

Ex (MeV)	Cross Section (mb/sr/MeV)	Snn	Snn .Cross Section (mb/sr/MeV)
0.0	0.342E+01 ± 0.286E -01	0.079 ± 0.017	0.270E+00 ± 0.566E -01
1.0	0.293E+01 ± 0.265E -01	0.091 ± 0.019	0.266E+00 ± 0.553E -01
2.0	0.776E+00 ± 0.135E -01	0.114 ± 0.034	0.885E -01 ± 0.266E -01
3.0	0.251E -01 ± 0.243E -02	0.165 ± 0.074	0.414E -01 ± 0.191E -02
4.0	0.476E+00 ± 0.106E -01	0.028 ± 0.043	0.135E -01 ± 0.204E -01
5.0	0.363E -01 ± 0.292E -02	0.119 ± 0.097	0.434E -02 ± 0.354E -02
7.0	0.205E+00 ± 0.696E -02	0.039 ± 0.066	0.806E -02 ± 0.134E -01
8.0	0.278E+00 ± 0.811E -02	0.122 ± 0.055	0.339E -01 ± 0.154E -01
9.0	0.222E+00 ± 0.728E -02	0.049 ± 0.061	0.109E -01 ± 0.135E -01
10.0	0.487E+00 ± 0.109E -01	0.401 ± 0.043	0.195E+00 ± 0.215E -01
11.0	0.104E+01 ± 0.158E -01	0.304 ± 0.030	0.317E+00 ± 0.316E -01
12.0	0.320E+00 ± 0.873E -02	0.248 ± 0.052	0.793E -01 ± 0.168E -01
13.0	0.114E+01 ± 0.166E -01	0.350 ± 0.028	0.400E+00 ± 0.322E -01
14.0	0.926E+00 ± 0.149E -01	0.373 ± 0.031	0.345E+00 ± 0.294E -01
15.0	0.924E+00 ± 0.149E -01	0.375 ± 0.031	0.346E+00 ± 0.287E -01
16.0	0.113E+01 ± 0.165E -01	0.421 ± 0.028	0.478E+00 ± 0.325E -01
17.0	0.130E+01 ± 0.177E -01	0.346 ± 0.025	0.450E+00 ± 0.335E -01
18.0	0.163E+01 ± 0.198E -01	0.355 ± 0.023	0.579E+00 ± 0.384E -01
19.0	0.150E+01 ± 0.190E -01	0.350 ± 0.024	0.527E+00 ± 0.362E -01
20.0	0.158E+01 ± 0.195E -01	0.353 ± 0.023	0.557E+00 ± 0.371E -01
21.0	0.134E+01 ± 0.180E -01	0.391 ± 0.024	0.524E+00 ± 0.335E -01
22.0	0.148E+01 ± 0.189E -01	0.379 ± 0.024	0.561E+00 ± 0.358E -01
23.0	0.146E+01 ± 0.187E -01	0.406 ± 0.023	0.591E+00 ± 0.350E -01
24.0	0.136E+01 ± 0.181E -01	0.441 ± 0.024	0.600E+00 ± 0.337E -01
25.0	0.124E+01 ± 0.173E -01	0.444 ± 0.025	0.551E+00 ± 0.320E -01

26.0	0.121E+01 ± 0.170E -01	0.375 ± 0.025	0.452E+00 ± 0.305E -01
27.0	0.113E+01 ± 0.165E -01	0.379 ± 0.026	0.430E+00 ± 0.299E -01
28.0	0.109E+01 ± 0.162E -01	0.371 ± 0.026	0.405E+00 ± 0.293E -01
29.0	0.107E+01 ± 0.160E -01	0.412 ± 0.027	0.441E+00 ± 0.297E -01
30.0	0.102E+01 ± 0.157E -01	0.427 ± 0.028	0.436E+00 ± 0.292E -01
31.0	0.968E+00 ± 0.153E -01	0.484 ± 0.028	0.468E+00 ± 0.280E -01
32.0	0.950E+00 ± 0.151E -01	0.408 ± 0.029	0.387E+00 ± 0.278E -01
33.0	0.909E+00 ± 0.148E -01	0.439 ± 0.029	0.399E+00 ± 0.276E -01
34.0	0.880E+00 ± 0.146E -01	0.452 ± 0.030	0.398E+00 ± 0.274E -01
35.0	0.847E+00 ± 0.143E -01	0.435 ± 0.031	0.368E+00 ± 0.272E -01
36.0	0.825E+00 ± 0.141E -01	0.485 ± 0.033	0.400E+00 ± 0.279E -01
37.0	0.791E+00 ± 0.138E -01	0.395 ± 0.035	0.313E+00 ± 0.284E -01
38.0	0.774E+00 ± 0.137E -01	0.361 ± 0.038	0.279E+00 ± 0.301E -01
39.0	0.737E+00 ± 0.133E -01	0.449 ± 0.041	0.331E+00 ± 0.311E -01
40.0	0.685E+00 ± 0.128E -01	0.410 ± 0.045	0.281E+00 ± 0.312E -01
41.0	0.662E+00 ± 0.126E -01	0.405 ± 0.049	0.268E+00 ± 0.330E -01
42.0	0.645E+00 ± 0.125E -01	0.393 ± 0.054	0.254E+00 ± 0.349E -01
43.0	0.588E+00 ± 0.119E -01	0.408 ± 0.059	0.240E+00 ± 0.351E -01
44.0	0.569E+00 ± 0.117E -01	0.447 ± 0.063	0.254E+00 ± 0.364E -01
45.0	0.515E+00 ± 0.111E -01	0.334 ± 0.075	0.172E+00 ± 0.387E -01

AII.3

Cross Sections, Analysing Powers and the Polarization functions in steps of 1 MeV without background subtraction for the $^{24}Mg(p,p')^{24}Mg$ reaction at 250 MeV at θ_{lab}=2.9°.

Ex (Mev)	Cross Section (mb/sr/MeV)	Analysing Power	Polarisation
0.0	0.222E+01 ± 0.181E -01	-0.133 ± 0.011	-0.002 ± 0.047
1.0	0.289E -01 ± 0.206E -02	0.017 ± 0.096	0.081 ± 0.208
2.0	0.149E+00 ± 0.469E -02	0.079 ± 0.042	0.197 ± 0.134
3.0	0.657E -01 ± 0.311E -02	0.113 ± 0.064	0.247 ± 0.125
4.0	0.148E+00 ± 0.467E -02	0.164 ± 0.042	0.111 ± 0.122
5.0	0.475E -01 ± 0.265E -02	0.163 ± 0.075	-0.097 ± 0.180
6.0	0.355E+00 ± 0.723E -02	0.041 ± 0.027	0.041 ± 0.112
7.0	0.220E+00 ± 0.569E -02	-0.013 ± 0.035	0.166 ± 0.145
8.0	0.101E+00 ± 0.386E -02	-0.004 ± 0.052	0.337 ± 0.179
9.0	0.243E+00 ± 0.598E -02	0.003 ± 0.033	-0.025 ± 0.140
10.0	0.530E+00 ± 0.883E -02	-0.063 ± 0.023	-0.006 ± 0.095
11.0	0.179E+01 ± 0.162E -01	-0.024 ± 0.012	0.072 ± 0.055
12.0	0.233E+00 ± 0.586E -02	0.104 ± 0.034	0.083 ± 0.129
13.0	0.131E+01 ± 0.139E -01	0.013 ± 0.014	0.007 ± 0.063
14.0	0.803E+00 ± 0.109E -01	0.010 ± 0.018	0.101 ± 0.079
15.0	0.603E+00 ± 0.943E -02	-0.046 ± 0.021	0.136 ± 0.087
16.0	0.997E+00 ± 0.121E -01	0.046 ± 0.016	0.038 ± 0.071
17.0	0.124E+01 ± 0.135E -01	-0.012 ± 0.015	0.028 ± 0.063
18.0	0.138E+01 ± 0.143E -01	0.035 ± 0.014	0.028 ± 0.059
19.0	0.156E+01 ± 0.152E -01	0.040 ± 0.013	0.044 ± 0.057
20.0	0.136E+01 ± 0.142E -01	0.036 ± 0.014	0.050 ± 0.060
21.0	0.113E+01 ± 0.129E -01	0.023 ± 0.015	0.053 ± 0.065
22.0	0.114E+01 ± 0.130E -01	0.020 ± 0.015	0.020 ± 0.065
23.0	0.111E+01 ± 0.128E -01	0.069 ± 0.016	0.049 ± 0.065
24.0	0.101E+01 ± 0.122E -01	0.057 ± 0.016	0.038 ± 0.068

25.0	0.994E+00 ± 0.121E -01	0.084 ± 0.016	0.091 ± 0.069
26.0	0.958E+00 ± 0.119E -01	0.064 ± 0.017	0.050 ± 0.071
27.0	0.915E+00 ± 0.116E -01	0.002 ± 0.017	0.135 ± 0.071
28.0	0.840E+00 ± 0.111E -01	0.039 ± 0.018	0.148 ± 0.074
29.0	0.778E+00 ± 0.107E -01	0.037 ± 0.019	0.106 ± 0.077
30.0	0.744E+00 ± 0.105E -01	0.020 ± 0.019	0.107 ± 0.078
31.0	0.701E+00 ± 0.102E -01	0.058 ± 0.020	0.045 ± 0.080
32.0	0.679E+00 ± 0.100E -01	0.055 ± 0.020	0.105 ± 0.080
33.0	0.670E+00 ± 0.994E -02	0.020 ± 0.020	0.062 ± 0.082
34.0	0.625E+00 ± 0.960E -02	0.008 ± 0.021	0.056 ± 0.083
35.0	0.599E+00 ± 0.940E -02	0.027 ± 0.021	-0.014 ± 0.086
36.0	0.571E+00 ± 0.917E -02	0.049 ± 0.022	0.034 ± 0.086
37.0	0.522E+00 ± 0.877E -02	0.010 ± 0.023	0.086 ± 0.091
38.0	0.423E+00 ± 0.789E -02	-0.001 ± 0.025	0.074 ± 0.094
39.0	0.327E+00 ± 0.694E -02	0.000 ± 0.029	0.144 ± 0.098
40.0	0.212E+00 ± 0.558E -02	0.003 ± 0.036	0.015 ± 0.103

AII.4

Cross Sections, Analysing Powers and the Polarization functions in steps of 1 MeV without background subtraction for the $^{24}Mg(p,p')^{24}Mg$ reaction at 250 MeV at θ_{lab}=6.55°.

Ex (Mev)	Cross Section (mb/sr/MeV)	Analysing Power	Polarisation
0.0	0.342E+01 ± 0.286E -01	0.155 ± 0.014	0.428 ± 0.028
1.0	0.293E+01 ± 0.265E -01	0.133 ± 0.014	0.358 ± 0.032
2.0	0.776E+00 ± 0.135E -01	0.477 ± 0.035	0.515 ± 0.068
3.0	0.251E -01 ± 0.243E -02	0.487 ± 0.126	0.546 ± 0.143
4.0	0.476E+00 ± 0.106E -01	0.411 ± 0.037	0.358 ± 0.083
5.0	0.363E -01 ± 0.292E -02	0.558 ± 0.105	0.426 ± 0.212
6.0	0.118E+00 ± 0.536E -02	-0.080 ± 0.060	-0.093 ± 0.126
7.0	0.205E+00 ± 0.696E -02	0.447 ± 0.050	0.580 ± 0.122
8.0	0.278E+00 ± 0.811E -02	0.383 ± 0.044	0.466 ± 0.097
9.0	0.222E+00 ± 0.728E -02	0.223 ± 0.045	0.269 ± 0.102
10.0	0.487E+00 ± 0.109E -01	-0.027 ± 0.030	0.190 ± 0.067
11.0	0.104E+01 ± 0.158E -01	0.039 ± 0.020	0.225 ± 0.047
12.0	0.320E+00 ± 0.873E -02	0.246 ± 0.039	0.392 ± 0.085
13.0	0.114E+01 ± 0.166E -01	0.131 ± 0.021	0.212 ± 0.044
14.0	0.926E+00 ± 0.149E -01	0.061 ± 0.022	0.121 ± 0.048
15.0	0.924E+00 ± 0.149E -01	0.103 ± 0.022	0.293 ± 0.047
16.0	0.113E+01 ± 0.165E -01	0.051 ± 0.020	0.102 ± 0.043
17.0	0.130E+01 ± 0.177E -01	0.089 ± 0.019	0.272 ± 0.039
18.0	0.163E+01 ± 0.198E -01	0.113 ± 0.017	0.187 ± 0.036
19.0	0.150E+01 ± 0.190E -01	0.063 ± 0.017	0.147 ± 0.037
20.0	0.158E+01 ± 0.195E -01	0.116 ± 0.018	0.177 ± 0.036
21.0	0.134E+01 ± 0.180E -01	0.076 ± 0.018	0.119 ± 0.038
22.0	0.148E+01 ± 0.189E -01	0.069 ± 0.017	0.144 ± 0.037
23.0	0.146E+01 ± 0.187E -01	0.096 ± 0.018	0.176 ± 0.036
24.0	0.136E+01 ± 0.181E -01	0.090 ± 0.019	0.166 ± 0.037

25.0	0.124E+01 ± 0.173E -01	0.066 ± 0.019	0.137 ± 0.039
26.0	0.121E+01 ± 0.170E -01	0.060 ± 0.019	0.181 ± 0.038
27.0	0.113E+01 ± 0.165E -01	0.073 ± 0.020	0.189 ± 0.040
28.0	0.109E+01 ± 0.162E -01	0.069 ± 0.020	0.140 ± 0.041
29.0	0.107E+01 ± 0.160E -01	0.060 ± 0.020	0.146 ± 0.042
30.0	0.102E+01 ± 0.157E -01	0.041 ± 0.021	0.168 ± 0.043
31.0	0.968E+00 ± 0.153E -01	0.074 ± 0.021	0.113 ± 0.043
32.0	0.950E+00 ± 0.151E -01	0.053 ± 0.022	0.181 ± 0.044
33.0	0.909E+00 ± 0.148E -01	0.103 ± 0.022	0.163 ± 0.045
34.0	0.880E+00 ± 0.146E -01	0.043 ± 0.022	0.131 ± 0.047
35.0	0.847E+00 ± 0.143E -01	0.044 ± 0.023	0.099 ± 0.049
36.0	0.825E+00 ± 0.141E -01	0.053 ± 0.023	0.152 ± 0.051
37.0	0.791E+00 ± 0.138E -01	0.055 ± 0.023	0.187 ± 0.055
38.0	0.774E+00 ± 0.137E -01	0.056 ± 0.023	0.030 ± 0.060
39.0	0.737E+00 ± 0.133E -01	0.050 ± 0.024	0.160 ± 0.064
40.0	0.685E+00 ± 0.128E -01	0.080 ± 0.025	0.075 ± 0.070
41.0	0.662E+00 ± 0.126E -01	0.018 ± 0.025	0.130 ± 0.076
42.0	0.645E+00 ± 0.125E -01	0.032 ± 0.026	0.034 ± 0.083
43.0	0.588E+00 ± 0.119E -01	0.055 ± 0.027	0.153 ± 0.092
44.0	0.569E+00 ± 0.117E -01	0.066 ± 0.028	-0.096 ± 0.098
45.0	0.515E+00 ± 0.111E -01	0.033 ± 0.029	0.165 ± 0.116

Appendix III

AIII.1

$(1^+, T=1, Ex=10.71\ MeV)$
$^{24}Mg(p,p')^{24}Mg\ \ E_p = 250\ MeV$

θ_{cm}	$d\sigma/d\Omega$ (mb/sr)	A_Y
2.68	1.83034±0.120	-0.0489±0.0445
2.97	1.76179±0.114	-0.0241±0.0417
3.23	1.72823±0.113	-0.0494±0.0450
6.44	0.77870±0.064	0.0130±0.0350
6.80	0.72725±0.055	-0.0325±0.0341
7.12	0.66421±0.054	0.0523±0.0365

AIII.2

$(1^+, T=0, Ex=11.45\ MeV)$
$^{28}Si(p,p')^{28}Si\ \ E_p = 250\ MeV$

θ_{cm}	$d\sigma/d\Omega$ (mb/sr)	A_Y
3.78	0.55279±0.053	-0.0566±0.041
4.43	0.59752±0.052	-0.1874±0.033
5.10	0.60051±0.035	-0.0738±0.042
6.54	0.52114±0.035	-0.1473±0.016
7.29	0.52282±0.034	-0.1823±0.013
8.15	0.50083±0.033	-0.1294±0.014

AIII.3

(1^+,T=1, Ex=11.45 MeV)
$^{28}Si(p,p')^{28}Si$ E_p = 250 MeV

θ_{cm}	dσ/dΩ (mb/sr)	Ay
3.78	2.28874±0.160	-0.0326±0.083
4.43	2.14476±0.148	-0.0083±0.073
5.10	1.68243±0.123	0.0014 ±0.071
6.54	0.96036±0.062	-0.0179±0.023
7.29	0.75121±0.048	-0.0325±0.017
8.15	0.59419±0.039	-0.0465±0.016

AIII.4

(1^+,T=0, Ex=11.45 MeV)
$^{28}Si(p,p')^{28}Si$ E_p = 290 MeV

θ_{cm}	dσ/dΩ (mb/sr)	Ay
3.67	0.43059±0.115	-0.0568±0.030
4.23	0.44639±0.111	-0.0571±0.031
4.81	0.41530±0.097	-0.2021±0.029

AIII.5

(1^+,T=1, Ex=11.45 MeV)
$^{28}Si(p,p')^{28}Si$ E_p = 290 MeV

θ_{cm}	dσ/dΩ (mb/sr)	Ay
3.67	1.64724±0.100	-0.0491±0.058
4.23	1.55587±0.083	0.0290 ±0.061
4.81	1.33349±0.071	-0.0417±0.055

AIII.6

(1^+,T=0, Ex=11.45 MeV)
$^{28}Si(p,p')^{28}Si$ E_p = 360 MeV

θ_{cm}	dσ/dΩ (mb/sr)	A_Y
3.85	0.45249±0.035	-0.0823±0.022
4.61	0.46436±0.036	-0.0922±0.023
5.32	0.50968±0.040	-0.0374±0.026

AIII.7

(1^+,T=1, Ex=11.45 MeV)
$^{28}Si(p,p')^{28}Si$ E_p = 360 MeV

θ_{cm}	dσ/dΩ (mb/sr)	A_Y
3.85	1.51194±0.100	0.0244 ±0.043
4.61	1.21458±0.083	-0.0647±0.040
5.32	0.99552±0.071	-0.0130±0.055

AIII.8

(1^+,T=0, Ex=11.45 MeV)
$^{28}Si(p,p')^{28}Si$ E_p = 400 MeV

θ_{cm}	dσ/dΩ (mb/sr)	A_Y
4.16	0.45636±0.037	-0.3476±0.0242
4.92	0.47719±0.038	-0.2494±0.0254
5.76	0.44791±0.035	-0.0862±0.0231
6.33	0.44200±0.033	-0.1233±0.0193
7.18	0.46142±0.033	-0.0319±0.0181
8.04	0.43376±0.033	0.0890 ±0.0192